Ultrasonic Techniques for Baseline-Free Damage Detection in Structures

Submitted in partial fulfillment of the
requirements for the degree of
Doctor of Philosophy

in

Civil and Environmental Engineering

Debaditya Dutta

B.Tech. (Hons.), Civil Engineering, Indian Institute of Technology Kharagpur (2006)
M.S., Civil and Environmental Engineering, Carnegie Mellon University (2007)

Carnegie Mellon University
Pittsburgh, PA

September, 2010

Thesis committee

Dr. Hoon Sohn (Advisor)

Adjunct Professor, Civil and Environmental Engineering Department, Carnegie Mellon University

and

Associate Professor, Civil and Environmental Engineering Department, Korea Advanced Institute of Science and Technology

Dr. Irving J. Oppenheim (Co-Advisor)

Professor, Civil and Environmental Engineering Department, Carnegie Mellon University

Dr. Jacobo Bielak

University Professor, Civil and Environmental Engineering Department, Carnegie Mellon University

Dr. James H. Garrett, Jr.

Thomas Lord Professor and Head, Civil and Environmental Engineering Department, Carnegie Mellon University

Dr. Piervincenzo Rizzo

Assistant Professor, Civil and Environmental Engineering Department, University of Pittsburgh

Acknowledgements

The success of this research project is due to the support of many people. I wish to express my sincerest gratitude to my advisors, Professor Hoon Sohn and Professor Irving J. Oppenheim, who were abundantly helpful and offered invaluable advice, resources and encouragement. Deepest gratitude is also due to the members of the advisory committee, Professor Jacobo Bielak, Professor James H. Garrett, Jr. and Professor Piervincenzo Rizzo, without whose knowledge and guidance this study would not have been successful.

I take this opportunity to acknowledge the immense help and support that I received from my colleagues: Ms. Yujie Ying, Dr. Seung-Bum Kim, Dr. Sangjun Lee, Mr. Abhinav Agrawal, Mr. Akhilesh Gupta and Dr. Chang-Kook Oh at Carnegie Mellon University, and Mr. Min-Koo Kim, Mr. Hyeonseok Lee, Mr. Chulmin Yeum, Mr. Changgil Lee, Mr. Eui-Jae Jin, Mr. Hyung-Jin Lim, and Ms. Sun-Hye Jung at Korea Advances Institute of Science and Technology.

Special thanks to my friends, especially Mr. Sharad Oberoi, Mr. Mudasar Zahoor, Mr. Sourav Chatterjee, Mr. Suvrajit Maji, Professor Sourav Bhattacharya and Mrs. Sudarshana Mukherjee for their support and encouragement in my research and life in Pittsburgh.

My sincere gratitude once again to Professor Jacobo Bielak at Carnegie Mellon University and my undergraduate advisor Professor L. S. Ramachandra at Indian Institute of Technology Kharagpur for inspiring my interest in the theory of mechanics through lessons and conversations.

Finally I would like to acknowledge the tremendous support that I received from my parents and family members, without which the research project would certainly have been incomplete.

I would also like to convey thanks to the funding agencies for providing the financial means and laboratory facilities. Parts of this work were supported by the Dean's Fellowship at Carnegie Mellon University, Bombardier Inc., Pennsylvania Infrastructure Technology Alliance (PITA) program, Smart Infra-Structure Technology Center (SISTeC), National Science Foundation (NSF award number 0700411), National Research Foundation of Korea (NRF) grant funded by the Korea government (MEST) (No. 2010-0017456) and National Nuclear R&D Program through the National Research Foundation of Korea (NRF) funded by the Ministry of Education, Science and Technology (No. 2009-0083489).

Abstract

This research presents ultrasonic techniques for baseline-free damage detection in structures in the context of structural health monitoring (SHM). Conventional SHM methods compare signals obtained from the pristine condition of a structure (baseline signals) with those from the current state, and relate certain changes in the signal characteristics to damage. While this approach has been successful in the laboratory, there are certain drawbacks of depending on baseline signals in real field applications. Data from the pristine condition are not available for most existing structures. Even if they are available, operational and environmental variations tend to mask the effect of damage on the signal characteristics. Most important, baseline measurements may become meaningless while assessing the condition of a structure after an extreme event such as an earthquake or a hurricane. Such events may destroy the sensors themselves and require installation of new sensors at different locations on the structure. Baseline-free structural damage detection can broaden the scope of SHM in the scenarios described above.

A detailed discussion on the philosophy of baseline-free damage detection is provided in Chapter 1. Following this discussion, the research questions are formulated. The organization of this document and the major contributions of this research are also listed in this chapter.

Chapter 2 describes a fully automated baseline-free technique for notch and crack detection in plates using a collocated pair of piezoelectric wafer transducers for measuring ultrasonic signals. Signal component corresponding to the damage induced

mode-converted Lamb waves is extracted by processing the originally measured ultrasonic signals. The damage index is computed as a function of this mode-converted Lamb wave signal component. An over-determined system of Lamb wave measurements is used to find a least-square estimate of the measurement errors. This error estimate serves as the damage threshold and prevents the occurrences of false alarms resulting from imperfections and noise in the measurement system. The threshold computation from only the measured signals is they key behind baseline-free damage detection in plates.

Chapters 3 and 4 are concerned with nonlinear ultrasonic techniques for crack detection in metallic structures. Chapter 3 describes a nonlinear guided wave technique based on the principle of super-harmonic production due to crack induced nonlinearity. A semi-analytical method is formulated to investigate the behavior of a bilinear crack model. Upon comparing the behavior with experimental observations, it is inferred that a bilinear model can only partially capture the signal characteristics arising from a fatigue crack. A correlation between the extents of nonlinear behavior of a breathing crack with the different stages of the fatigue crack growth is also made in Chapter 3. In Chapter 4, a nonlinear system identification method through coherence measurement is proposed. A popular electro-magnetic impedance circuit was used to detect acoustic nonlinearity produced by a crack.

Chapters 5 and 6 comprise the final part of this thesis where wavefield images from a scanning laser vibrometer are digitally processed to detect defects in composite structures. Once processed, the defect in the scanned surface stands out as an outlier in the background of the undamaged area. An outlier analysis algorithm is then implemented to detect and localize the damage automatically. In Chapter 5, exploratory groundwork on wavefield imaging is done by obtaining wave propagation images from specimens made of different materials and with different geometries. In Chapter 6, a hitherto unnoted phenomenon of standing wave formation in delaminated composite plates is observed and explained. Novel signal and image processing techniques are also proposed in this chapter, of which the isolation of standing waves using wavenumber-frequency domain manipulation and the use of Laplacian image filtering technique deserve special mention.

Contents

List of figures

List of tables

List of related publications

Refereed Journals:

[1] “Application of Principal Component Analysis and Wavelet Transform to Fatigue Crack Detection in Waveguides” M. Cammarata, P. Rizzo, D. Dutta & H. Sohn. *Smart Structures and Systems*, Vol. 6 (4) (2010)

[2] “A Nonlinear Acoustic Technique for Crack Detection in Metallic Structures” D. Dutta, H. Sohn, K. A. Harries & P. Rizzo. *Structural Health Monitoring*, Vol. 8, 251-262 (2009)

[3] “An Unsupervised Learning Algorithm for Fatigue Crack Detection in Waveguides” P. Rizzo, M. Cammarata, D. Dutta, H. Sohn & K. A. Harries. *Smart Materials and Structures*, Vol. 18 (2), 025016, 11 pp (2009)

[4] “A Baseline-Free Crack Detection Using Nonlinear Acoustics.” D. Dutta & H. Sohn *International Journal of Steel Structures,* Vol. 7 (1), 27-31 (2007).

[5] “Temperature Independent Damage Detection in Plates using Redundant Signal Measurements” H. Sohn, D. Dutta & Y. K. An. *Journal of Nondestructive Evaluation* (In review, submitted May 2010)

[6] “Ultrasonic energy trapping by delamination through the production of standing waves” D. Dutta & H. Sohn. *Applied Physics Letters* (In review, submitted July 2010)

[7] “Noncontact guided wave imaging for delamination and disbond detection in composites” H. Sohn, D. Dutta, J. Y. Yang, H. J. Park, M. P. DeSimio, S. E. Olson & E. Swenson. *Composites Science and Technology* (In review, submitted August 2010)

Conference Proceedings:

[1] “A Non-Contact Structural Health Monitoring System through Laser Based Excitation and Sensing of Ultrasonic Guided Waves” D. Dutta, H. Sohn & J. Y. Yang. *Proceedings of the 16th US National Congress of Theoretical and Applied Mechanics*, University Park, PA (July 2010)

[2] “Imaging Ultrasonic Waves in Complex Structures using a Scanning Laser Doppler Vibrometer” H. Sohn, J. Y. Yang, D. Dutta, E. D. Swenson, M. P. DeSimio & S. E. Olson. *Proceedings of the 5th International Conference on Bridge Monitoring, Safety and Management,* Philadelphia, PA (July 2010)

[3] “Delamination Detection in Composite Structures using Laser Vibrometer Measurement of Lamb Waves” H. Sohn, D. Dutta, E. D. Swenson, M. P. DeSimio & S. E. Olson. *Proceedings of the SPIE 17th International Symposium on Smart Structures/NDE,* San Diego, CA (March 2010)

[4] "Baseline-Free Damage Detection through Mode Separation of Lamb Waves using Self-Sensing Piezoelectric Transducers" H. Sohn, D. Dutta & Y. K. An. *Proceedings of the 7th International Workshop on Structural Health Monitoring*, Stanford, CA (September 2009)

[5] "A Nonlinear Acoustic Technique for Crack Detection in Metallic Structures" D. Dutta, H. Sohn, K. A. Harries & P. Rizzo. *Proceedings of the 15th SPIE International Symposium on Smart Structures/NDE*, San Diego, CA (March 2008)

[6] "Crack Detection in Metallic Structures Using Nonlinear Electro-Magnetic 'Impedance' Measurement" D. Dutta & H. Sohn. *Proceedings of the 4th European Workshop on Structural Health Monitoring,* Cracow, Poland (July 2008)

[7] "A Nonlinear Impedance Method and Its Potential Application in Baseline Free Crack Detection in Metallic Structures" D. Dutta & H. Sohn. *Proceedings of the 4th International Conference on Bridge Monitoring, Safety and Management,* Seoul, Korea (July 2008)

[8] "Advanced Signal Processing for Ultrasonic Structural Monitoring of Waveguides" M. Cammarata, P. Rizzo, D. Dutta, H. Sohn & K. A. Harries. *Proceedings of the 4th International Conference on Bridge Monitoring, Safety and Management,* Seoul, Korea (July 2008)

[9] "Advanced Ultrasonic Structural Monitoring of Waveguides" M. Cammarata, D. Dutta, H. Sohn, P. Rizzo & K. A. Harries, *Advances in Science and Technology,* Vol. 56, 477-482. *Proceedings of the CIMTEC 3rd International Conference on Smart Materials, Structures and Systems,* Acireale, Sicily, Italy (June 2008)

[10] "Crack Detection in Metallic Structures Using Nonlinear Electro-Magnetic Impedance Measurement" D. Dutta & H. Sohn. *Proceedings of the 2nd CenSCIR Annual Symposium,* Pittsburgh, PA (May 2008)

[11] "Transition from Guided Wave Based Non-Destructive Testing to Structural Health Monitoring" H. Sohn, S. B. Kim, S. J. Lee, D. Dutta, H. J. Park, C. G. Lee, A. Agrawal, C. M. Yeom, S. H. Park, Y. K. An. *Proceedings of the 35th Annual Review of Progress in Quantitative Nondestructive Evaluation,* Chicago, IL (2008)

1. Introduction

1.1 The evolution of structural health monitoring from nondestructive testing

The American Society of Civil Engineers (ASCE) has slapped a ‘D’ grade to America’s aging infrastructure in its 2009 Report Card [1]. Critical infrastructure like bridges and dams scored ‘C’ and ‘D’ respectively. To ensure proper functionality of such structures and prevent catastrophic failures, regular inspection and maintenance are necessary. Traditional nondestructive evaluation (NDE) methods are often time consuming and labor intensive and therefore infrequent. Moreover, NDE allows only schedule based maintenance while condition based maintenance would be more effective for preventing structural failures as well as more economical [2]. These limitations of NDE have inspired researchers to develop a continuous and automated monitoring system for infrastructure and led to the development of the research field which goes by the name *Structural Health Monitoring* (SHM).

In his book titled *Encyclopedia of Structural Health Monitoring Vol. 1* [3], Christian Boller defines SHM as an “… integration of sensing and possibly also actuation devices to allow the loading and damaging conditions of a structure to be recorded, analyzed, localized, and predicted in a way that nondestructive testing (NDT) becomes an integral part of the structure and material.” SHM infers the current condition of a structure based on a streamline of data collected from sensors installed in the structure. Both centralized processing and distributed processing of the data are possible [4]. A wide variety of data processing techniques are used to detect different types of structural damages under different operational and environmental conditions [5],[6].

Conventional SHM methods compare signals obtained from the pristine condition of a structure (baseline signals) with those from the current state. Certain differences in one or more signal characteristics between the two sets of signals are attributed to damage. Popular SHM techniques such as guided wave based methods [7],[8], electro-mechanical impedance methods [9],[10], nonlinear ultrasonic techniques [11],[12] and vibro-acoustic methods [13] – all rely heavily on baseline measurements.

Of the several different approaches to SHM, ultrasonic guided wave based techniques have emerged as a very prominent option due to their well-established theories, their ability to detect small damages within reasonably large inspection areas, and advancement in transducer technologies used for guided wave sensing and excitation, to name a few [7]. Guided waves are specific types of elastic waves confined by the boundaries of a structure. For example, when a plate structure is excited at a high frequency, the top and bottom surfaces of the plate "guide" the elastic waves along its axis, producing a specific type of guided waves called Lamb waves [14-16]. Various types of transducers can be used for the excitation and sensing of guided waves. The most commonly used ones are angled piezoelectric wedge transducers, piezoelectric wafer transducers, electromagnetic acoustic transducers, and comb transducers [7]. Some transducers are mainly used for sensing applications such as polyvinylidene fluoride (PVDF) and fiber optic sensors. The transducers mentioned above are all used for sensing at discrete points on the structure. More recently, people have started using scanning laser vibrometers for creating wavefield images across the surface of the structure with high spatial resolution [17],[18]. Besides allowing high resolution, laser vibrometry is essentially a non-contact measurement technique. Thus, it avoids adding additional mass and disturbance to the target structure. Also, a single laser vibrometer can be used to acquire data from a reasonably large inspection area.

In this thesis, we will focus mainly on guided wave based techniques. Both piezoelectric wafer transducers and laser vibrometers are used in the experiments.

1.2 What is baseline free condition assessment and why is it necessary?

Traditional NDE methods such as C-scan are baseline-free in the sense that they do not require a direct comparison of the current data with a baseline data to detect damage [19]. This is possible due to small and specific inspection areas and extensive involvement of human experts. Such is not the case for SHM where the infrastructure of a whole country is to be continuously monitored. The need for large scale distributed sensing and automation makes the use of baseline measurements almost imperative [20]. As a result, the popular SHM techniques all rely heavily on baseline data, as mentioned in the previous section. There are, however, certain drawbacks of using baseline measurements in real field applications. Data from the pristine condition are not available for most existing structures. Measurements obtained from C or D-grade structures would therefore pass as baseline data which might seriously undermine the process of successful damage detection. Moreover, baseline measurements may become meaningless while assessing the condition of a structure after an extreme event such as earthquake which might destroy the sensors themselves. Baseline-free damage detection would broaden the scope of SHM in such cases as well as those where operational and environmental variations tend to mask the effect of damage on the signal characteristics [21].

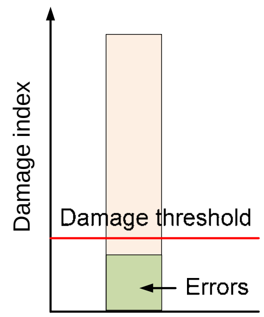

Figure 1.1 Specimens having damage index value below the damage threshold are classified as undamaged structures and vice versa

Figure 1.2 Both damage and errors contribute to the damage index value. The damage threshold is an estimate of the error level.

To develop a fully baseline-free technique, both the damage index and the damage threshold must be computed from the signals obtained only from the current state of the structure (henceforth called "current signals" or "current data" for the sake of abbreviation). Here, the damage index is a quantitative measure of damage (e.g. the amplitude of the reflected ultrasonic signal from damage). In real applications, the damage index would be non-zero even for undamaged structures, due to bias and random errors in the measurement system. Therefore a threshold for the damage index is necessary to avoid false positive alarms. This threshold between a false positive and a real positive identification of damage is called the damage threshold (**Figure 1.1** and **Figure 1.2**). In a baseline-free damage detection technique, the challenge is not only to compute the damage index but also to compute the damage threshold from the current data. Under certain circumstances, an estimate of the measurement error level may be computed from the current data [21]. This estimate may serve as the damage threshold.

1.3 Research questions

Based on the discussion in the preceding sections, the research questions associated with the baseline free damage detection of a structure may be framed as following:

- What is the signature of a specific type of damage in the ultrasonic signal?
- Based on this signature, how to obtain a quantitative damage index (DI) from the ultrasonic signal through signal processing?
- How to set a threshold on the DI to avoid false alarms?

Note that in the absence of a baseline, the threshold must be estimated from the signals measured from the current state of the structure only.

1.4 Organization of this document

The answers to the above research questions will be attempted in the subsequent chapters with regards to different types of structures and damages. A fully automated baseline-free technique for notch and crack detection in plates is developed in Chapter 2. Nonlinear ultrasonic techniques for crack detection in metallic structures are explored in Chapters 3 and 4. Chapter 3 describes a nonlinear guided wave based technique while Chapter 4 deals with a nonlinear system identification method. Chapters 5 and 6 comprise the final part of this thesis where wavefield images from a scanning laser vibrometer are digitally processed to detect hidden delamination and disbond in composite structures. Exploratory work to outline the scope of laser vibrometry is done in Chapter 5. Chapter 6, on the other hand, deals with the specific problem of automatically detecting delamination and disbond from the scanned images.

1.5 Unique contributions of this research

The major findings of this research effort are listed below

- Developing a fully automated Lamb wave based baseline-free technique for damage detection in plate like structures (Chapter 2)
- Correlating the extent of nonlinear behavior of a breathing crack with the different stages of the fatigue crack growth (Chapter 3)
- Formulating a semi-analytical method to investigate the behavior of a bilinear crack model and comparing it with experimental observations (Chapter 3)
- Developing a nonlinear system identification technique using an electro-magnetic impedance circuit (Chapter 4)
- Examining and interpreting the wavefield images obtained from a wide variety of structures of engineering interest (Chapter 5)
- Observing and explaining the occurrence of standing waves in a delaminated composite (Chapter 6)
- Developing novel signal and image processing techniques to detect the formation of standing waves (Chapter 6)
- Developing outlier analyses techniques to detect delamination and disbond from scanned wavefield images in a baseline-free manner (Chapter 6)

2. Baseline-free damage detection in plates using Lamb waves

2.1 Motivation

Plates and plate-like structures are ubiquitous in civil, mechanical and aerospace industries. Moreover, wave propagation in plates is relatively simple to study and hence it is a good starting point for testing the feasibility of automated baseline-free ultrasonic damage detection techniques.

2.2 Chapter abstract

This chapter describes a method to detect notch like damages in plates using piezoelectric transducers. The method does not use prior baseline data for damage detection. A single pair of piezoelectric wafer transducers made of Lead Zirconate Titanate (PZT) is attached back to back on the opposite sides of a plate and are used for simultaneous actuation and sensing. A notch, which is a sudden change in thickness of the plate, leads to mode conversion of Lamb waves. The mode converted wave component in the measured signal is then separated from the other Lamb wave mode components using polarization characteristics of the piezoelectric wafer transducers. The damage index is a function of the amplitude of this mode converted component of the signal. In real world situations, the damage index will not be exactly zero due to inaccuracy in transducer collocation and non-uniformity in their bonding conditions. Therefore, a (non-zero) threshold for the damage index needs to be established to avoid false alarms. True to the spirit of baseline-free damage detection, this threshold is computed from the signals acquired only from the current state of the structure. This is achieved by using redundancy in signal measurements. Since the method detects damages without having to rely on baseline data, environmental variations like temperature change do not affect its performance. Results from numerical simulations as well as experiments on aluminum specimens are provided to demonstrate the effectiveness of the method described above.

2.3 Chapter introduction

The technique described in this chapter is baseline-free in the sense that (1) the damage-sensitive feature is extracted without a direct comparison of the current data with baseline data and (2) the threshold for damage classification is also obtained only from the current measurements. Some prior knowledge of the structure is still required though. In this study, this prior knowledge is that the structure is a plate. The ubiquity of plates and plate like structures in the civil, mechanical and aerospace industries justifies the effort. To detect damage in plates, the present study uses a technique that is based on the principle of mode conversion of Lamb waves at a surface-breaking notch or crack [22]. Several researchers have used this principle for detecting damages in plates or plate-like structures [21],[23-27]. The guided waves in the plate (Lamb waves) are generated and sensed by piezoelectric wafer transducers (henceforth called PZTs for the sake of abbreviation). The polarization property of the PZTs is used to generate different combinations of the Lamb wave modes [21],[28]. Later, the sensed signals are digitally processed to extract the various modal components present in those signals. A novelty of the present chapter is to extract these modal components using only two piezoelectric wafers. Previously it was possible with four such wafers [21],[29]. Among the extracted modal components is the component corresponding to mode converted Lamb waves. The converted Lamb wave mode is present only when there is an asymmetric damage in the plate such as a surface breaking notch or a crack. However, due to the many sources of non-idealities in the measurement system, the extracted modal component corresponding to mode conversion may not exactly be zero. These non-idealities may be noise in the measurement channel, or collocation and bonding mismatch in the PZTs which influence the precise generation and measurement of the selective Lamb wave modes. In this chapter we propose a scheme to estimate the extent of these non-idealities through redundant signal measurements which is the second and key novelty of this chapter. By measuring more signals than are necessary to extract the independent Lamb wave modes, we create an over-determined system which is then solved through a least-square inversion process. The deviation error (also known as least-square error) incurred in the process of least-square inversion is an estimate of the non-idealities in the measurement system and serves as the basis for establishing a threshold to classify damaged and undamaged structures. Thus, we not only compute the damage index (amplitude of the mode-conversion component of the sensed signals) from the current measurements but also a reasonable estimate of the damage threshold. Computing the damage threshold from the current measurements is a critical step for automated baseline-free classification of plates into damaged and undamaged categories. It is worthy of note here that some earlier studies had successfully computed the damage index from current measurements only [30],[31],[11]. However, in each case, the choice of the damage threshold was somewhat arbitrary. More recently, it was also possible to get a good estimate of the damage threshold using time of flight information [23],[29]. But using time of flight information can be tricky when there are multiple reflections from the boundary and when the crack is not directly in the line of sight of the two pairs of PZTs used in those studies. The present method is free from the above limitations and hence completely automatable, as demonstrated through the experiments in Section 2.6.

This chapter is organized as follows. First, the theoretical development of the technique is provided in Section 2.4, followed by simulation (Section 2.5) and experimental validation (Section 2.6) of the theory. The chapter then concludes with a brief critique.

2.4 Theoretical development

This section is presented in two stages. The first subsection deals with the extraction of the different Lamb wave modal components in the measured signals. The second one describes a methodology to compute the damage index based on the extracted mode conversion component and also illustrates a method to compute the damage threshold.

2.4.1 Extraction of the modal components

The polarization characteristics of piezoelectric materials and its use in Lamb wave mode extraction are described in [21]. The same line of reasoning is followed here. A schematic of the target structure is shown in **Figure 2.1**. Two collocated PZTs, PZTs P and Q, are used to excite as well as sense the guided waves in pulse-echo configuration. The guided waves are excited by either one of PZTs P and Q or both PZTs simultaneously. The generated waves are then reflected from the boundaries of the structure as well as the defects (if any) and subsequently sensed by the same PZTs. It is assumed in the theoretical development that the PZTs are identical in shape and size and have identical bonding conditions with the structure. Although the method is applicable to any range of excitation frequency, for simplicity of discussion the driving frequencies of the ultrasonic signals are limited to a range so as to allow the excitation of only the fundamental symmetric (S_0) and anti-symmetric (A_0) Lamb wave modes [32],[16],[33]. The symmetric Lamb mode corresponds to equal stretching conditions (tension or compression) on both sides of the plate. The anti-symmetric mode corresponds to stretching conditions which are equal in magnitude but opposite in sign on the two sides of the plate. Therefore, if a particular input voltage on PZT P produces a particular set of S_0 and A_0 modes, the same input to PZT Q will generate an identical S_0 mode but an equal and opposite A_0 mode in the structure. Selective generation of either S_0 or A_0 mode can be done by simultaneous excitation of the two PZTs with appropriate input voltages, thereby reinforcing the desired mode and canceling out the other [21],[28]. The experimental configuration for selective mode generation will be mentioned in a later section. Similar argument used for Lamb wave generation can be used for Lamb wave sensing as well. Both PZTs P and Q would measure the same voltage for an S_0 mode but would measure equal but opposite voltages for an A_0 mode (**Figure 2.2**).

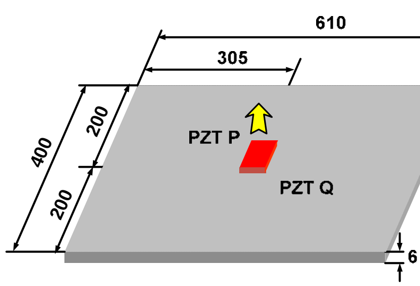

Figure 2.1 Test configuration showing poling directions of the collocated PZT wafers. PZT P is attached on the top and PZT Q is on the bottom surface. All dimensions are in mm.

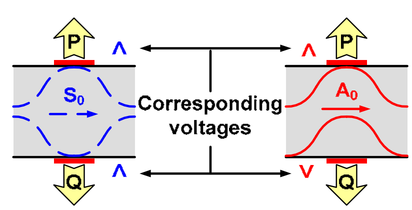

Figure 2.2 S_0 and A_0 modes measured using the PZT configuration shown in **Figure 2.1**. The voltages corresponding to S_0 mode are in-phase while those corresponding to A_0 mode are out of phase.

Mode conversion of Lamb waves (e.g. from the S_0 mode to the A_0 mode or vice versa) takes place when waves propagating along a thin plate of uniform thickness encounter a discontinuity such as a sudden thickness variation due to damage [22],[21]. The S_0 and the A_0 modes originally produced by the PZTs encounter the defect and the boundaries multiple times as they propagate back and forth. Thereby they undergo multiple scatterings and mode conversions before being picked up by the PZTs as measured signals. Any measured signal $Y(t)$ will therefore be a linear superposition of four constituent signal components: $X_{SS}(t)$, $X_{SA}(t)$, $X_{AS}(t)$, and $X_{AA}(t)$; where t denotes time; and $X_{AS}(t)$ is the component of the signal $Y(t)$ which corresponds to an anti-symmetric (A_0) mode when generated but a symmetric (S_0) mode when measured, the mode conversion(s) having taken place at the defect location. $X_{SS}(t)$, $X_{SA}(t)$ and $X_{AA}(t)$ are defined likewise. Theoretically there would be no mode conversion for an undamaged plate with free boundaries [21],[34]. So the measured signals from undamaged plates would contain only two constituent components viz. $X_{SS}(t)$ and $X_{AA}(t)$. Actually, a shear horizontal (SH) mode may be generated by non-normally incident S_0 mode on a free boundary. However, the transduction devices used in this study most likely have no sensitivity to SH modes. The numerical and experimental results confirm that such modes, even if they exist, do not affect the technique.

Based on the discussion earlier in this section, the relative signs of the constituent signal components ($X_{AS}(t)$ etc.) present in the measured signal $Y(t)$ will be different depending on which PZT actuates and which one senses. The signal actuated by PZT P and sensed by PZT Q is called $Y_{PQ}(t)$ etc. For the sake of convenience, the parentheses *(t)* are dropped from all the signal notations in the remainder of the chapter. **Figure 2.3** shows an example case, in which the relative phases of the Lamb wave modes present in the measured signals Y_{PP} and Y_{QQ} are shown. Similar figures can be constructed for other pairs of the measured signals. Equation (2.1) is the compact mathematical representation of what is shown in **Figure 2.3**, the concept being extended to other pairs of the measured signals as well.

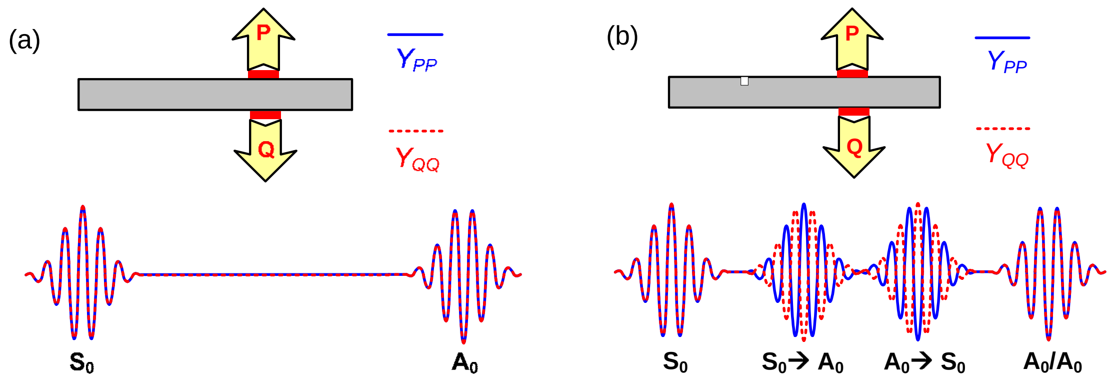

Figure 2.3 Signals Y_{PP} and Y_{QQ} (a) without and (b) with a notch (theoretical prediction).

$$\begin{pmatrix} Y_{PP} \\ Y_{PQ} \\ Y_{QP} \\ Y_{QQ} \end{pmatrix} = \begin{bmatrix} 1 & 1 & 1 & 1 \\ 1 & 1 & -1 & -1 \\ 1 & -1 & 1 & -1 \\ 1 & -1 & -1 & 1 \end{bmatrix} \begin{pmatrix} X_{SS} \\ X_{AS} \\ X_{SA} \\ X_{AA} \end{pmatrix} \tag{2.1}$$

In Equation (2.1), the coefficients in the matrix on the right hand side denote the relative contribution of the constituent signal components in each measured signal. Now, let us examine the signals Y_{PQ} and Y_{QP}. According to the theorem of dynamic reciprocity [35]:

$$Y_{PQ} = Y_{QP} \tag{2.2}$$

Writing Y_{PQ} and Y_{QP} in terms of the constituent signal components according to Equation (2.1) and then equating those according to Equation (2.2), the following relationship between the two types of signal components is obtained:

$$X_{SA} = X_{AS} = 0.5X_{MC} \tag{2.3}$$

where "*MC*" stands for "mode conversion." The significance of Equation (2.3) is that the two signal components related to mode conversion (S_0 to A_0 and A_0 to S_0) reinforce each other and manifest as a single signal component X_{MC}. Note that the above statement holds true specifically for the PZT configuration discussed in this chapter (**Figure 2.1**). Using Equation (2.1)(2.3), Equation (2.1) may be rewritten as:

$$\begin{pmatrix} Y_{PP} \\ Y_{PQ} \\ Y_{QP} \\ Y_{QQ} \end{pmatrix} = \begin{bmatrix} 1 & 1 & 1 \\ 1 & 0 & -1 \\ 1 & 0 & -1 \\ 1 & -1 & 1 \end{bmatrix} \begin{pmatrix} X_{SS} \\ X_{MC} \\ X_{AA} \end{pmatrix} \tag{2.4}$$

If selective modes are also actuated by simultaneously exciting the PZTs P and Q using a switch circuit [28], Equation (2.1) may be expanded as:

$$\mathbf{Y = DX}, \text{ where } \mathbf{Y} = \begin{pmatrix} Y_{PP} \\ Y_{PQ} \\ Y_{QP} \\ Y_{QQ} \\ Y_{SP} \\ Y_{SQ} \\ Y_{AP} \\ Y_{AQ} \end{pmatrix}, \ \mathbf{D} = \begin{bmatrix} 1 & 1 & 1 \\ 1 & 0 & -1 \\ 1 & 0 & -1 \\ 1 & -1 & 1 \\ 1 & 0.5 & 0 \\ 1 & -0.5 & 0 \\ 0 & 0.5 & 1 \\ 0 & 0.5 & -1 \end{bmatrix} \text{ and } \mathbf{X} = \begin{pmatrix} X_{SS} \\ X_{MC} \\ X_{AA} \end{pmatrix} \tag{2.5}$$

Here Y_{SP} is the signal actuated by exciting both PZTs P and Q simultaneously to selectively generate the symmetric mode (S_0) only and then eventually sensed by PZT P. Y_{SQ}, Y_{AP} and Y_{AQ} are similarly defined. In theory, $Y_{SP} = 0.5(Y_{PP} + Y_{QP})$, etc. [28] Note that Equation (2.5) is an over-determined system where the number of (known) measured signals is more than the number of unknown signal components to be extracted. The reason behind this redundant signal measurement will be clear from the discussion below.

From Equation (2.5), a least-square estimate of the signal components $\widetilde{\mathbf{X}}$ can be obtained from the measured signals, **Y,** using Moore-Penrose (pseudo) inverse of **D** [36]:

$$\widetilde{\mathbf{X}} = \mathbf{D}^{+}\mathbf{Y} \text{ where } \widetilde{\mathbf{X}} = \begin{pmatrix} \widetilde{X}_{SS} \\ \widetilde{X}_{MC} \\ \widetilde{X}_{AA} \end{pmatrix} \tag{2.6}$$

where $^{+}$ denotes the pseudo inverse of a matrix. Under ideal circumstances, $\widetilde{X}_{MC}$ would be zero for undamaged structures but non-zero for damaged ones. However, in practical situations, even undamaged structures are expected to exhibit non-zero $\widetilde{X}_{MC}$ due to noise and other reasons mentioned earlier. A non-zero threshold is therefore required to determine whether $\widetilde{X}_{MC}$ is produced just by noise etc. or whether it is produced by mode conversion at damage location as well.

2.4.2 Damage detection

As mentioned earlier, Moore-Penrose inverse gives the least-square estimate of an over-determined system. The deviation error (also known as least-square error) incurred in the process of the least-square inversion is an estimate of the non-idealities in the measurement system. This deviation error is computed through the reconstruction of the measured signals from the least-square estimates of the signal components. If one tries to reconstruct the measured signals from the estimated signal components using:

$$\widetilde{\mathbf{Y}} = \mathbf{D}\widetilde{\mathbf{X}} = \mathbf{D}\mathbf{D}^{+}\mathbf{Y} \tag{2.7}$$

the reconstructed signal $\widetilde{\mathbf{Y}}$ would not, in most practical cases, correspond exactly to the originally measured signals **Y**. It is only reasonable that the same non-idealities that cause non-zero $\widetilde{X}_{MC}$ in an undamaged structure would also be reflected as errors in the reconstructed signals (***e***):

$$\mathbf{e} = \mathbf{Y} - \widetilde{\mathbf{Y}} = (\mathbf{I} - \mathbf{D}\mathbf{D}^{+})\mathbf{Y} \tag{2.8}$$

where **I** is a 8x8 identity matrix. Based on the above discussion, if the damage index is defined to be a measure of the mode conversion viz. $\widetilde{X}_{MC}$, then a meaningful damage threshold would be a measure of the reconstruction errors (**e**). Note that the terms ‘reconstruction error’, ‘deviation error’ and ‘least-square error’ are used interchangeably. This non-zero damage threshold (**e**) will contain the effects of noise and non-idealities of the structure as well as the instrumentation.

In this study, tone-burst signals at n different frequencies are used to generate Lamb waves in the structure. AMC_i is the amplitude of the Fast Fourier Transform (*FFT*) of $\widetilde{X}_{MC}$ at the i^{th} frequency (i = 1,2,…,n) when a tone-burst signal centered at the i^{th} frequency is used for excitation:

$$AMC_i = \left| FFT(\widetilde{X}_{MC}) \right|_i \tag{2.9}$$

H_i is similarly defined and gives the maximum of the errors committed in reconstructing the eight measured signals from the least-square estimates:

$$H_i = max(\left|FFT(e_j)\right|_i), \quad j = 1,2,...,8 \tag{2.10}$$

where e_j is the j^{th} reconstruction error so that e_1 is the error in reconstructing signal Y_{PP} (i.e. $e_1 = Y_{PP} - \tilde{Y}_{PP}$), etc. AMC_i and H_i are thus the quantitative measures of damage and damage threshold respectively, both computed from the current measurements. To avoid the risk of false results due an inappropriate choice of frequency, AMC_i and H_i are averaged over a range of frequencies. The criterion for classifying a given structure into undamaged or damaged category is established based on these averaged values:

$$\begin{aligned} &\overline{AMC} = \frac{1}{n}\sum_{i=1}^{n} AMC_i \\ &\overline{H} = \frac{1}{n}\sum_{i=1}^{n} H_i \\ &\text{If } \overline{AMC} > \overline{H} \text{ then damage exists.} \\ &\text{Otherwise no damage.} \end{aligned} \tag{2.11}$$

In summary, this section established the theory behind the baseline-free damage detection technique in plates with free boundaries. This theory is validated through numerical simulation and experiments in the subsequent sections.

2.5 Simulation results

Using the PZFlex finite element software, Lamb wave propagation in an aluminum beam was simulated. A two-dimensional plane strain model was used for simulation. **Figure 2.4** shows the damaged structure, the undamaged one being without the notch. A 5 cycle tone-burst voltage signal centered at 150 kHz was used as input. The accuracy of the matrix **D** is corroborated by the fact that the reconstruction errors, **e** in Equation (2.7), are almost negligible (e.g. **Figure 2.5**). **Figure 2.6** compares the least-square estimates constituent signal components obtained from the undamaged plate with those obtained from the damaged one.

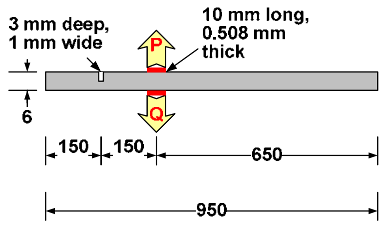

Figure 2.4 Dimensions (in mm) of an aluminum plate used for numerical simulation.

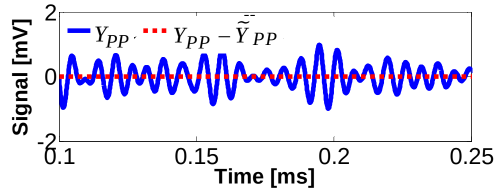

Figure 2.5 Reconstruction error in Y_{PP} in the damaged specimen (numerical simulation).

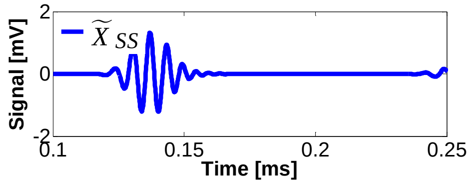

(a) Signal component corresponding to S_0 mode in intact plate

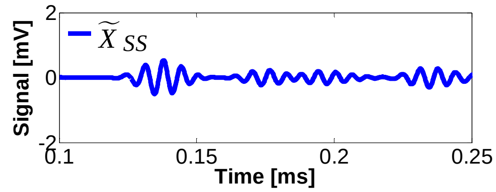

(b) Signal component corresponding to S_0 mode in damaged plate

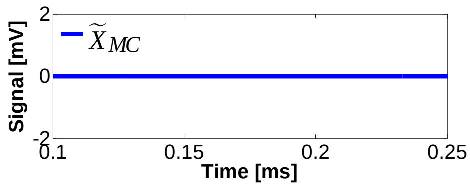

(c) Signal component corresponding to mode conversion in intact plate

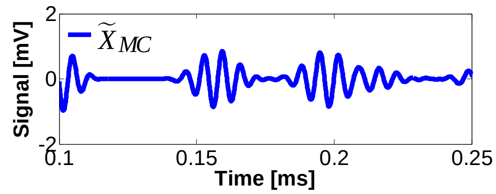

(d) Signal component corresponding to mode conversion in damaged plate

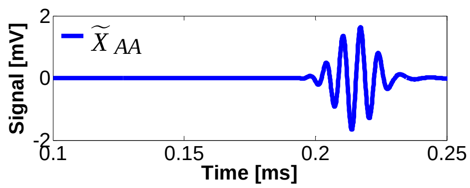

(e) Signal component corresponding to A_0 mode in intact plate

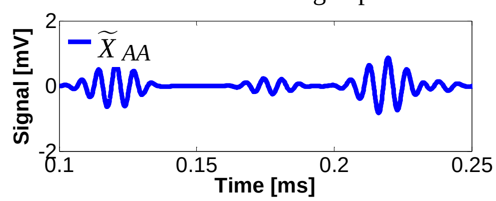

(f) Signal component corresponding to A_0 mode in damaged plate

Figure 2.6 Comparison of the least-square estimates of the constituent signal components between the intact case and the damaged case (results obtained from numerical simulation).

It can be observed that the damaged structure exhibits significant mode conversion, as opposed to the absence of the same in the undamaged structure. Additional reflections of the S_0 and A_0 modes due to the notch can also be observed. Because of the ideal conditions implicit in the numerical simulation, $\widetilde{X}_{MC}$ is practically absent in the signals obtained from the undamaged plate. Therefore the application of the damage classifier is redundant for the numerical simulation results.

2.6 Experimental results

The proposed damage detection technique was further examined through tests conducted on an aluminum plate (**Figure 2.1** and **Figure 2.7**). Two PZTs insulated with a coating of Kapton were mounted back to back on the opposite faces of the plate. The scheme for data acquisition is shown in **Figure 2.8**.

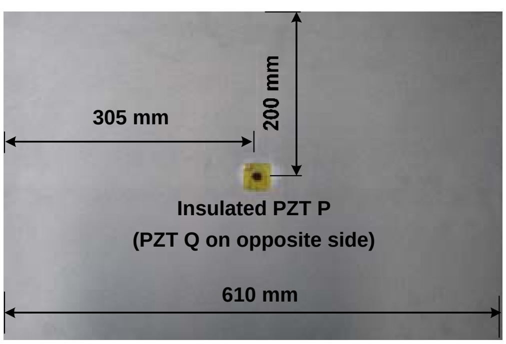

Figure 2.7 The 6 mm aluminum plate specimen.

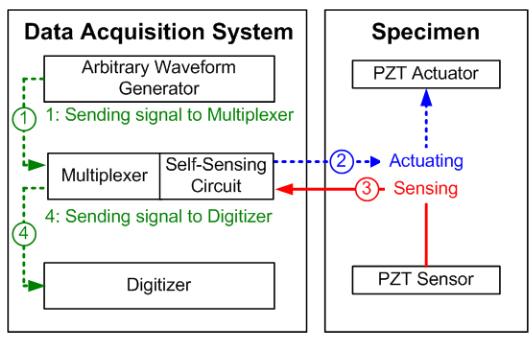

Figure 2.8 Scheme for data acquisition

The circuit scheme for acquiring signals Y_{PP}, Y_{PQ}, Y_{SP} and Y_{SQ} are shown in **Figure 2.9**. Here a voltage divider circuit is used to allow measurement of the piezoelectric voltage across the PZTs even when the input voltage channel is on. Such a circuit is called a self-sensing piezoelectric circuit as it allows simultaneous actuation and sensing using only a single PZT [37],[38]. Similar circuit configurations were used to measure the other four signals (Y_{QP}, Y_{QQ}, Y_{AP} and Y_{AQ}). The electric terminals were reversed with respect to the electrodes of PZT Q in order to excite the selective A_0 mode in the structure. It is worthy to mention here that voltage divider circuits have been used for different purposes in the context of SHM including piezoelectric self-diagnosis [39].

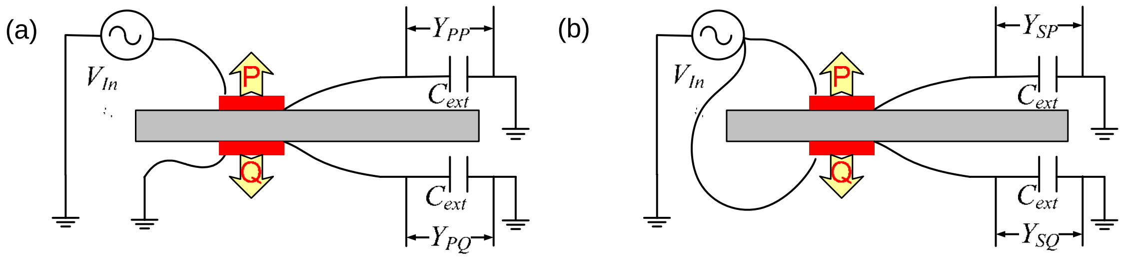

Figure 2.9 Circuit configurations for acquiring the signals (a) Y_{PP} and Y_{PQ}, and (b) Y_{SP} and Y_{SQ}.

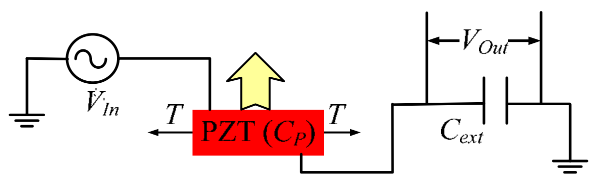

Figure 2.10. A self-sensing piezoelectric circuit using an external capacitor as a voltage divider.

In a self-sensing circuit (**Figure 2.10**), the output voltage (V_{out}) is related to the tensile stress in the PZT (T) through Equation (2.10):

$$V_{out} = \frac{C_P}{C_P + C_{ext}}\left(V_{in} - \frac{ds}{C_P}T\right) \tag{2.12}$$

where C_P is the capacitance of the PZT, C_{ext} is the capacitance of the external capacitor, V_{in} the input voltage, d is the piezoelectric constant of PZT and s is the surface area of the PZT wafer. Equation (2.9) can be derived from the fundamental constitutive equation of piezoelectric materials [2] using basic circuit analysis.

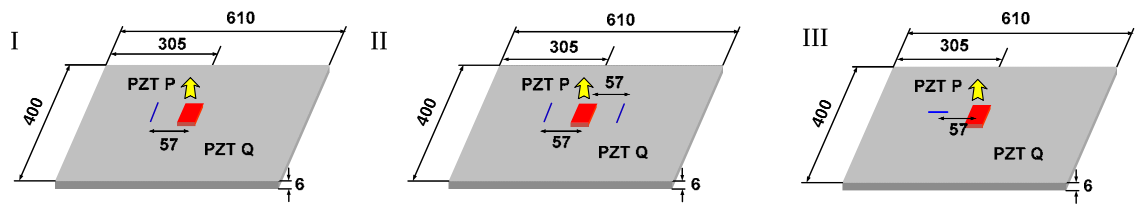

Figure 2.11 The three damage scenarios. All dimensions are in mm. Each notch is 3 mm deep, 30mm long and 1 mm wide.

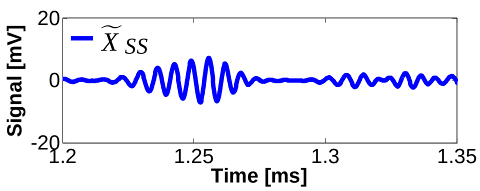

(a) Signal component corresponding to S_0 mode in intact plate

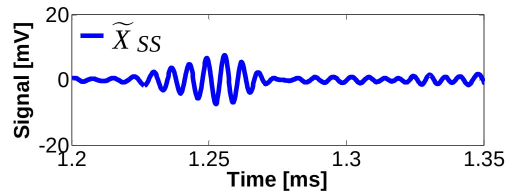

(b) Signal component corresponding to S_0 mode in damaged plate

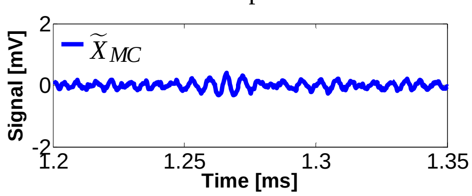

(c) Signal component corresponding to mode conversion in intact plate

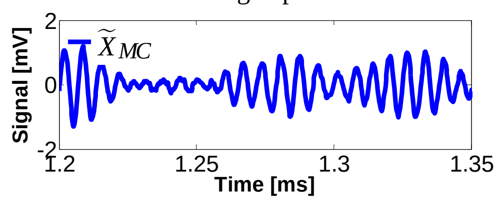

(d) Signal component corresponding to mode conversion in damaged plate

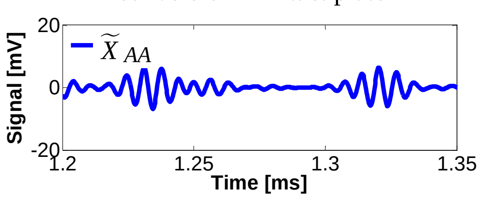

(e) Signal component corresponding to A_0 mode in intact plate

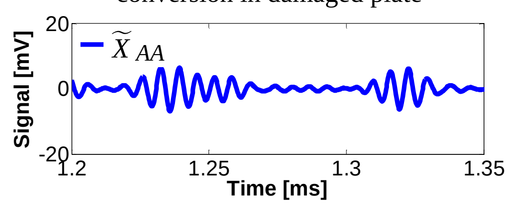

(f) Signal component corresponding to A_0 mode in damaged plate

Figure 2.12 Comparison of the least-square estimates of the constituent signal components between the intact case and the damaged case III (results obtained from experiment).

The experiment was performed on three damage cases (**Figure 2.11**) as well as the undamaged case (**Figure 2.1**). A comparison of the decomposed modes obtained from the undamaged case and the damage case-III is shown in **Figure 2.12**.

A 5 cycle tone-burst voltage signal centered at 150 kHz was used as input. It may be observed that the undamaged specimen exhibits slightly nonzero $\widetilde{X}_{MC}$ due to PZT imperfection and measurement noise. The presence of mode conversion in the damaged specimen is very prominent though and can be attributed to the existence of a notch. The experimental procedure was repeated with the center frequency of the tone-burst input signal varying from 100 kHz to 200 kHz with a step of 1 kHz.

Figure 2.13 shows the spectra of the mode converted and the error signals at tested frequency range for the undamaged case and damaged case III. The baseline-free damage classifier discussed in the "Theoretical development" section was then applied on the experimentally obtained signals. The algorithm resulted in correct classification of the specimen's condition as far as the existence of damage is concerned (**Figure 2.14**).

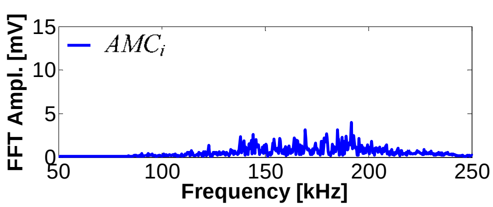

(a) Amplitude of mode conversion in undamaged plate at different frequencies of excitation

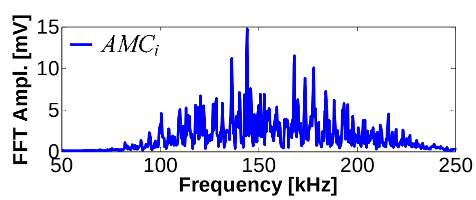

(b) Amplitude of mode conversion in damaged plate at different frequencies of excitation

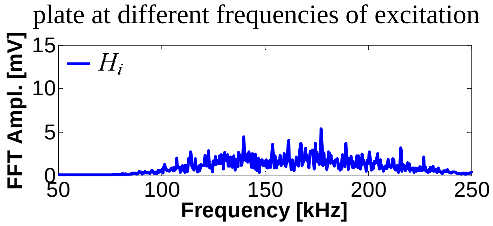

(c) Threshold amplitude computed for intact plate at different frequencies of excitation

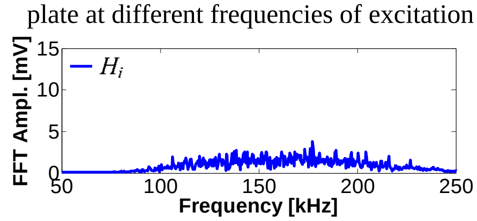

(d) Threshold amplitude computed for damaged plate at different frequencies of excitation

Figure 2.13 Comparison of the amplitude of mode conversion and threshold amplitude between the intact case and the damage case III at different frequencies.

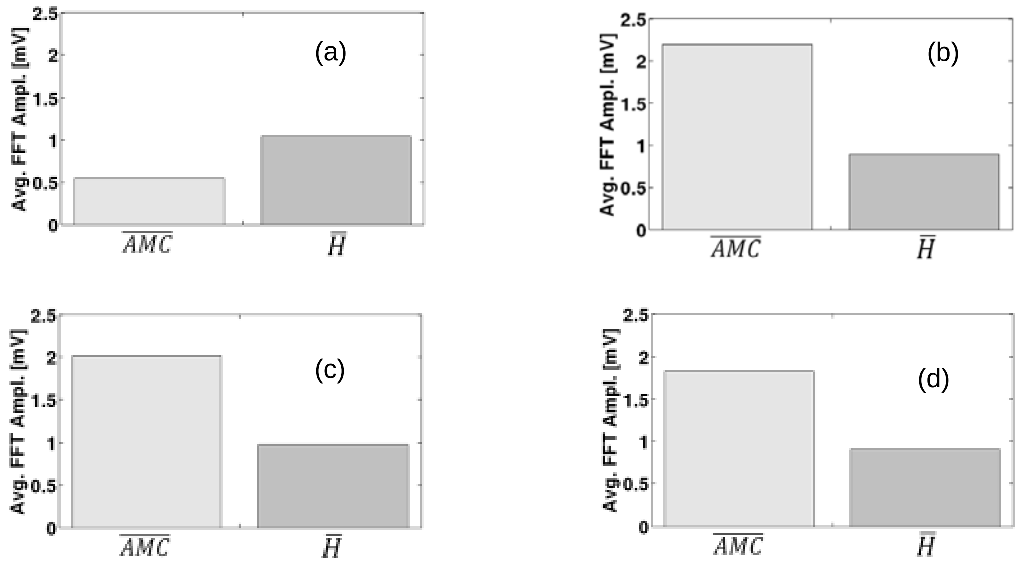

Figure 2.14 Damage classification: (a) Undamaged (b) Damage-I (c) Damage-II (d) Damage-III. (A structure is classified as damaged only when $\overline{AMC}$ becomes larger than $\overline{H}$)

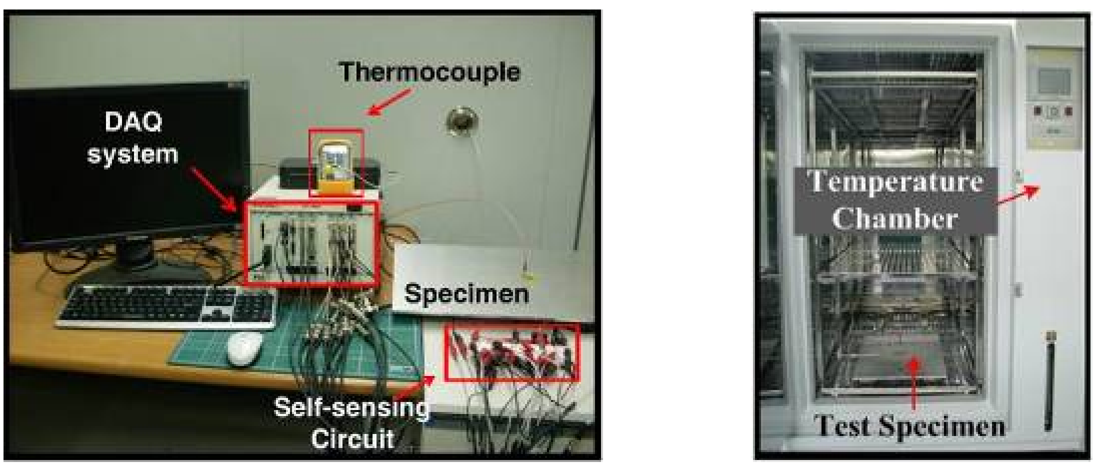

(a) Overall experimental setup (b) Test specimen in temperature chamber

Figure 2.15 Experimental setup for temperature variation tests.

Variability in environmental and operational conditions (e.g. temperature variation) often adversely affects the performances of SHM techniques, especially the ones which depend on baseline data [40]. In particular, the role of temperature variation has often been studied [41-44]. Therefore, the robustness of the proposed damage detection technique to the variation of ambient temperature is investigated in the following paragraphs. The same set of the undamaged and damaged specimens was used. **Figure 2.15** shows the experimental set-up for the temperature variation tests.

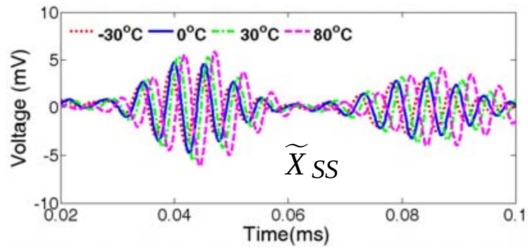

(a) Signal component corresponding to S_0 mode in intact plate

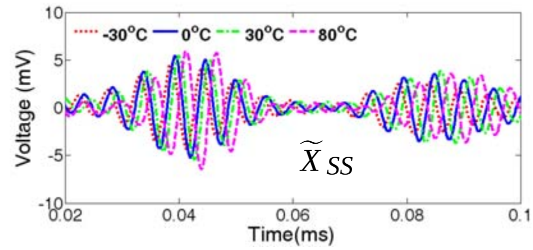

(b) Signal component corresponding to S_0 mode in damaged plate

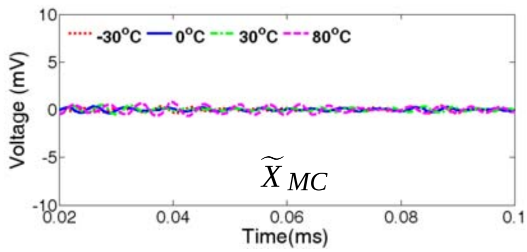

(c) Signal component corresponding to mode conversion in intact plate

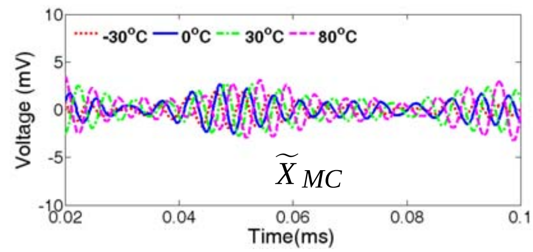

(d) Signal component corresponding to mode conversion in damaged plate

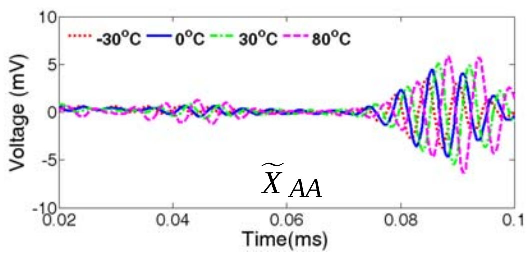

(e) Signal component corresponding to A_0 mode in intact plate

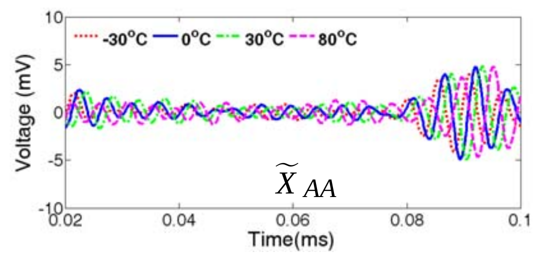

(f) Signal component corresponding to A_0 mode in damaged plate

Figure 2.16 Comparison of the least square estimates of the constituent signal components between the intact case and the damage case I (experiments performed at different temperatures).

Figure 2.16 shows the decomposed modes from the undamaged specimen and the damaged specimen I at different temperatures. Although the signals themselves vary with temperature, the extent of mode conversion in the damaged specimen is always greater than that in the undamaged specimen. Since the technique described in this chapter relies only on the relative magnitude of mode conversion with respect to the initial error level, the technique remains robust to temperature variation.

Table 2.1 Damage classification of the test aluminum article at varying temperatures. The number in bold font in the columns $\overline{AMC}$ and $\overline{H}$ represents which one among $\overline{AMC}$ or $\overline{H}$ is bigger.

CASE	Temp. (^{0}C)	Damage Index ($\times 10^{-4}$)		Damage Classifier
		$\overline{AMC}$	$\overline{H}$	
INTACT	-30	2.7	**4.5**	Intact
	0	2.8	**6.1**	Intact
	30	3.1	**7.7**	Intact
	80	3.2	**9.7**	Intact
DAMAGE I	-30	**7**	4	Damage
	0	**8**	5.1	Damage
	30	**8.8**	6.2	Damage
	80	**9.3**	7.3	Damage
DAMAGE II	-30	**7.9**	3.7	Damage
	0	**9.5**	4.8	Damage
	30	**11**	5.3	Damage
	80	**12**	5.7	Damage
DAMAGE III	-30	**7.4**	4	Damage
	0	**8.7**	5.4	Damage
	30	**9.3**	6.5	Damage
	80	**10**	7.9	Damage

Once again, the baseline-free damage detection algorithm described in the "Theoretical development" section was applied and the algorithm resulted in accurate classification of the specimen's damage state (**Table 2.1**).

2.7 Chapter summary

The chapter describes a baseline-free damage detection technique in plate structures which is also robust to variation in the ambient temperature. The principle of work is based on the mode conversion of Lamb waves due to defects. The mode conversion is detected using the polarization property of piezoelectric wafer transducers. To avoid false alarms, a structure is adjudged damaged only if the amplitude of the mode converted signal goes beyond a certain threshold. The threshold is computed from the signals acquired only from the current state of the structure by exploiting the redundancy in signal measurements. This threshold level represents the error levels in the signals due to PZT imperfection and measurement noises. The technique was validated through simulations as well as experiments. The application of the method is at the moment limited to plate structures with uniform thickness only.

3. Crack detection in metallic structures using nonlinear ultrasonics: I. Superharmonics generation

3.1 Motivation

The baseline-free technique described in the previous chapter is limited in application to plates. In this chapter and the next, we will investigate the effectiveness of nonlinear ultrasonic techniques which are used to detect nonlinearity in the ultrasonic medium caused by the breathing mechanism of a crack [45]. Nonlinear techniques are sensitive to cracks but are insensitive to other harmless factors like complex structural features (such as stiffeners and joints) and operational and environmental variability (such as temperature change). This property makes nonlinear techniques good candidates for a baseline-free approach.

3.2 Chapter abstract

A crack detection technique based on nonlinear acoustics is investigated in this study. Acoustic waves at a chosen frequency are generated using an actuating lead zirconate titanate (PZT) transducer, and they travel through the target structure before being received by a sensing PZT wafer. Unlike an undamaged medium, a cracked medium exhibits high acoustic nonlinearity which is manifested as harmonics in the power spectrum of the received signal. Experimental results also indicate that the harmonic components increase non-linearly in magnitude with increasing amplitude of the input signal. The proposed technique identifies the presence of cracks by looking at the two aforementioned features: harmonics and their nonlinear relationship to the input

amplitude. The effectiveness of the technique has been tested on aluminum and steel specimens. The behavior of these nonlinear features as crack propagates in the steel beam has also been studied.

3.3 Chapter introduction

Metallic structures made of aluminum and steel are ubiquitous in mechanical, aerospace and civil infrastructure. Structural failure in metals is often attributed to cracks developed due to fatigue or fracture. For instance, such cracks can develop at the flange-web junction of a bridge girder, in the wings of an aircraft, in railway tracks or in the sub-structures of a power generation plant. In most cases, cracks cannot be avoided. Thus there is a need for non-destructive inspection of such structural components.

Some of the popular NDT techniques for crack detection are acoustic emission [46], eddy current techniques [47], vibration-based techniques [48], impedance-based methods [9],[10] and ultrasonic testing [7]. Ultrasonic guided wave based methods can be broadly classified in two groups: (1) those based on the principles of linear acoustics like transmission, reflection, scattering, mode-conversion and absorption of acoustic energy caused by a defect [49],[50],[21],[51]; and (2) those based on the principles of nonlinear acoustics like harmonics generation [52-54],[12],[55], frequency mixing [56],[11] and modulation of ultrasound by low-frequency vibration [13],[45]. Linear NDT techniques identify cracks by detecting the amplitude and phase change of the response signal caused by defects when a consistent probe signal is applied. On the other hand, nonlinear techniques correlate defects with the presence of additional frequency components in the output signal. Existing literature on damage detection techniques using nonlinear acoustics [56],[11],[12] suggest that nonlinear techniques are robust to harmless factors like complicated geometry or moderate environmental variations *viz.* wind and temperature. This robustness makes the nonlinear acoustic techniques attractive for field applications.

Many existing techniques suffer from one or more drawbacks *viz.* use of bulky equipment, unsuitability of automation and requirement of interpretation of data or image by trained engineers. These shortcomings make existing methods less attractive for online continuous monitoring. The uniqueness of the present study lies in the authors' effort to overcome the aforementioned drawbacks by developing a crack detection technique using PZT wafers (which can be easily surface-mounted or embedded in the structure) and suggesting a damage detection process that can be readily automated. These features might make the proposed technique more suitable for online continuous monitoring of structures. Another unique aspect of this chapter is to study the behavior of the nonlinear features with a propagating crack in a steel beam.

The chapter is organized as follows. First, the theoretical development for acoustic nonlinearity due to cracks is provided. Then, experimental studies performed to verify the effectiveness of the proposed technique are discussed. Finally, this chapter concludes with a brief summary.

3.4 Theoretical development

Fatigue in metallic materials is a progressive, localized, and permanent structural damage that occurs when a material is subjected to cyclic or fluctuating stresses that are less than (often much less than) the static yield strength of the material [22]. The process initiates a discontinuity and becomes a microscopic crack. The crack propagates as a result of subsequent stress applications caused by cyclic loading. The fatigue life depends on the applied stress range and also on the structural geometry. A higher stress range usually leads to shorter fatigue life.

It is well known that a crack in a metallic structure causes nonlinear interaction of acoustic waves [52-54],[12],[55]. A manifestation of this nonlinear interaction is the production of acoustic super-harmonics when the structure is excited with an ultrasonic probing signal of a given frequency [52-54],[12],[55],[11],. Several theories have been proposed to explain the phenomenon of harmonics generation. However, a consensus regarding the physical understanding of the mechanism has not yet been reached. A summary of the existing theoretical models has been given by Parsons and Staszewski [45]. One of the popular theories is the 'breathing crack model' where the crack closes during compression and opens during tension when ultrasonic waves propagate through it [54],[57],[58],[56],[11],[59],[60]. In the following paragraphs, the authors have endeavored to explain the phenomenon of harmonics generation in a semi-analytic manner. The intention is to provide an easy and intuitive understanding of the above phenomenon without indulging into a rigorous mathematical analysis. A variational formulation, similar to that of the finite element method, has been adopted for the purpose of the semi-analytic derivation. The crack is modeled as a single infinitesimal element in the structure that exhibits bilinear stiffness [54],[58],[57].

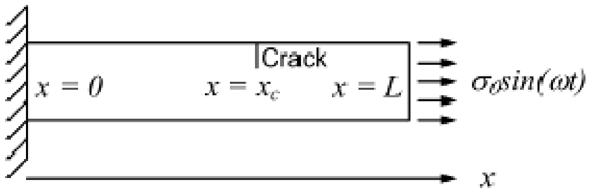

Figure 3.1 A schematic of a cracked beam with a harmonic excitation

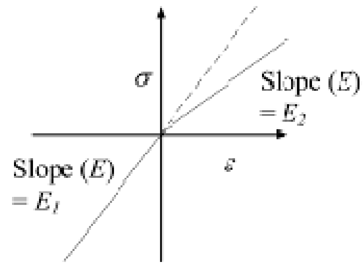

Figure 3.2 Bilinear stress-strain relation at the crack location (x = xc)

Consider a longitudinal wave traveling through a slender elastic beam containing a crack (**Figure 3.1**). The beam is fixed at one end and excited with a harmonic stress at the other. The bilinear stress-strain relationship at the location of the crack is shown in **Figure 3.2**. As a convention, the strain (ε) is considered positive in tension and negative in compression. Mathematically, therefore, the crack is open when $\varepsilon|_{x_c} > 0$ and closed when $\varepsilon|_{x_c} < 0$.

If the mass density of the beam in question is assumed to be uniform and equal to ρ, the governing equation of wave propagation through this structure is given by:

$$\rho \frac{\partial^2 u}{\partial t^2} = \frac{\partial}{\partial x}(E \frac{\partial u}{\partial x})$$
$$E = \begin{cases} E_2 & \text{for } x = x_c \quad \text{and} \quad \varepsilon|_{x = x_c} = \left.\frac{\partial u}{\partial x}\right|_{x = x_c} > 0 \\ E_1 & \text{otherwise} \end{cases} \tag{3.1a}$$

where $u = u(x,t)$ is the longitudinal displacement of a point on the beam at position x and time t, and $E = E(x, \frac{\partial u}{\partial x})$ is the modulus of elasticity. Equation (3.1a) is subject to the initial conditions:

$$u\big|_{t=0} = 0 \quad \text{for } 0 \le x \le L$$

$$\left.\frac{\partial u}{\partial t}\right|_{t=0} = 0 \quad \text{for } 0 \le x \le L \tag{3.1b}$$

and boundary condition:

$$\left.(E\frac{\partial u}{\partial x})\right|_{x=L} = \sigma_0 \sin(\omega t) \tag{3.1c}$$

The damping coefficient in the elastic medium of the beam is assumed to be negligible.

A purely analytical solution of Equation (3.1) is difficult to obtain. Therefore, an approximate solution of the problem is sought through a variational formulation of Equation (3.1). At first, the displacement field is discretized in space as following:

$$\hat{u} = \sum_i g_i(t)\phi_i(x) \tag{3.2}$$

where $\phi_i(x)$ are the shape functions and $g_i(t)$ are the corresponding coefficients. $\hat{u}$ is an approximation for u. The weak form of Equation (3.1) is then formulated using the Galerkin technique (Equation (3.3)). Please note that the trial function, $\hat{u}$, and the test function, v, must satisfy the essential and homogeneous boundary conditions, respectively. Same basis functions are used for both $\hat{u}$ and v, as in the ordinary Galerkin method.

$$\int_{x=0}^{L} \{\rho \frac{\partial^2 \hat{u}}{\partial t^2} - \frac{\partial}{\partial x}(E\frac{\partial \hat{u}}{\partial x})\} v dx + \{\left.(E\frac{\partial \hat{u}}{\partial x})\right|_{x=L} - \sigma_0 \sin(\omega t)\} v\big|_{x=L} = 0 \tag{3.3}$$

Equation (3.3) may be reduced to the well-known form of the equation of forced oscillation of a multi degrees of freedom system:

$$\mathbf{M}\frac{\partial^2 \tilde{g}}{\partial t^2} + \mathbf{K}\tilde{g} = \tilde{f} \tag{3.4a}$$

where the superscript ~ is used to denote vectors. The matrices **M** and **K** are given by: $\mathbf{M}_{j,i} = \int_{x=0}^{L} \rho \phi_i \phi_j dx$, and $\mathbf{K}_{j,i} = \int_{x=0}^{L} E \frac{\partial \phi_i}{\partial x}\frac{\partial \phi_j}{\partial x} dx$, and the vector $\tilde{f}$ is given by $f_j = \sigma_0 \sin(\omega t)\phi_j\big|_{x=L}$. $\mathbf{M}_{j,i}$ is the element in the j^{th} row and i^{th} column of **M**. Similar definition goes for **K**. f_j is the j^{th} element of $\tilde{f}$. From Equation (3.4), the solution for the vector $\tilde{g}$ is sought subject to the initial conditions:

$$\begin{aligned} g_i\big|_{t=0} &= 0 \quad \forall i \\ \left.\frac{\partial g_i}{\partial t}\right|_{t=0} &= 0 \quad \forall i \end{aligned} \tag{3.4 b}$$

The above initial conditions follow from Equation (3.1b).

Equation (3.4) is otherwise a linear differential equation except that the matrix **K** changes between closed and open configurations of the crack. Since the excitation is harmonic with frequency ω, the steady state solution for $\tilde{g}$ is also harmonic with the same frequency. However, since the matrix **K** changes between the closed and open states of the crack, the amplitude of oscillation would be different between these two states. Let us assume that the solution for $\tilde{g}$ is $\tilde{g}_1 \sin(\omega t)$ when the crack is closed and $\tilde{g}_2 \sin(\omega t)$ when the crack is open. A strain gage affixed on the beam at $x = x_s$, say, therefore records a strain of $(\varepsilon_1\big|_{x=x_s})\sin(\omega t)$ when the crack is closed and

$(\varepsilon_2|_{x=x_s})\sin(\omega t)$ when it is open. $\varepsilon_1|_{x=x_s}$ and $\varepsilon_2|_{x=x_s}$ are given by: $\varepsilon_1|_{x=x_s} = \sum_i \tilde{g}_{1_i} \left.\frac{\partial \phi_i}{\partial x}\right|_{x=x_s}$ and $\varepsilon_2|_{x=x_s} = \sum_i \tilde{g}_{2_i} \left.\frac{\partial \phi_i}{\partial x}\right|_{x=x_s}$. Since $\tilde{g}_1$ and $\tilde{g}_2$ are different, so are $\varepsilon_1|_{x=x_s}$ and $\varepsilon_2|_{x=x_s}$. Hereafter, it is shown using a numerical example that the amplitude spectrum of a nearly harmonic signal with two different amplitude contents (Equation (3.5)) would contain harmonics of the fundamental frequency (**Figure 3.3**). The amplitude spectrum is computed using Fast Fourier Transform (FFT). It can be observed from **Figure 3.3** that a 1% change in amplitude results in visible even-harmonics in the frequency spectrum. Thus, it is shown in this section that a crack, modeled as a bilinear stiffness element in the structure, can cause production of certain super-harmonics when the structure is excited with a harmonic excitation.

$$y = \begin{cases} \sin(\omega t) & \text{if } y \ge 0 \\ 0.99\sin(\omega t) & \text{if } y < 0 \end{cases} \tag{3.5}$$

where $\omega = 2\pi \times 250 \times 10^3$ Hz, and t is in seconds.

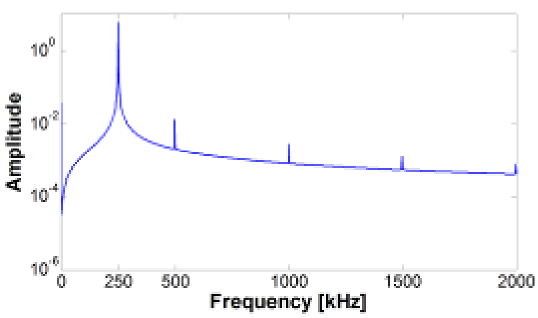

Figure 3.3 Amplitude spectrum of a nearly harmonic signal given by Equation (3.5)

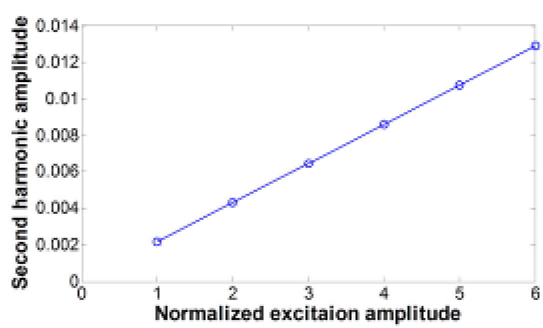

Figure 3.4 Linear variation of the second harmonic amplitude with excitation voltage

Although the bilinear stiffness model of a crack has been used in many studies [54],[57],[58],[56],[11],[59],[60] including the present one, the derivations presented above suggest that this model has certain limitations. First of all, the solution results in a sudden transition in the velocity field when the structure changes its configuration from open crack to closed crack and vice versa. This can be seen as a direct effect of the sharp transition of the local Young's modulus at the crack location when the crack opens or closes (**Figure 3.2**). Secondly, odd-harmonics are not observed through this formulation. Experimental results, however, show the presence of third harmonics in certain cases. Last, but not the least, a system with bilinear stiffness (and transition occurring at zero strain) is one of those rare kinds of nonlinear systems which display homogeneity [61]. As a result, the harmonic amplitudes are predicted by this model to vary linearly with the exciting amplitude. This linear variation is confirmed through numerical simulation by scaling y in Equation (3.5) with integers from two to six, and the result is shown in **Figure 3.4**. On the contrary, experimental results confirm that the harmonic amplitudes vary rather nonlinearly with exciting voltage.

The complexity of the interaction of acoustic waves with real defects is beyond the scope of current theoretical methods. However, some aspects of the wave-crack interaction can be explained, at least qualitatively, with a more detailed model of the crack *viz.* the Greenwood and Williamson's model [62],[59]. Most importantly, the Greenwood and Williamson's model can explain the presence of odd-harmonics and the nonlinear variation of the harmonic amplitudes with exciting voltage.

The proposed technique identifies the presence of cracks in a structure by looking at the harmonics of the exciting frequency in the output signal and their nonlinear relationship to the input amplitude [59]. The amplitudes corresponding to the harmonics can be computed automatically using a Fast Fourier Transform (FFT). It is worth mentioning here that harmonics of the driving frequency are expected to be present even in the output signal from an undamaged specimen because of unknown sources of nonlinearity; *e.g.* nonlinearity in the attached circuit. Therefore, it will be a challenging task to distinguish between nonlinearity produced by a crack and nonlinearity produced by other sources. However, from experimental results it appears that the amplitude of the harmonics due to unknown sources of nonlinearity and the degree of their variation with the excitation voltage are smaller compared to those due to crack-nonlinearity. Therefore, it is assumed in this study that this type of the excitation amplitude dependent nonlinearity is mainly attributed to crack formation. To detect cracks, results obtained from a cracked specimen must be compared with baseline results from the pristine condition of the same specimen. Larger amplitudes of harmonics and greater variation thereof with excitation voltage indicate crack(s) in the structure.

3.5 Experimental results

The effectiveness of the proposed technique has been tested on an aluminum specimen and a steel specimen. The results are detailed in the following sections. To ensure that crack opening and closing happens at the fullest extent, the exciting frequency was always chosen to be the same as the resonant frequency of the transducer-structure system.

3.5.1 Experimental results from aluminum specimen

The overall test configuration and the aluminum test specimen are shown in **Figure 3.5**. The specimen consisted of a rectangular cross-sectional beam 53.34 cm long, 7.14 cm wide and 0.64 cm thick. The crack was made at the centre of the beam-span and runs transversely across the width of the beam.

To produce the crack, a sharp notch was first made at the center of the beam. The beam was then subjected to cyclic loading under an INSTRON loading machine until a visible fatigue crack developed at the notch site. It took about 5,000 cycles to produce a visible crack under 0.2 Hz cyclic loading a tensile stress range at the notch of 180 MPa. Two PSI-5A4E type PZT wafer transducers (1.0 cm x 1.0 cm x 0.0508 cm) were mounted on the beam so that the distance between them was 17.78 cm centered on the crack.

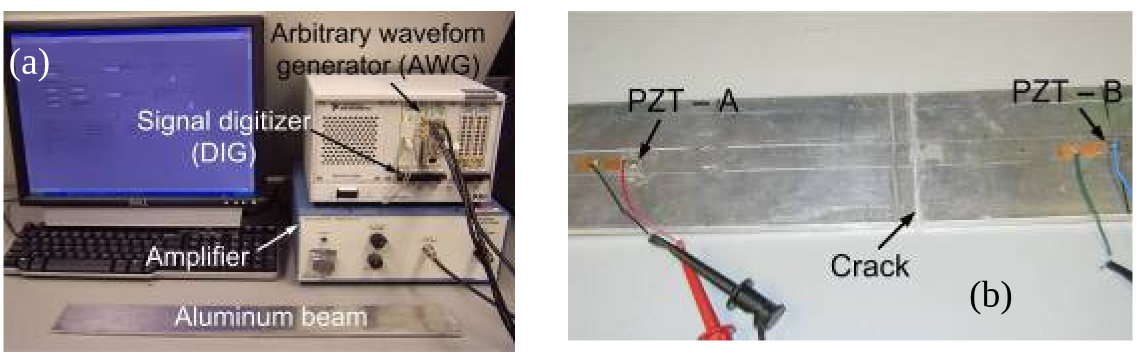

Figure 3.5 Experimental setup for detecting cracks on aluminum beam: (a) Data acquisition system and the undamaged beam (b) Part of the beam showing the crack and the PZT transducers

The data acquisition system was composed of an arbitrary waveform generator (AWG), a high-speed signal digitizer (DIG), and a linear amplifier. The gain of the amplifier was set to two. Using the 16-bit AWG, a Gaussian white noise signal with a

20V peak-to-peak (p-p) voltage was generated and applied to one of the transducers (PZT-A in **Figure 3.5**). PZT-A generated elastic waves and the response was measured at PZT-B. When the waves arrived at PZT-B, the voltage output from PZT-B was measured by the DIG. The sampling rate and resolution of the DIG were 10 MHz and 14 bits, respectively. Thereafter, FFT of the response measured at PZT-B was done and the resonant frequency of the transducer-structure system was identified from the power spectrum. In order to improve the signal-to-noise ratio, the forwarding signals were measured thirty times and averaged in the frequency domain.

Figure 3.6 shows the amplitude spectrum of the output signal for the transducer-structure system when Gaussian white noise input was applied to the actuator. It can be observed from **Figure 3.6** that the resonant frequency of the cracked system did not vary significantly from the resonant frequency of the undamaged system. Therefore, the driving frequency for all subsequent experiments for all undamaged, notched and cracked states of the beam was chosen to be 250 kHz. Another resonant frequency was observed at 493 kHz (**Figure 3.6**). However, the response at 493 kHz was smaller compared to that at 250 kHz. Since the frequency resolution of the DIG was set to as low as 0.1 kHz, 493 kHz is not considered to be the second harmonic of 250 kHz.

Once the resonant frequency of the system was identified, a sinusoidal signal with a 2V p-p and driving frequency equal to the resonant frequency of the system was generated using the same AWG and applied to PZT-A. FFT of the response measured at PZT-B was taken, and the absolute values of the FFT at the second and third harmonics of the driving frequency were noted. Again, the forwarding signals were measured twenty times and averaged in the frequency domain. The above procedure was then repeated with the p-p excitation voltage varying from 2V to 40V with an incremental step of 2V. The same experiment was repeated three times for each state of the specimen (i.e. undamaged, notched and cracked) to see experiment to experiment variation. Note that the linearity of the amplifier used in this study is guaranteed only up to a certain output voltage, and this maximum voltage is determined from the maximum driving frequency (250 kHz) and the capacitance value of the transducer (4 nF) [27]. From the reference, it was found to be safe to apply up to 40V p-p without compromising the linearity of the amplifier.

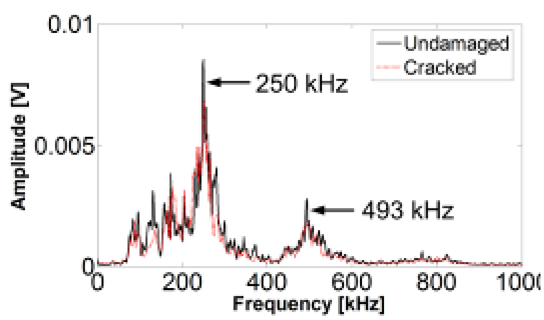

Figure 3.6 Amplitude spectrum of the output signal for Gaussian white noise input at 20V p-p to the aluminum specimen

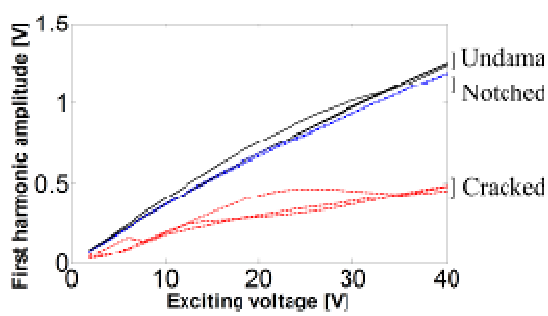

Figure 3.7 Variation of the first harmonic (250 kHz) amplitude in the output signal with excitation p-p voltage – results from three tests on the same aluminum specimen

Figure 3.7 shows that the first harmonic amplitude of the output signal varies more or less linearly with the excitation voltage in the undamaged and notched cases as opposed to exhibiting nonlinear variance in the cracked case. This is an indication of nonlinearity due to crack, and the crack caused the energy corresponding to the driving frequency to be shifted among the higher harmonics. Additionally, the amplitude of the first harmonic is much lower in the cracked beam compared to its undamaged and notched counterparts. The above phenomenon can be attributed to reflection and scattering of acoustic waves from the crack interface. In addition, for the crack case, the amplitude of the first harmonic varies nonlinearly with increasing input voltage.

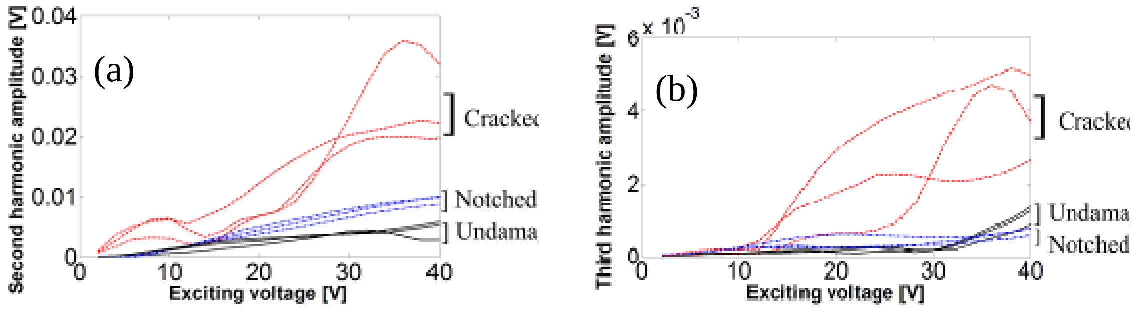

Figure 3.8 Variation of (a) second harmonic (500 kHz) and (b) third harmonic (750 kHz) amplitudes in the output signal with the increasing excitation voltage – results from three tests on the same specimen

It can be observed from **Figure 3.8** that beyond a certain value of the exciting voltage, the second and third harmonic contents of the output signal are much more prominent in the cracked case than in the undamaged or notched cases. The variation of the harmonic amplitudes in the cracked specimen with increasing level of excitation is observed to be nonlinear. The presence of harmonics in the undamaged and notched states can be attributed to unknown sources of nonlinearity such as circuit-nonlinearity. The repeatability of the results shown in **Figure 3.7** and **Figure 3.8** are acceptable in so far as the undamaged, notched and cracked states of the beam can be easily classified.

In conclusion, it can be said that the cracked state of the aluminum beam could be distinguished from its undamaged and notched states by considering the amplitudes of the harmonic components and their variation with the excitation voltage.

3.5.2 Experimental results from steel specimen

A second experiment was performed on a 2.74 m long W6 x 15 (SI: W150 x 22.5) steel beam. The dimensions of the steel specimen are shown in **Figure 3.9**a. Two notches were cut into the bottom (tension) flange near the center of the beam-span as shown in **Figure 3.9**b. These notches served as fatigue crack initiators, and also helped to increase the stress at this section in order to accelerate the development of fatigue cracks. The notches were designed to have a theoretical fatigue life on the order of 40,000 cycles at an applied stress range of 190 MPa. Notches on either side of the web were the same to mitigate any eccentric behavior. Fatigue cracks were expected to form at the sharp root of each notch.

Two PSI-5A4E type PZT wafer transducers (1.0 cm x 1.0 cm x 0.0508 cm) were mounted on the bottom flange of the beam so that the distance between them is 25 cm and the crack initiator falls between the transducers (**Figure 3.10**). Additionally, four electrical resistance crack gages were placed to monitor crack propagation. These were placed at the notch root on both sides of the flange (**Figure 3.10**a).

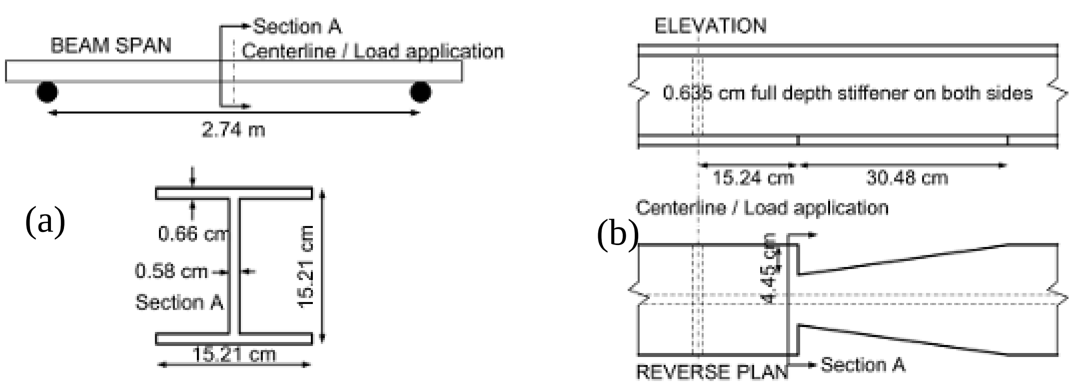

Figure 3.9 Dimensions of the steel W6 x 15 (SI: W150 x 22.5) section: (a) Beam span and cross section (b) Elevation and plan views of the flange in the tension side

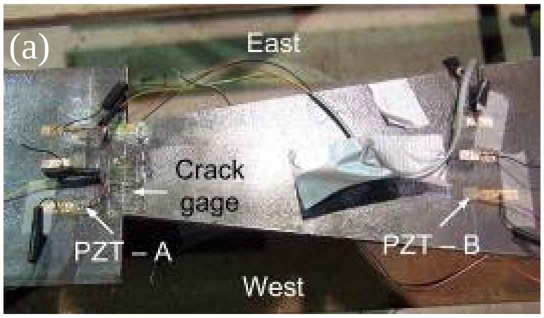

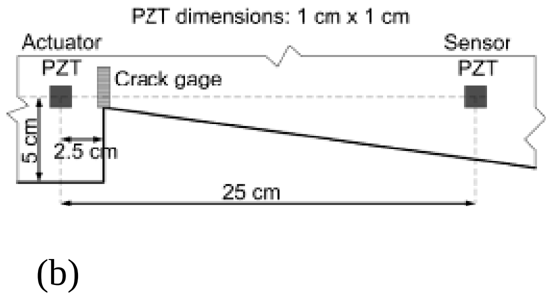

Figure 3.10 Part of the tension flange of the steel beam: (a) The notch, the PZT wafers and the crack gages (b) Schematic figure showing transducers and crack gage locations

To produce the cracks, the beam was loaded in simple mid-span loading over a span length of 2.74 m. The midspan load was cycled from 4.5 kN to 40.5 kN resulting in a load range of 36 kN. Cycling was carried out at a rate of 1 Hz. The 36 kN applied load corresponds to a tensile stress range of 190 MPa at the notch root of the tension flange. The minimum stress, at an applied load of 4.5 kN is 22.7 MPa. The loading set-up is shown in **Figure 3.11**. The notch site was continuously monitored for crack initiation. After approximately 9,000 cycles, cracks at each notch root were identified by the crack gages and could be observed visually. **Figure 3.12** shows the crack on the Western side of the tension flange propagating beneath a crack gage after approximately 18,000 cycles.

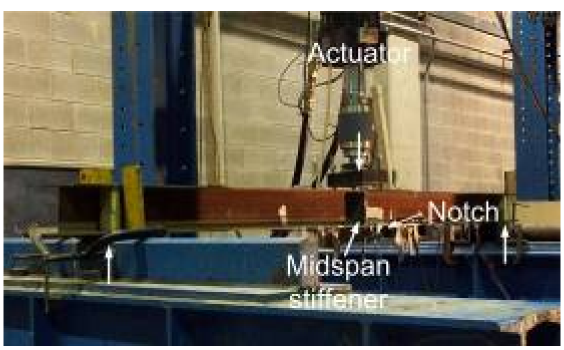

Figure 3.11 Loading configuration for the experiment on the steel beam

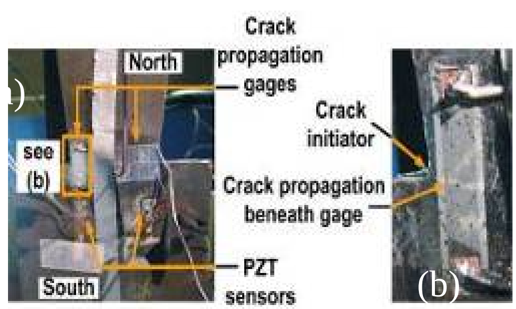

Figure 3.12 Part of the tension flange of the steel beam showing the location of the crack

Figure 3.13 shows the history of crack propagation in the West flange of the steel beam. Following every few thousand cycles (after 0, 5000, 10000, 12000, 14000, 18000, 22000 and 24000 cycles to be precise), the cyclic loading was paused and a static load of 22 kN (average of fatigue load stress range) was applied to the beam. Under this constant load, data from the PZT transducers were collected following the same procedure that was performed on the aluminum beam. It should be mentioned that the resonant frequency of the transducer-structure system was measured once at the onset of loading and once after 12,000 cycles when the crack already existed (**Figure 3.14**). **Figure 3.14** shows the amplitude spectrum of the output signal for the transducer-structure system when a Gaussian white noise input is given to the actuator. It can be observed from **Figure 3.14** that the resonant frequency of the cracked system does not vary significantly from the resonant frequency of the undamaged system. The driving frequency for all subsequent experiments was therefore chosen to be 350.5 kHz, and the amplitude spectrum was not measured again due to time constraints. For a Gaussian white noise, the energy is distributed among so many frequencies that the second harmonic of a particular frequency (caused by the crack nonlinearity, which is usually small) is hardly discernable.

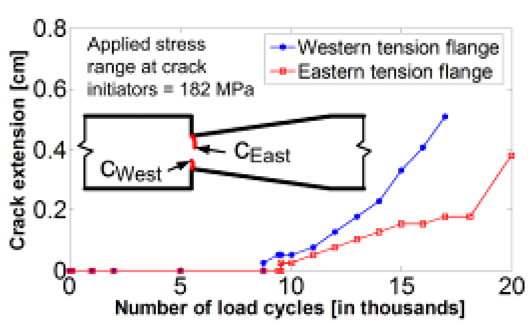

Figure 3.13 Propagation history of the crack emanating from the notch-tip of West part of the tension flange of the steel beam

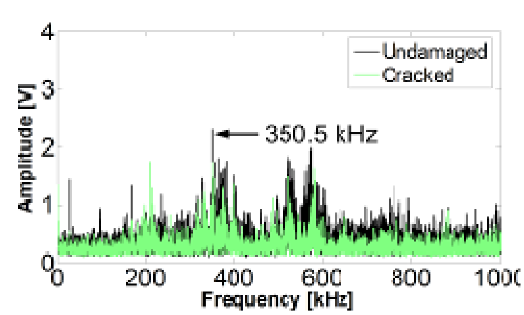

Figure 3.14 Amplitude spectrum of the output signal for Gaussian white noise input at 20V p-p to the steel specimen

The results discussed in this section were obtained from the West side of the tension flange where collected data was more consistent. A fatigue crack also formed on the East side of the flange and was successfully captured by the crack gages. However, the PZT-based system failed to identify this crack before twenty thousand cycles. This fact does not give the crack gages any edge over the PZT-based system because in practice the exact location of crack initiation will hardly be known in advance and the crack gages must traverse the crack (crack gages are conventionally applied following crack initiation to monitor crack propagation). The successful detection of a crack using PZT transducers depends upon a number of factors viz. nature of the crack, position of the PZT relative to the crack etc. It is difficult to specify which of the above factor(s) is (are) responsible for the successful detection of the crack on Western part of the flange and for the failure to detect crack on the Eastern part of the tension flange.

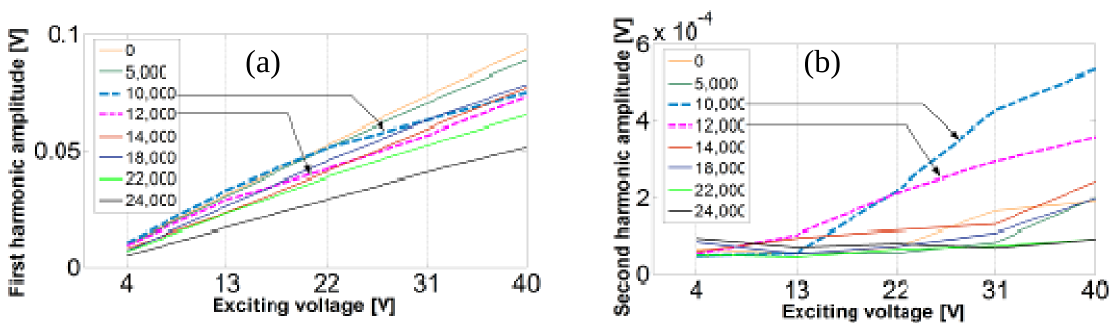

Figure 3.15 Variation of (a) first harmonic (350.5 kHz) and (b) second harmonic amplitudes (701 kHz) in the output signal with the increasing excitation p-p voltage after given number of cycles of loading; Crack initiated around 8790 cycles

Figure 3.15a suggests an increased acoustic nonlinearity at approximately ten thousand cycles when the first harmonic amplitude varies nonlinearly with the excitation voltage. The presence of the second harmonic is also significant around ten thousand cycles (**Figure 3.15**b). These observations combined with observations from the crack gages (**Figure 3.13**) imply that the PZT-based active sensing system could identify the damage near its inception.

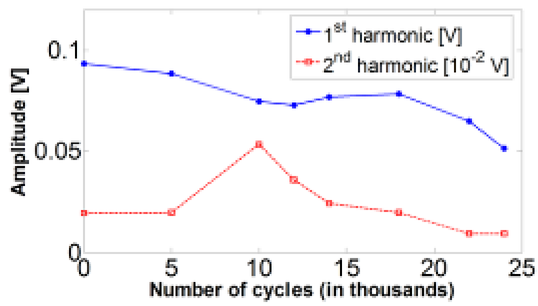

Figure 3.16 Variation of first (350.5 kHz) and second harmonic (701 kHz) amplitudes in the output signal with respect to the number of loading cycles for an excitation voltage of 40V p-p

Figure 3.16 shows the variation of the first and second harmonic amplitudes in the output signal with the increasing number of loading cycles for an excitation voltage of 40V p-p. In **Figure 3.16**, the first harmonic amplitude shows a general downward trend which can be attributed to reflection and scattering of acoustic waves from the crack interface. However, around ten thousand cycles, the first harmonic amplitude dips unusually which may be explained by energy shifting to the higher harmonics. The same figure also shows the trend of the second harmonic amplitude which is unusually high around ten thousand cycles. The following may therefore be inferred from the above observations: the nonlinearity effects became prominent at the inception of the crack but its manifestation decreased steadily with increasing length of the crack and became indiscernible after fourteen thousand cycles. There are two possible explanations for this observed phenomenon. First, the crack tip gets wider as crack propagates, and crack opening and closing becomes insignificant. Secondly, the crack tip moves away from the line of sight of the PZT actuator-sensor couple. This results in oblique incidence of the acoustic waves on the crack tip which is not strong enough to produce crack opening and closing. Whatever the reason, this observation suggests a highly localized nature of the sensing technique described in this study.

In conclusion, it can be said that the crack in the West part of the bottom flange of the steel beam could be identified at its inception by looking at the amplitudes of the harmonic component and their nonlinear variation with excitation voltage.

3.6 Chapter summary

The objective of this study was to propose an easily automated crack detection technique in metallic structures using agile PZT transducers. Preeminent harmonics in the response signal from cracked specimens were observed as the input power of the driving PZT-wafer increased. The harmonic amplitudes also showed nonlinear variation with the increasing excitation voltage in cracked specimens. The proposed technique identifies the presence of cracks by looking at two features: harmonics and their nonlinear relationship to the input amplitude. Although the essence of crack detection remains the same for both the specimens, the effect of nonlinearity is far less pronounced in the case of the steel beam (e.g. compare

Figure 3.8a and **Figure 3.15**b). Since the size and stiffness of the steel specimen are greater than those of the aluminum plate, the amplitude of vibration in steel is smaller compared to that in aluminum for the same level of excitation voltage. Because of the low amplitude of oscillation, the extent of crack opening and closing is reduced and hence nonlinear wave interaction does not take place at a measurable level for the steel specimen. Experimental results also showed the presence of second and third order harmonics in the undamaged and notched states of a structure caused by other sources of nonlinearity such as the instrumentation and the adhesive layers. Further study is warranted to address the issue of distinguishing the nonlinearity due to cracks from nonlinearity due to other sources. Nevertheless, it is possible to identify cracks in a specimen by looking at the greater magnitude of the harmonics and higher amount of their variation with the excitation voltage as compared to those in the pristine state of the structure (it is assumed that the nonlinear effects are in some way additive). Another interesting study would be to investigate the effectiveness of this technique by varying the position to the PZTs relative to the crack. At this point, it can be said that the two main concerns are: (1) the distance of an actuator or a sensor from the crack, and (2) the orientation of the crack relative to the line of sight between the actuator and the sensor. Since guided waves are known to propagate large distances without much attenuation, it is envisioned that the effectiveness of the proposed technique would not be significantly affected by the relative location of the crack and the PZTs. This claim, however, needs to be corroborated by experimental data and relevant work in this direction is considered a part of the authors’ future work.

4. Crack detection in metallic structures using nonlinear ultrasonics: II. Nonlinear system identification through coherence measurement

4.1 Motivation

In the previous chapter we investigated the generation of superharmonics which is but one particular manifestation of the nonlinearity in the acoustic medium due to a crack. In this chapter, we obtain the coherence measurement of the transducer-structure system using an electromagnetic impedance circuit. The deviation of coherence from unity is a cumulative manifestation of the nonlinearity in the system.

4.2 Chapter abstract

An electro-mechanical impedance based method using the principles of nonlinear acoustics is developed in this study to detect cracks in metallic structures. Lead-Zirconate-Titanate (PZT) transducers are used for exciting and measuring acoustic waves in a structure. Cracks in a structure give rise to a set of nonlinear boundary conditions in the acoustic field. This phenomenon affects the coupled electro-mechanical impedance of the PZT-structure system in a way that the measured impedance varies with the amplitude of the exciting voltage. In other words, the current through the electrical circuit varies nonlinearly with the input voltage. This nonlinear relationship can be captured by computing the coherence function between the input voltage and the resulting current. Experimental results from an undamaged structure show that coherence value remains close to unity throughout the exciting frequency range. However, significant drop below unity was observed at certain frequencies in the data obtained from a cracked specimen. The above observation is exploited to detect the defect on the structure.

4.3 Chapter introduction

Two very popular techniques for crack detection in metallic structures are: (1) electro-mechanical impedance-based method [9],[10] and (2) ultrasonic testing using guided waves [7]. In the impedance method, the coupled electro-mechanical impedance of the PZT-structure system is obtained from a cracked structure and compared with that of the undamaged structure to identify the presence of defect. It should be noted that the concept of impedance is implicitly defined for linear systems. This chapter studies the effect of a crack on the impedance of a transducer-structure system in a different way than the traditional impedance-based methods do. The nonlinear boundary conditions at a crack interface affect the coupled electro-mechanical impedance of the PZT-structure system in a way that the measured impedance varies with the amplitude of the exciting voltage. In other words, the current through the electrical circuit varies nonlinearly with the input voltage. This nonlinear relationship can be captured by computing the coherence function between the input voltage and the resulting current. In this way, this chapter presents a unique hybrid of the impedance technique and the nonlinear acoustic techniques for crack detection. This hybrid technique uses the same circuit used for conventional impedance methods (**Figure 4.1**). The technique was implemented using light PZT wafers which can be easily surface-mounted or embedded in the structure. It should be noted here that ordinary coherence and bi-coherence functions have been used in the past to detect acoustic nonlinearity produced by a crack [56],[11]. However, two transducers were used in those studies, - one of which acted as an actuator and the other as a sensor. Thereafter, the coherence or bi-coherence relationship between the input waveform at the actuator and the measured output waveform at the sensor were computed to identify any presence of nonlinearity.

This chapter is organized as follows. First, the theoretical development for the proposed method is provided. Then, experimental studies performed to verify the effectiveness of the proposed technique are discussed. Finally, this chapter concludes with a brief summary.

4.4 Theory

This section provides the theoretical background for the crack detection technique presented in this chapter. First, it is explained why the output current (i_{out}) is nonlinearly related to the input voltage (v_{in}) for a cracked specimen, as opposed to an undamaged specimen where the relationship is linear. Then it is shown how the nonlinearity can be captured by computing the coherence function between the input voltage and output current.

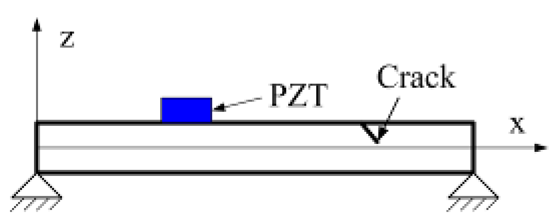

Figure 4.1 A schematic of a cracked beam with a surface mounted PZT.

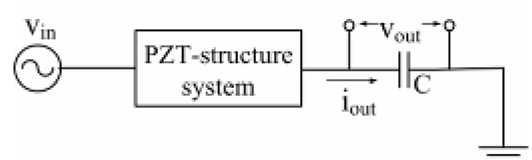

Figure 4.2 A schematic of the voltage divider circuit.

Consider a PZT patch attached to a simply supported beam (**Figure 4.1**). The circuit is schematically shown in **Figure 4.2**. The current through the PZT-patch is related to the voltage across the same through a function, say H (Equation (4.1)). Please note that the current through the PZT-patch is same as the output current ($i_{out}(t)$). Also note that the voltage across the external impedance, which is a capacitor for the present study, is linearly related to the current through it ($i_{out}(t)$) by a linear function K_C.

$$i_{out}(t) = \mathrm{H}[v_{in}(t) - \mathrm{K}_C[i_{out}(t)]] \tag{4.1}$$

Now, the acoustic medium in an undamaged aluminum beam can be considered to be linear for all practical purposes. Assuming that the attached instrument also behaves mostly linearly (which is a valid assumption in most cases), the coupled electro-mechanical response of the PZT-undamaged-structure system should be linear. In other words, the function H is a linear mapping. Since K_C is also linear, Equation (4.1) can be rearranged to get the following:

$$i_{out}^{und}(t) = \Lambda[v_{in}(t)] \tag{4.2}$$

where Λ is a linear function that maps the input voltage $v_{in}(t)$ to the output current $i_{out}^{und}(t)$. The superscript '*und*' stands for undamaged.

However, cracks in a structure give rise to a nonlinear acoustic medium [10-12]. This makes the coupled electro-mechanical response of the PZT-cracked-structure system nonlinear and therefore H becomes nonlinear. Using the above piece of information in Equation (4.1), we have:

$$i_{out}^{dam}(t) = \mathrm{N}[v_{in}(t)] \tag{4.3}$$

where N is a nonlinear function that maps the input voltage $v_{in}(t)$ to the output current $i_{out}^{dam}(t)$. The superscript '*dam*' stands for damaged.

Now, let $V_{in}(\omega)$ and $I_{out}(\omega)$ be the Fast Fourier Transforms (FFT) of the input voltage ($v_{in}(t)$) and the output current ($i_{out}(t)$) respectively:

$$V_{in}(\omega) = \Im[v_{in}(t)],\ I_{out}(\omega) = \Im[i_{out}(t)] \tag{4.4}$$

Here, ω stands for frequency. The ordinary coherence function $\gamma(\omega)$ between the input voltage and output current may then be defined as:

$$\gamma^2(\omega) = \frac{\left|S_{vi}(\omega)\right|^2}{S_{vv}(\omega)S_{ii}(\omega)} \tag{4.5}$$

where the terms in Equation (4.5) are defined as follows.

$$\begin{aligned} &S_{vv}(\omega) = E[V^*(\omega)V(\omega)],\quad S_{ii}(\omega) = E[I^*(\omega)I(\omega)] \\ &and \quad S_{vi}(\omega) = E[V^*(\omega)I(\omega)] \end{aligned} \tag{4.6}$$

E[X] is the expectation of a variable *X* and Y^* is the complex conjugate of a complex quantity *Y*. The ordinary coherence function is often used as a measure of how well the output is linearly related to the input at each frequency [63]. In other words, the coherence function is a measure of the linearity of a system. Its value is bounded between zero and one and the coherence value for a linear system (in this case the PZT-undamaged-structure system) has to be equal to one throughout the exciting frequency range. However, significant drop below unity may be expected for a nonlinear system (in this case the PZT-cracked-structure system) at any frequency. Thus, by looking at the ordinary coherence function, one can distinguish an undamaged structure form a cracked one. It is assumed that all the sources of excitation in the frequency range of investigation are known. Unaccounted sources of excitation can cause drops in the coherence spectrum as well.

It is worth mentioning here that the nonlinear effect due to a crack is relatively small. Moreover, the nonlinearity is mainly attributed to crack opening and closing which happens only if the amplitude of the propagating wave is large enough to produce the crack opening and closing. Consequently, the crack-nonlinearity is most pronounced near the resonant frequency of the system where the amplitude of the traveling wave is large. Based on the above discussion, the coherence value for a cracked specimen is expected to fall significantly below unity at certain frequencies while it should be close to unity at certain other frequencies.

4.5 Experimental results

4.5.1 Specimens and experimental setup

The crack detection technique was tested on two aluminum specimens, one of which is intact while the other has a crack. The specimens along with the dimensions are shown in **Figure 4.3**. To produce the crack, a notch was first made on the beam. The beam was then subjected to cyclic loading under an INSTRON loading machine until a visible fatigue crack was developed at the notch site. It took about 5,000 cycles to produce a visible crack under 0.2 Hz cyclic loading and a tensile stress range of 180 MPa at the notch site. Two PZT-patches were then attached on the aluminum beams at identical locations. Please note that the PZT-patch on the cracked specimen is 10 cm away from the crack.

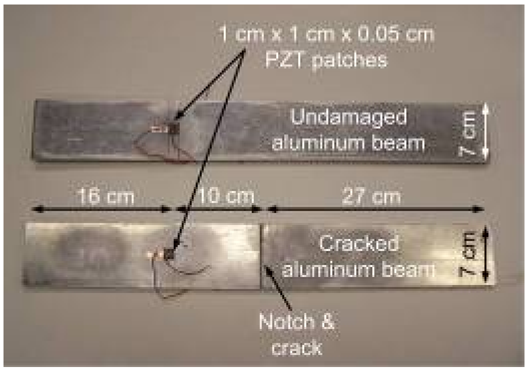

Figure 4.3 Test specimens. Both beams are 6 mm thick.

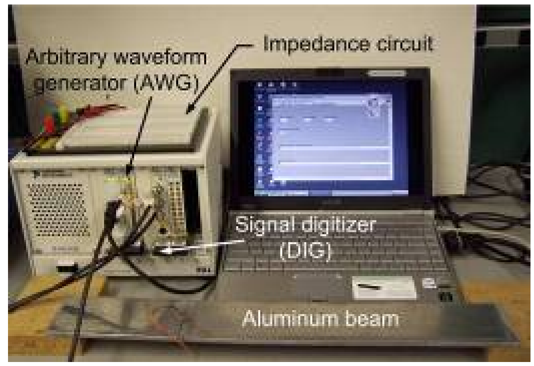

Figure 4.4 Test setup.

The data acquisition system was composed of an arbitrary waveform generator (AWG), a high-speed signal digitizer (DIG), and an impedance measurement circuit (**Figure 4.4**). The input voltage (v_{in} as in **Figure 4.2**) was applied to the PZT using the 16-bit AWG and the voltage output (v_{out} as in **Figure 4.2**) as well as the voltage input were measured by the DIG. The sampling rate and resolution of the DIG were 10 MHz and 14 bits, respectively. The coherence value between the input voltage (v_{in}) and the output current (i_{out}) can be mathematically shown to be equal to the coherence value between the input voltage (v_{in}) and the output voltage (v_{out}). The fact that the output voltage (v_{out}) and the output current (i_{out}) are linearly related may be taken as a hint for the proof. Note that v_{in} is the actual input voltage that goes into the system, and not the digital input waveform. This was achieved by bifurcating the input cable and measuring the input voltage through a DIG channel. In this way, the unwanted nonlinearity of the

AWG was avoided. Using this setting, the AWG is no more a part of the system for which the coherence is measured.

4.5.2 Experimental results

Please recall from the 'theory' section that in order for the crack nonlinearity to be manifested, the traveling waves should have high amplitude. This is achieved when the PZT-structure system is excited near its resonant frequency. Therefore, a range of frequencies which is near the resonant frequency of the system was identified for each aluminum specimen by the following procedure. Using the 16-bit AWG, a Gaussian white noise signal with a ± 10 peak-to-peak voltage was generated and applied to the transducer. The admittance spectrum of the PZT-structure system was obtained by evaluating the H_2 estimate of the Frequency Response Function (FRF) between the input voltage and the output current (**Figure 4.5** and **Figure 4.6**). The H_2 estimate of the FRF between the input voltage and output current is given by:

$$H_2(\omega) = \frac{E[I_{out}(\omega) I_{out}^*(\omega)]}{E[V_{in}(\omega) I_{out}^*(\omega)]} \tag{4.7}$$

The symbols in Equation (4.7) have the same meanings as before. In the present study, the expectations were performed on twenty pairs of signals. Based on the admittance spectrum, a 100 kHz zone containing the resonance frequency is selected. For the undamaged specimen, the selected frequency zone was 130-230 kHz (**Figure 4.5**) and for the cracked specimen it was 200-300 kHz (**Figure 4.6**).

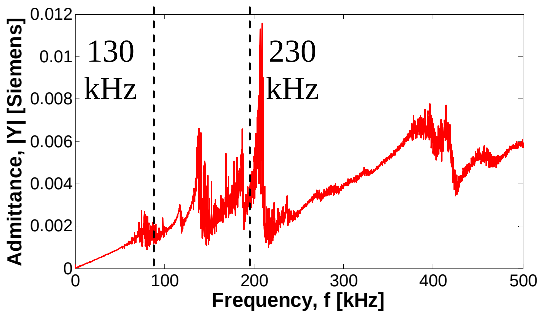

Figure 4.5 Frequency response of the PZT-undamaged-structure system for a Gaussian white noise input.

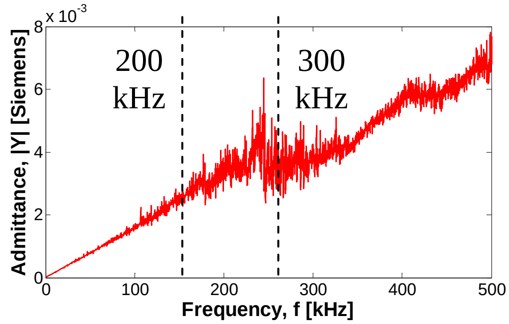

Figure 4.6 Frequency response of the PZT-cracked-structure system for a Gaussian white noise input.

After the frequency zone was selected, each specimen was excited by a frequency swept signal [19] band-limited within the corresponding frequency range. This was repeated forty times with the peak-to-peak exciting voltage varying from 0.5 V to 20 V with a step of 0.5 V. Sample excitation signals (digital) with 20 V peak-to-peak voltage are shown in **Figure 4.7** (undamaged specimen) and **Figure 4.8** (cracked specimen). The coherence functions computed between the input voltage and the output current for the frequency swept inputs are shown in **Figure 4.9** and **Figure 4.10** for the undamaged and damaged specimens respectively. Note that the expectations (as in Equation (4.6)) were performed on the forty pairs of input and output data described above. The same set of experiments was performed three times to check for repeatability (**Figure 4.9** and **Figure 4.10**).

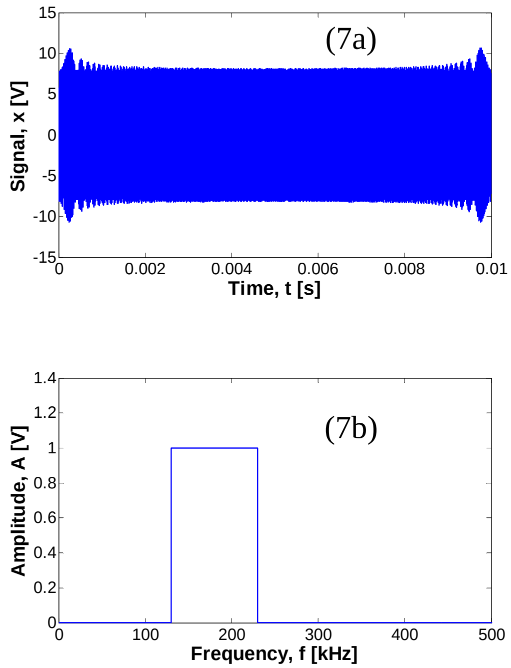

Figure 4.7 Frequency swept input signal (digital) applied to the undamaged system for damage detection: (a) time-domain representation (b) frequency-domain representation

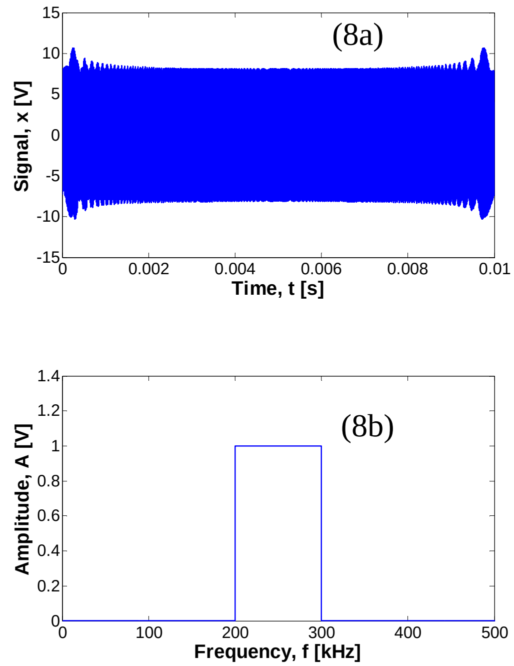

Figure 4.8 Frequency swept input signal (digital) applied to the damaged system for damage detection: (a) time-domain representation (b) frequency-domain representation.

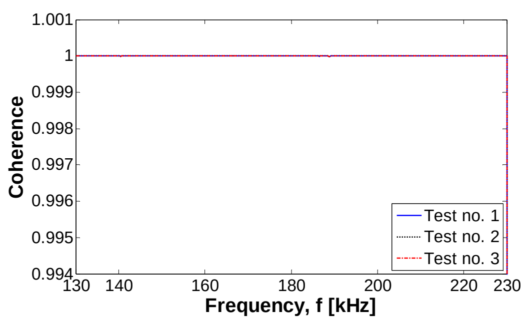

Figure 4.9 Coherence spectrum of the PZT-undamaged-structure system for the frequency swept input shown in **Figure 4.7**.

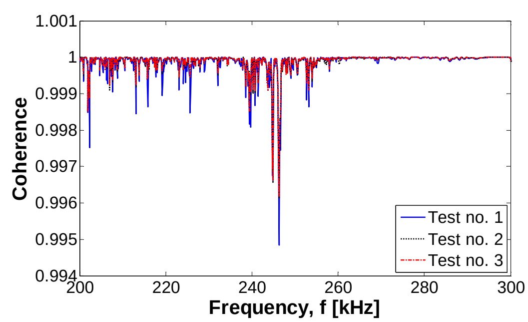

Figure 4.10 Coherence spectrum of the PZT-cracked-structure system for the frequency swept input shown in **Figure 4.8**.

It can be observed from **Figure 4.9** that the coherence values for an undamaged specimen stay equal to unity (when the values are considered up to the third decimal place) for the entire exciting frequency range. However, for a cracked specimen, there is observable drop below unity which clearly indicates nonlinearity in the system (**Figure 4.10**). The drop below unity is still small though (about five parts in a thousand), - which indicates that crack nonlinearity, although distinguishable, is quite small. Another fact worth mentioning is that the deviation in coherence value for the damaged specimen is most prominent at around 250 kHz (**Figure 4.10**) which is suspiciously close to the resonant frequency of the PZT-cracked-structure system (**Figure 4.6**). The above fact reinforces the theory that nonlinearity in a cracked structure is caused by crack opening and closing, and its manifestation is most prominent near the resonant frequency of the system where the amplitude of the propagating waves is maximum.

4.6 Chapter summary

An impedance based crack-detection technique in metallic structures using the principles of nonlinear acoustics was introduced in this chapter. This hybrid of the impedance techniques and the nonlinear techniques for crack detection uses the same circuit as used in conventional impedance-based methods. Further, this technique identifies a crack in the structure through verification of linearity of the PZT-structure system. An intact structure is expected to behave linearly whereas a crack in the structure would make the entire system behave nonlinearly. The system identification is done by computing the ordinary coherence function between the input voltage and output current. Significant deviation of the coherence values from unity over the exciting frequency range may be correlated to system nonlinearity and hence damage. The technique was implemented using light PZT-wafers surface mounted on two aluminum specimens. One of the aluminum specimens was intact and the other was cracked. The experimental results indicate observable deviation of the coherence values from unity in the data collected from the cracked specimen. However, coherence values from the intact specimen stayed close to unity throughout the exciting frequency range. The experimental results were thus found to be consistent with the theory. The unwanted nonlinear effects of the AWG were bypassed by measuring the input voltage in real time rather than considering the digital input waveform for coherence measurements. However, nonlinearity due to the impedance circuit or other instrumentations (like the attached PZT-wafers) cannot be avoided. Although such nonlinear effects were not observed in the present study, nonlinearity in instrumentation may cause significant deviation from unity in the coherence function even for an undamaged structure, thereby producing false alarms. As a closing note, the coherence spectrum obtained from the undamaged specimen is shown again, only this time the y-axis is magnified revealing the small nonlinearities due to instrumentation and the adhesive layer.

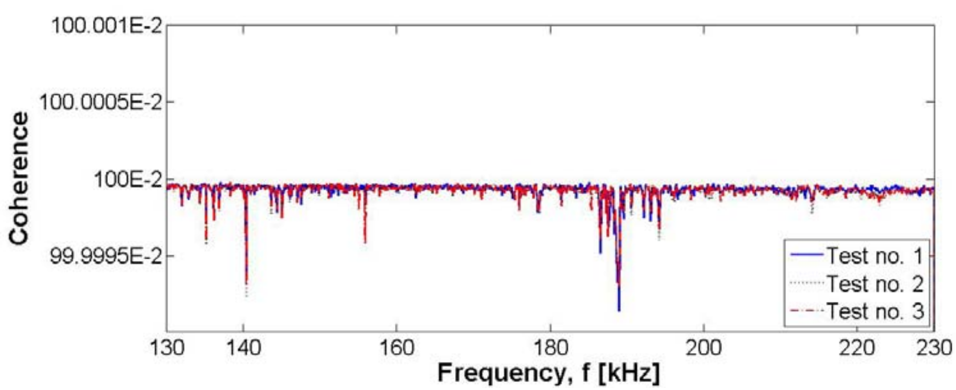

Figure 4.11 Coherence spectrum of the PZT-undamaged-structure system (**Figure 4.9**) with a magnified y-axis (Input: frequency-swept function)

5. Damage detection from wavefield images: I. Imaging ultrasonic waves in structures with complex geometry

5.1 Motivation

A scanning laser Doppler vibrometer allows one to observe the ultrasonic wavefield across the surface of the target specimen. Interaction of ultrasound with a defect produces interesting local phenomena in the vicinity of the defect. Such interaction can be highlighted using proper signal processing so that the damage stands out in the background of the residual undamaged area. Here, the undamaged area serves as a "baseline" for damage detection purpose. The technique is still baseline-free by our definition, because the scanning is done on the current state of the structure only. This chapter describes some groundwork on what to expect from the wavefield images obtained using a laser vibrometer. The next chapter is specifically about detecting delamination and disbond in composite specimens.

5.2 Chapter abstract

Ultrasonic wave propagation through metallic and composite structures is of considerable interest in the context of non-destructive testing and evaluation (NDT&E) and structural health monitoring (SHM). This chapter presents images of ultrasonic wavefields in specimens varying in structure and composition. The ultrasonic waves are generated in the structures using surface bonded piezoelectric wafer actuators. A scanning laser Doppler vibrometer (SLDV) is used to image out-of-plane velocity field across the surface of the structure. The images thus obtained give valuable insight into the interaction of ultrasonic waves with various structural components (such as stiffeners, bolts, lap joints and variation in thickness etc.) as well as the interaction with damages (such as impact damage). A proper understanding of such interactions would hopefully lead to improved damage detection in complex engineering structures in future.

5.3 Chapter introduction

Various types of transducers can be used to excite and sense guided waves. The most commonly used transducers include angled piezoelectric wedge transducers, comb transducers and electromagnetic acoustic transducers and surface-bonded piezoelectric wafer transducers[7],[64-67]. Some transducers are mainly used for sensing applications such as polyvinylidene fluoride (PVDF) and fiber optic sensors [68],[69]. Although each transducer mentioned above has its own set of strengths and weaknesses, all of them are primarily used for discrete point measurements. Such transducers are inadequate for the purpose of the present study which is to create images of the ultrasonic fields in structures. It is practically impossible to place a dense array of transducers commensurate with the short wavelength of ultrasonic waves. A potential solution to this problem is to use non-contact scanning laser techniques for creating wavefield images with a high spatial resolution. The present study uses an SLDV to remotely sense the ultrasonic field in a structure. Laser based generation and measurement of ultrasound have been studied in the past [70],[17],[18]. More recently, Leong et al. [71] studied the interaction of guided waves with fatigue cracks in a plate using SLDV. It is worth mentioning here that the wavefield imaging discussed above is different from traditional ultrasonic imaging in which time-of-flight information is used to image all reflectors in the ultrasonic medium

[72],[73]. This traditional ultrasonic imaging requires precise information about the material as well as geometry of the structure. Therefore, guided wave imaging using SLDV is more suitable for complex engineering structures.

The objective of the present study is to expand the scope of using laser vibrometry to detect defects in complex structures [74]. To this effect, the interactions of ultrasonic waves with structural components (such as bolts, stiffeners and joints) have been studied and attempt has been made to distinguish such interactions with those happening at defect locations.

The chapter is organized as follows. First, the experimental setup is described. This is followed by a report of the experimental results. The chapter then concludes with a brief summary.

5.4 Experimental setup

Figure 5.1 shows the overall configuration of the experimental setup used in this study. An arbitrary waveform generator with a piezoelectric transducer and a power amplifier are used to generate guided waves in the test article. Then, the guided wave responses in a specified area are scanned by a laser vibrometer, and the data is collected by a built-in data acquisition system. The data is then exported to the MATLAB® software program and processed on a personal computer. In the following subsections, each aspect of the proposed experiment is described in further details.

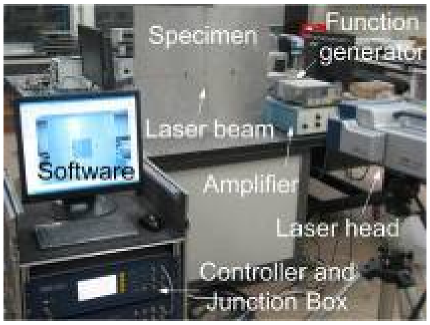

Figure 5.1 Experimental set up for a typical laser scan

Figure 5.2 6 mm thick composite plate instrumented with Kapton coated PZTs

5.4.1 Guided wave excitation

User specified waves are generated using an arbitrary waveform generator. In our experiments, a 6 peak tone burst signal at 100 kHz driving frequency is used. The excitation voltage is amplified up to ±50 V using a power amplifier and applied to a piezoelectric transducer (made from lead zirconate titanate, better known as PZT). 5AH type PZT transducers are used and the actual sizes of the transducers are different for different experiments. The excitation signal triggers data collection so that the excitation and response signals are properly synchronized.

5.4.2 Guided wave sensing

The guided waves generated by the PZT transducer are measured by a *Polytec PSV-400* SLDV. The 1D vibrometer used in this study measures the out-of-plane velocity across the scanned surface of the specimen using the principle of Doppler frequency-shift effect on light waves. The scanning is done by steering the laser beam to the desired location using deflection mirrors which are built into the laser head. The time response at each measurement point is averaged 20 times to improve the signal to noise ratio, and a band pass filter is applied to eliminate exogenous noise outside the driving frequency band. A sampling rate of 2.56 MHz and a sensitivity of 10 mm/s/V are used for all cases. In order to create a high resolution wavefield image it is important to have small measurement grid size compared to the wavelengths of the guided waves. Assuming a scanning area of 100 cm^2 with 100×100 measurement points and 20 times averaging, it takes about 1-2 hours to collect all the time signals and create wave propagation images. Once all the data are collected, it is converted to a universal file format and exported to the MATLAB® software program.

5.4.3 Signal processing

Once all the data are imported to MATLAB® all further processing of the data is conducted using MATLAB®. Basically, three operations are conducted here. First, the raw time signals are passed through a wavelet or a Butterworth filter to reduce noise and examine wave propagation within a narow frequency band. Second, a video of wave propagtion in the structure is constructed from the out-of-plane velocity information using the MATLAB® graphics tools. Third, the mean-square value of out-of-plane velocity at each scan point is computed at a given point of time:

$$E(x,y,t) = \frac{1}{2} \int_{\tau=0}^{t} v^2(x,y,\tau) d\tau \tag{5.1}$$

where $E(x,y,t)$ is the mean-square value at the scan location (x,y) at time t; $v(x,y,\tau)$ is the out-of-plane velocity at the same scan location at time $\tau\ (\forall \tau \leq t)$. The mean square value represents the mass-normalized cumulative kinetic energy which is the total amount of ultrasonic energy that has passed through a certain point until that time. Note that the kinetic energy corresponding only to the out-of-plane velocity is captured using a 1D vibrometer.

5.5 Experimental results

The ultrasonic images obtained from various specimens are reported in this section (**Figure 5.2-Figure 5.26**).

Figure 5.2 shows a 6 mm thick composite plate instrumented with Kapton coated circular PZTs. The actuator as well as the scan area is indicated in the figure. Since the target structure is a plate, Lamb waves are expected to propagate through the structure

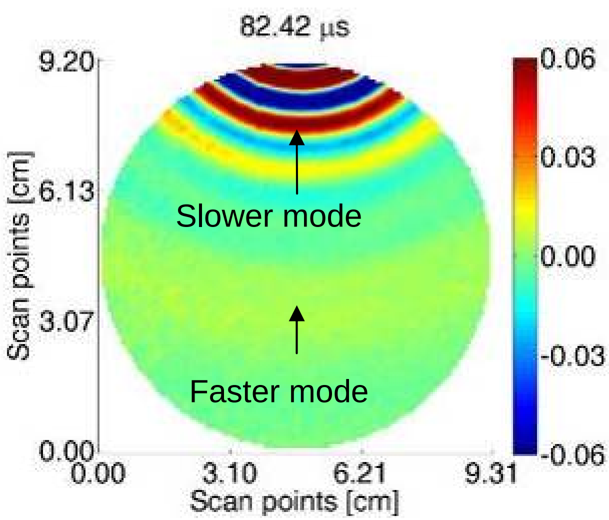

Figure 5.3 Contour plot of the out-of-plane ultrasonic velocity field for the specimen shown in **Figure 5.2**.

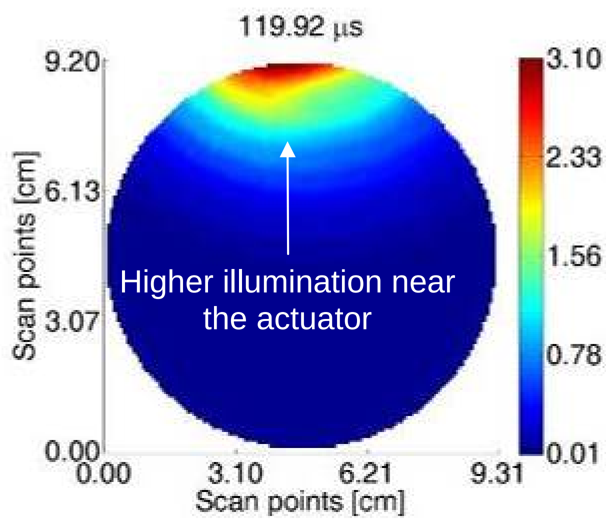

Figure 5.4 Contour plot of the cumulative kinetic energy field for the specimen shown in **Figure 5.2**.

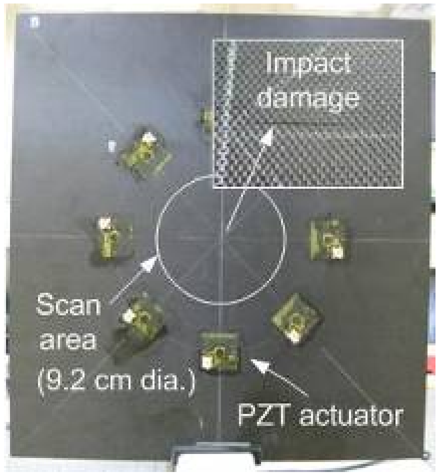

Figure 5.5 1.8 mm thick composite plate instrumented with Kapton coated PZTs.

(Rose 1999). **Figure 5.3** and **Figure 5.4** show the out-of-plane ultrasonic velocity field and the cumulative kinetic energy field respectively after 82.42 µs and 119.92 s from the initiation of the scan. It can be observed from **Figure 5.3** that the faster traveling symmetric mode (also noticeable by its longer wavelength) has lower amplitude of out-of-plane velocity than the slower anti-symmetric one. **Figure 5.4** demonstrates the phenomenon of divergence of ultrasonic waves radiating from a source (PZT actuator). The region near the source experiences higher intensity compared to the ones away from it.

Figure 5.5 shows another composite plate, this one with impact damage at the center. In **Figure 5.6** and **Figure 5.7**, high ultrasonic activity is observable in the defect location. This manifests as higher out-of-plane velocity and higher cumulative kinetic energy in the defect zone than in the surrounding area.

The next experiment demonstrates the effect of foreign substances on the wave propagation through a structure. The actuator assembly shown in **Figure 5.8** includes a pair of metallic connectors which add substantial mass to the 1.8mm thick composite plate.

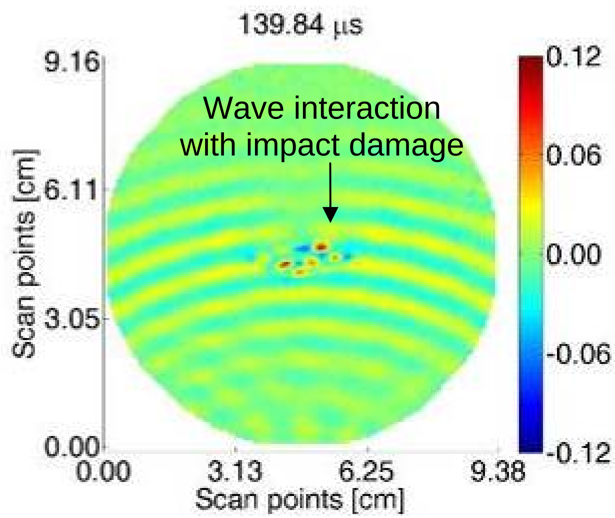

Figure 5.6 Contour plot of the out-of-plane ultrasonic velocity field for the specimen shown in **Figure 5.5**.

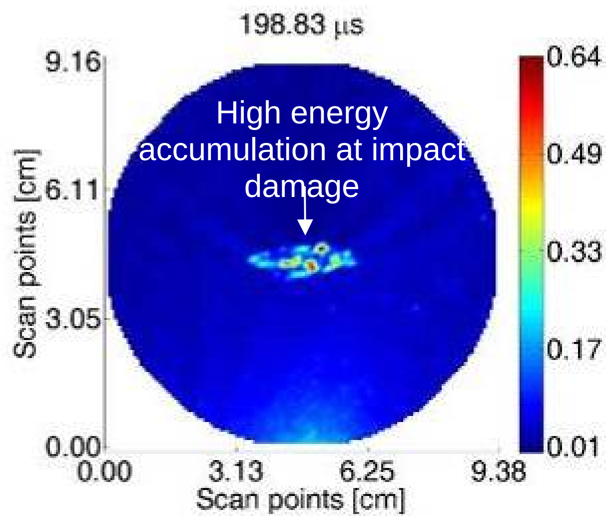

Figure 5.7 Contour plot of the cumulative kinetic energy field for the specimen shown in **Figure 5.5**.

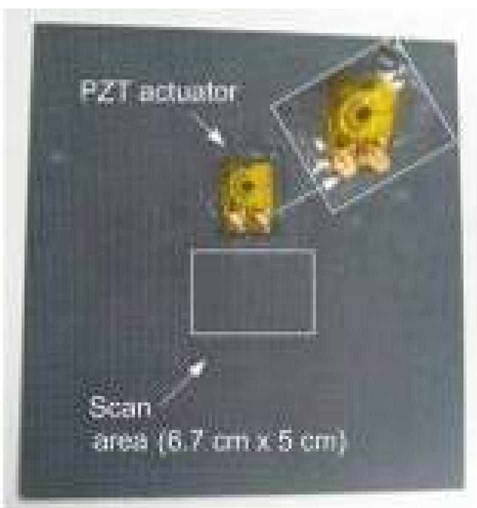

Figure 5.8 1.8 mm thick composite plate instrumented with a Kapton coated PZT.

The connectors obstruct the propagation of ultrasonic waves and allow a relatively high intensity beam to pass through the ‘gate’ formed between them (**Figure 5.9** and **Figure 5.10**).

Figure 5.11 shows a 2mm thick composite specimen with stiffeners. A significant amount of ultrasonic energy flow into the stiffener thereby reducing the intensity of the ultrasonic waves in the region beyond the stiffener (**Figure 5.12-Figure 5.14**). A curious observation in **Figure 5.13** is that the amplitude of the out-of-plane velocity is relatively high at the stiffener location than in the neighboring area on the actuator side. This can be explained by the following hypothesis. At the stiffener location, the faster traveling symmetric mode with low amplitude of out-of-plane velocity is mode-converted into the anti-symmetric mode with high out-of-plane velocity (Rose 1999). The slower traveling anti-symmetric mode emanating from the actuator has not yet arrived at the neighboring region. Therefore the stiffener location looks brighter in the image relative to its neighboring area.

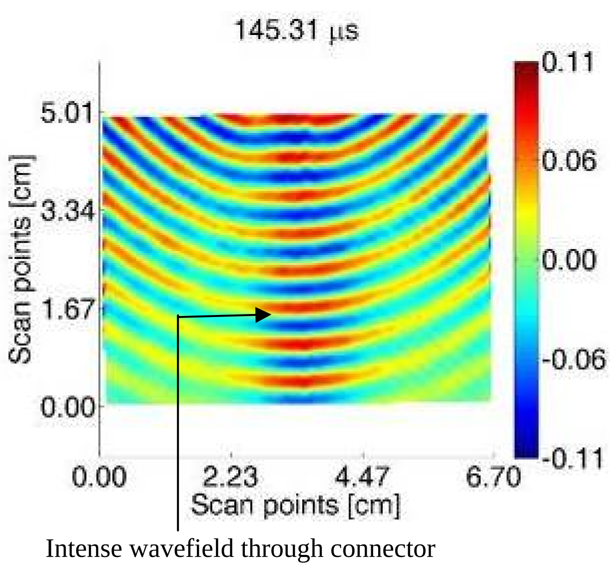

Figure 5.9 Contour plot of the out-of-plane ultrasonic velocity field for the specimen shown in **Figure 5.8**.

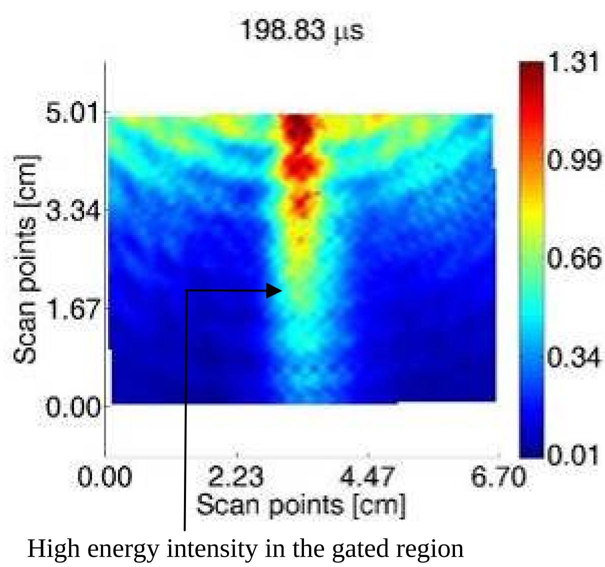

Figure 5.10 Contour plot of the cumulative kinetic energy field for the specimen shown in **Figure 5.8**.

Figure 5.11 2 mm thick composite plate with stiffeners and instrumented with circular PZTs.

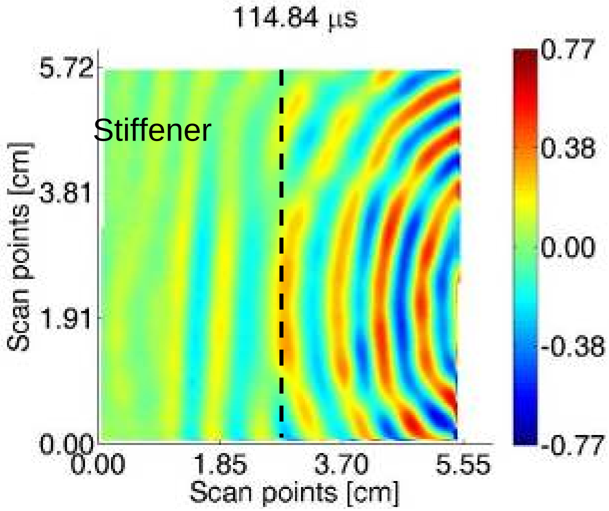

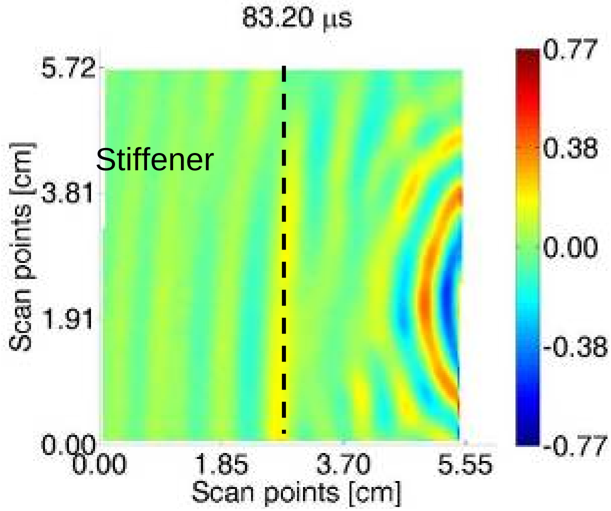

Figure 5.12 Contour plot of the out-of-plane ultrasonic velocity field for the specimen shown in **Figure 5.11**.

Figure 5.13 Contour plot of the out-of-plane ultrasonic velocity field for the specimen shown in **Figure 5.11** at a previous time instant.

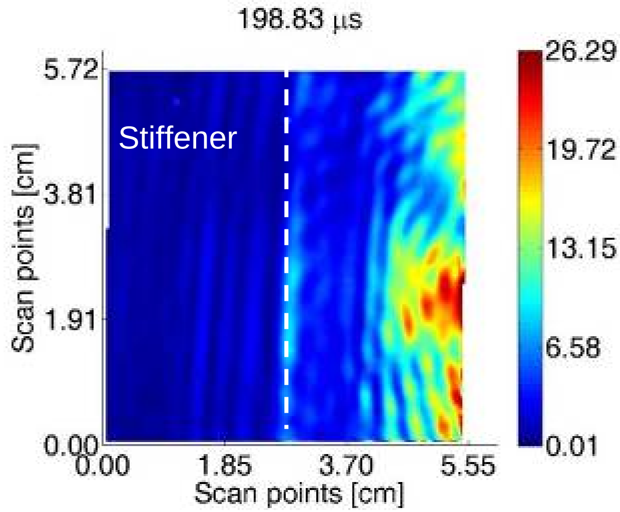

Figure 5.14 Contour plot of the cumulative kinetic energy field for the specimen shown in **Figure 5.11**.

Figure 5.15 shows an aluminum plate with variable thickness. The necking region is 1 cm wide. The plate is instrumented with two PZTs, one on either side of the neck. As can be seen from **Figure 5.16**, the intensity of the ultrasonic wave is higher in the thinner area of the plate. This can be intuitively explained by the fact that the same amount of ultrasonic energy can cause more vigorous oscillation in a thinner plate than in a thicker one. When ultrasonic waves are generated by the PZT on the thinner side, the thicker side exhibits little oscillation (**Figure 5.16** and **Figure 5.17**). Even when the waves are generated by the thicker side, the thinner side shows more vigorous oscillation (**Figure 5.18** and **Figure 5.19**).

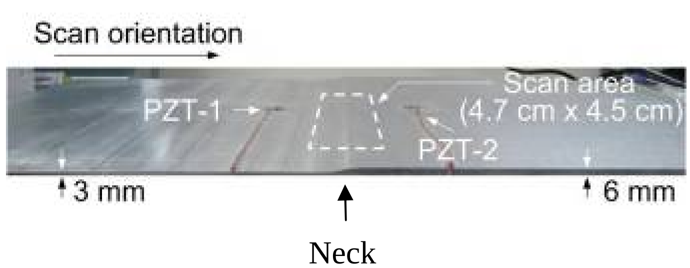

Figure 5.15 Aluminum plate with variable thickness and instrumented with square PZTs.

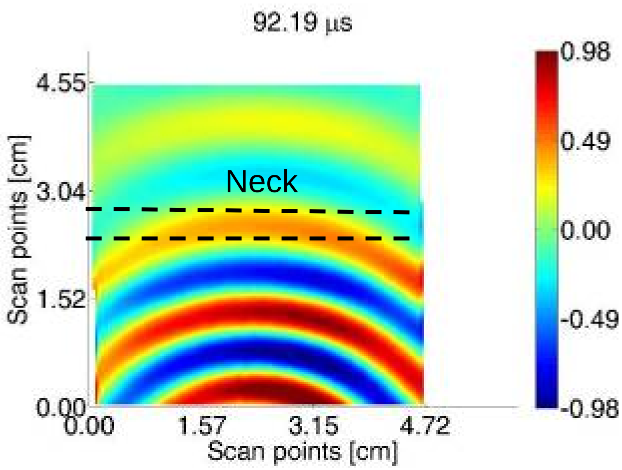

Figure 5.16 Contour plot of the out-of-plane ultrasonic velocity field excited by PZT-1 for the specimen shown in **Figure 5.15**.

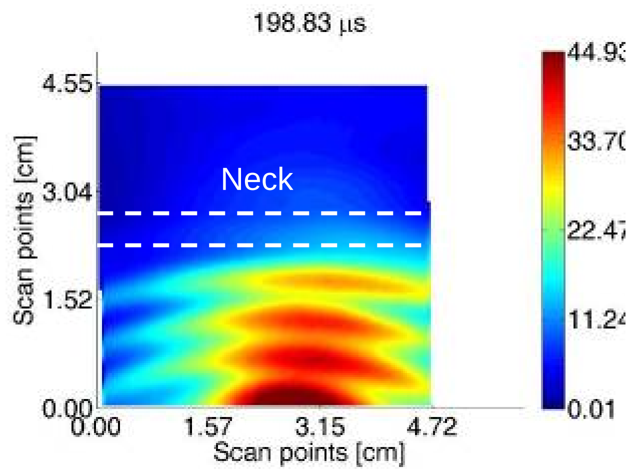

Figure 5.17 Contour plot of the cumulative kinetic energy field excited by PZT-1 for the specimen shown in **Figure 5.15**.

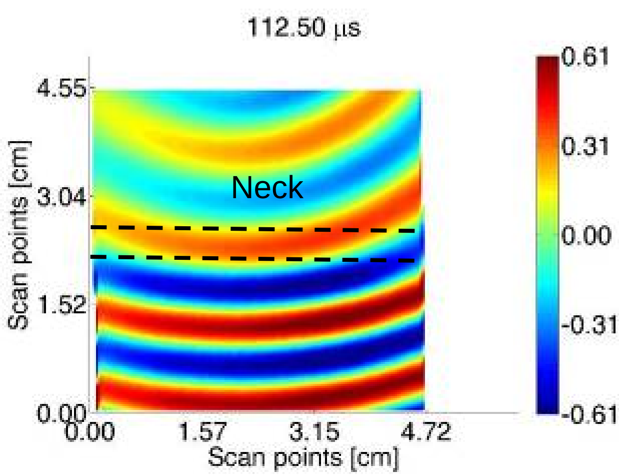

Figure 5.18 Contour plot of the out-of-plane ultrasonic velocity field excited by PZT-2 for the specimen shown in **Figure 5.15**.

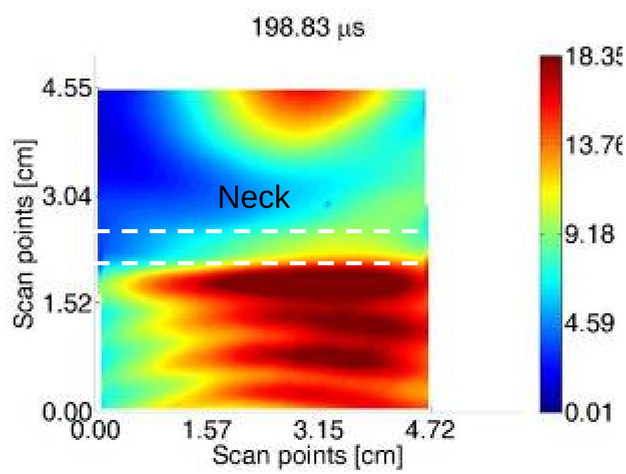

Figure 5.19 Contour plot of the cumulative kinetic energy field excited by PZT-2 for the specimen shown in **Figure 5.15**.

Our final specimen of interest is a steel structure with a bolted joint (**Figure 5.20**). The objectives of studying this specimen are threefold: to see the effect of wave interaction i) with a bolt, ii) with an overlap, and iii) with a lap joint, in that order. The effect of loosening the bolt was also studied.

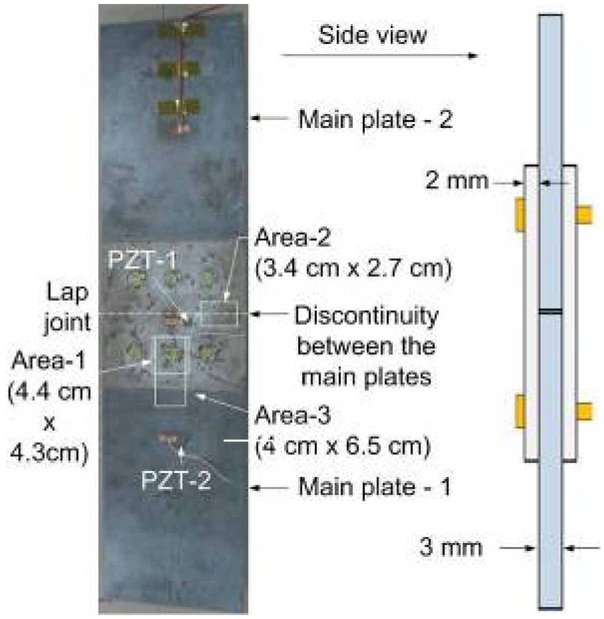

Figure 5.20 3 mm thick steel plate with 2 mm thick overlap plates and instrumented with square PZTs.

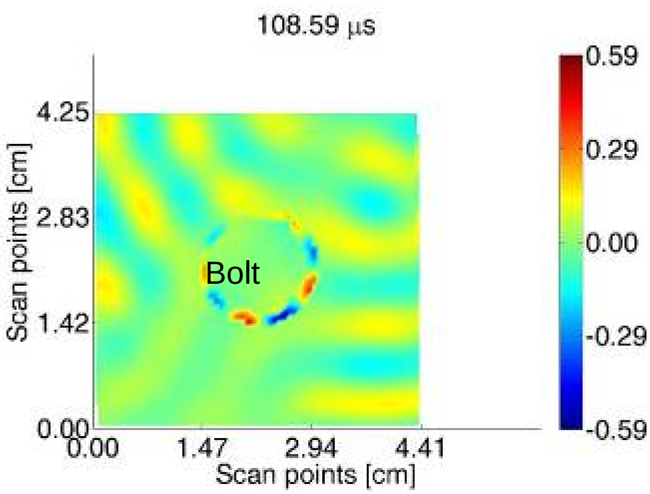

Figure 5.21 Contour plot of the out-of-plane ultrasonic velocity field (area-1) for the specimen shown in **Figure 5.20**. PZT-1 was used to excite the ultrasonic waves.

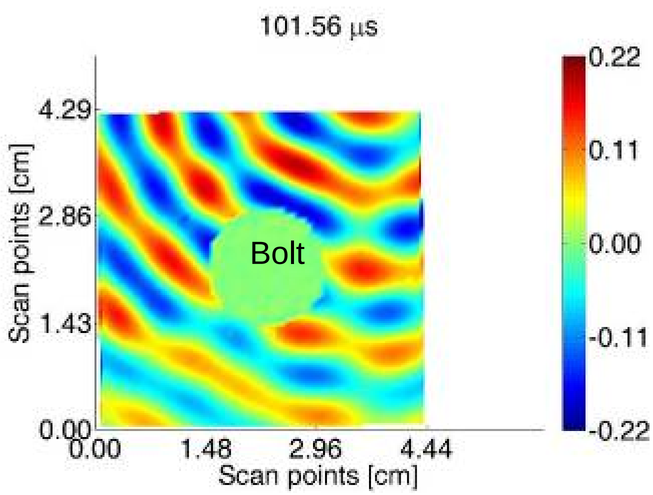

Figure 5.22 Contour plot of the out-of-plane ultrasonic velocity field (area-1) for the specimen shown in **Figure 5.20** with the bolt (contained in area-1) loosened. PZT-1 was used to excite the ultrasonic waves.

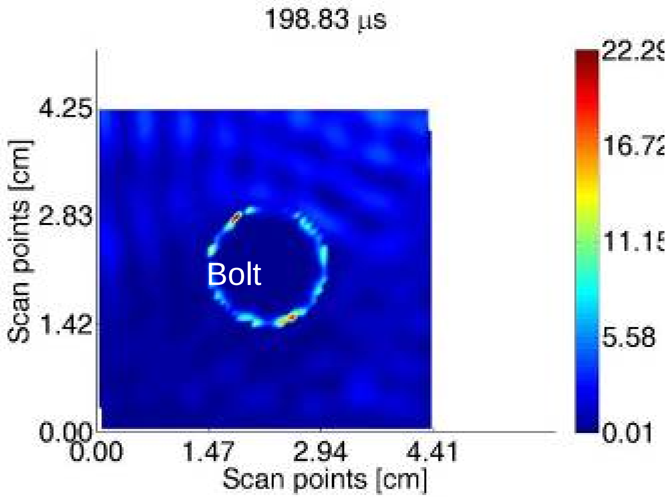

Figure 5.23 Contour plot of the cumulative kinetic energy field (area-1) for the specimen shown in **Figure 5.20**. PZT-1 was used to excite the ultrasonic waves.

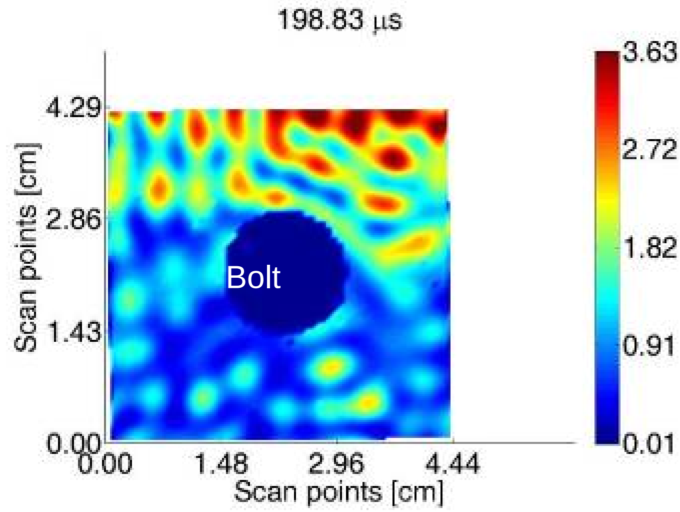

Figure 5.24 Contour plot of the cumulative kinetic energy field (area-1) for the specimen shown in **Figure 5.20** with the bolt (contained in area-1) loosened. PZT-1 was used to excite the ultrasonic waves.

Figure 5.21 and **Figure 5.22** show the out of plane velocity fields with the tightened and loosened bolt respectively when PZT-1 was used to generate the ultrasonic waves and Area-1 was scanned. Considerable ultrasonic activity can be seen around the tight bolt (**Figure 5.21** and **Figure 5.23**) as opposed to nothing around the loosened bolt (**Figure 5.22** and **Figure 5.24**). When the bolt is tight, ultrasonic waves leak into the thin washer which is strongly pressed against the steel plate. In the context of **Figure 5.21** - **Figure 5.24**, note that the washer is circular while the bolt is octagonal. Once the bolt is loosened, the waves cannot leak into the loosely fitted washer and the bolt plus washer region appears like a hole or a dark spot in the ultrasonic field image.

Next, PZT-2 was excited and Area-3 was scanned. High gradient in ultrasonic energy across the overlap boundary can be observed from **Figure 5.25**. It can therefore be concluded that not much energy leaks into the adjacent overlying plate.

To study the effect of the lap joint, PZT-1 was excited and Area-2 was scanned. The discontinuity in the underlying plates can hardly be observed from **Figure 5.26**. This observation is consistent with the previous one that adjacent plates do not significantly affect the wave propagation through a plate.

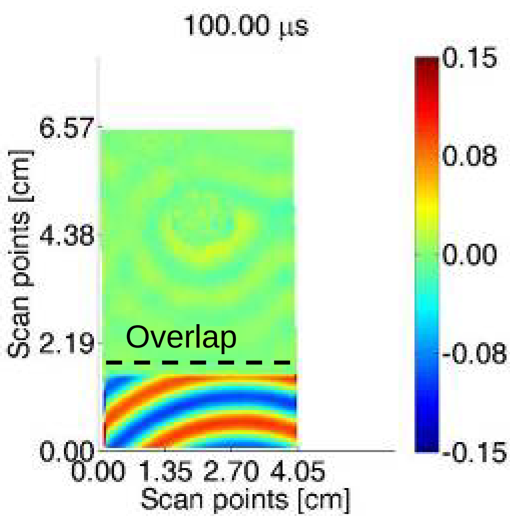

Figure 5.25 Contour plot of the out-of-plane ultrasonic velocity field (area-3) for the specimen shown in **Figure 5.20**. PZT-2 was used to excite the ultrasonic waves.

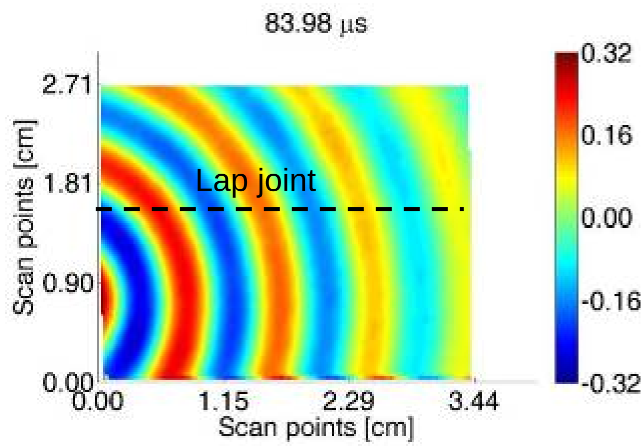

Figure 5.26 Contour plot of the out-of-plane ultrasonic velocity field (area-2) for the specimen shown in **Figure 5.20**. PZT-1 was used to excite the ultrasonic waves.

5.6 Chapter summary

This chapter described a study of ultrasonic wave propagation through complex engineering structures. It was observed that the location of structural components (like stiffeners, bolts, overlaps and necking regions) could be identified from the ultrasonic field images. The defect locations (like notch and impact damage) could also be identified from the high ultrasonic activity zones in the captured images. Overall, the study gives insight into the interaction of ultrasonic waves with different structural components as well as defects. This information may be used for improved damage detection in complex structures. Further studies include a more extensive research on such interaction phenomena with a broader selection of specimens. Also a detailed theoretical explanation for the observed wave interactions would be appropriate.

6. Damage detection from wavefield images: II. Delamination and disbond detection

6.1 Motivation

In the previous chapter, images of wave propagation in different specimens were presented. The motivation of the present chapter is to detect two particular types of defect (viz. delamination and disbond) from the scan images.

6.2 Chapter abstract

This study explores the feasibility of using a non-contact guided wave imaging system to detect hidden delamination and disbond in multi-layer composites. Lamb waves are excited by a Lead Zirconate Titanate (PZT) transducer mounted on the surface of a composite plate using an arbitrary waveform generator, and the out-of-plane velocity field is measured using a 1D scanning laser vibrometer. From the scanned time signals, wavefield images are constructed and processed to study the interaction of Lamb waves with hidden delamination and disbond. The chapter presents additional signal and image processing techniques used to highlight the defect in the scanned area. The performance of the proposed scheme is investigated using experimental data collected from a 1.8 mm thick multi-layer composite plate and another 2 mm thick composite wing fitted with spars.

6.3 Chapter introduction

In this chapter, we excite a fixed point on a composite specimen using a piezoelectric wafer transducer and scan the guided wave response using a laser vibrometer. Lamb waves are excited by a Lead Zirconate Titanate (PZT) wafer transducer using an arbitrary waveform generator (AWG).

Previous research on structural damage detection using laser vibrometry includes fatigue crack detection from the variation of ultrasonic amplitude profile [71],[75] and using frequency-wavenumber domain filtering to locate reflectors in the ultrasonic medium, some of which could be defects [18]. Another technique is to use a pulsed laser source to generate guided waves at arbitrary locations, then corresponding responses are measured at a single point using a conventional ultrasonic transducer; the wavefield images are then constructed using the principle of dynamic reciprocity [76-78].

The uniqueness of the present chapter is twofold. First, we observe and explain a hitherto unheeded phenomenon of standing wave formation when ultrasonic waves interact with delamination. Second, we propose novel signal and image processing techniques to highlight the interactions of ultrasonic waves with delamination and disbond. We also propose a way to distinguish between delamination and disbond.

This chapter is organized as follows. Section 6.4 describes a delamination detection technique in a multi-layer composite plate while Section 6.5 deals with disbond detection in a composite wing with multiple spars. The chapter then concludes with a brief summary.

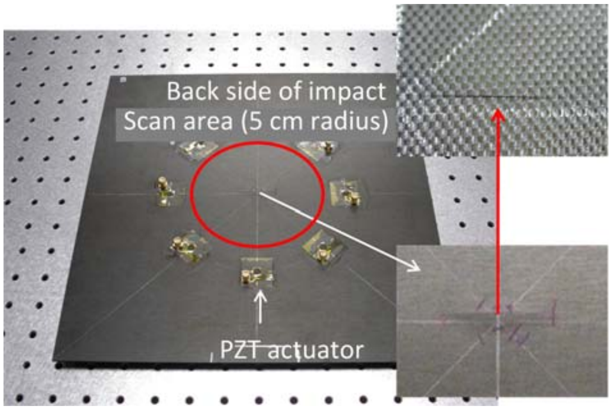

Figure 6.1 A multi-layer composite plate with impact-induced delamination

6.4 Delamination detection in a multilayer composite plate

In this section we present experimentally obtained wavefield images from a delaminated composite plate using a scanning laser vibrometer. We describe how standing waves are formed when ultrasonic waves interact with delamination, and propose signal and image processing technique to highlight such interactions.

The composite plate tested in this study is shown in **Figure 6.1** This 27.5 cm × 27.5 cm square plate of thickness of 1.8 mm was fabricated from IM7 graphite fibers with 977-3 resin material, and consists of 14 plies with a layup of [02/±45/0/±45]s. The test article was subjected to impact, and the formation of internal delamination near the center of the plate was confirmed from nondestructive thermographic imaging as shown in **Figure 6.2**. A 3 cm long impact damage could be seen on the back side of the impact (**Figure 6.1)**, but on the impact side of the specimen there was only a small dent which was barely visible to the naked eye.

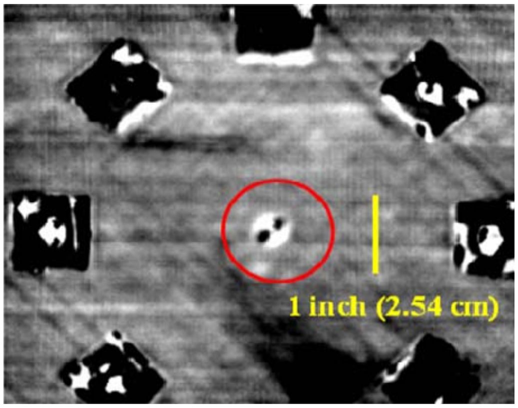

(a) Impact Surface

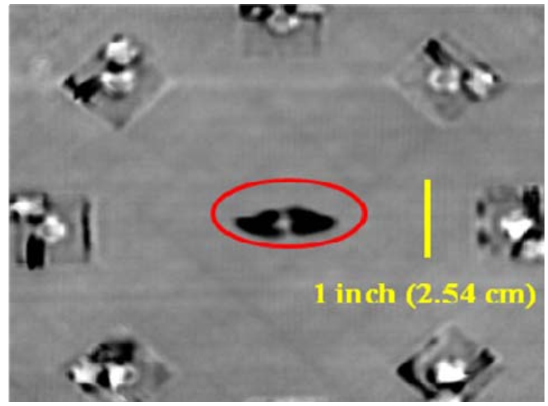

(b) Back surface

Figure 6.2 Nondestructive thermographic imaging of the composite plate

Figure 6.3 shows the overall configuration of the experimental setup. A 5A type piezoelectric wafer transducer (PZT) powered by an AWG and a signal amplifier was used to generate guided waves in the test article. The guided wave responses at several points within a specified area were sensed by a scanning laser vibrometer, and the data was collected by a built-in data acquisition system. The data was then exported to the MATLAB® software program and processed on a personal computer.

A 5.5 cycle tone burst signal at 100 kHz was used as the input waveform. The output voltage from the AWG was ±10 V and was amplified up to ±50 V using a power amplifier before being applied to the actuator PZT. One out of the eight PZT transducers installed on the backside of the impact was designated as the actuator (**Figure 6.1**).

The guided waves generated by the PZT transducer were measured by a *Polytec PSV-400-M4* scanning laser Doppler vibrometer. The 1D vibrometer used in this study measures the out-of-plane velocity of a target point using the principle of Doppler frequency-shift effect on light waves [79]. The scanning over a specified grid of points is done by steering the laser beam to the desired location using deflection mirrors which are built into the laser head. The laser vibrometer was placed about 0.9 m away from the test article, and the sensitivity of the velocity measurement was set to 10 mm/s/V. The time response at each measurement point was averaged 20 times to improve the signal-to-noise ratio, and a 75-125 kHz band pass filter was applied to eliminate exogenous noise outside the driving frequency band. A sampling rate of 2.56 MHz was used and the spatial grid density was set to 9 points per cm. We observed that, at the excitation frequency used in this study (100 kHz), the out-of-plane component of the velocity field is stronger for the antisymmetric mode compared to the symmetric one, and hence the 1D laser vibrometer is more sensitive to the antisymmetric mode. The wavelength corresponding to the first antisymmetric Lamb mode was found to be about 1.2 cm. It took about 40 minutes to scan a circular area with 5 cm radius containing about 6400 scan points (**Figure 6.1**).

Once the data are collected, it is converted to a universal file format and exported to the MATLAB® software program. The raw data contains time signals from each of the scanned points. Using MATLAB® graphic tools, a wave propagation video is created where each frame in the video represents the out-of-plane velocity field across the scanned surface of the target specimen at a particular instant in time. The snapshots at three representative time instants are shown in **Figure 6.4**. All images are plotted in RGB scale where low to high values are mapped from blue to red with green indicating middle range values. In **Figure 6.4**a, the incident waves can be clearly seen, and the interaction with the delaminated area is apparent in **Figure 6.4**b. Ultrasonic oscillations at the delamination location can be observed long after the incident waves had passed the delaminated area (**Figure 6.4**c). A possible explanation for this phenomenon is given in the following paragraph.

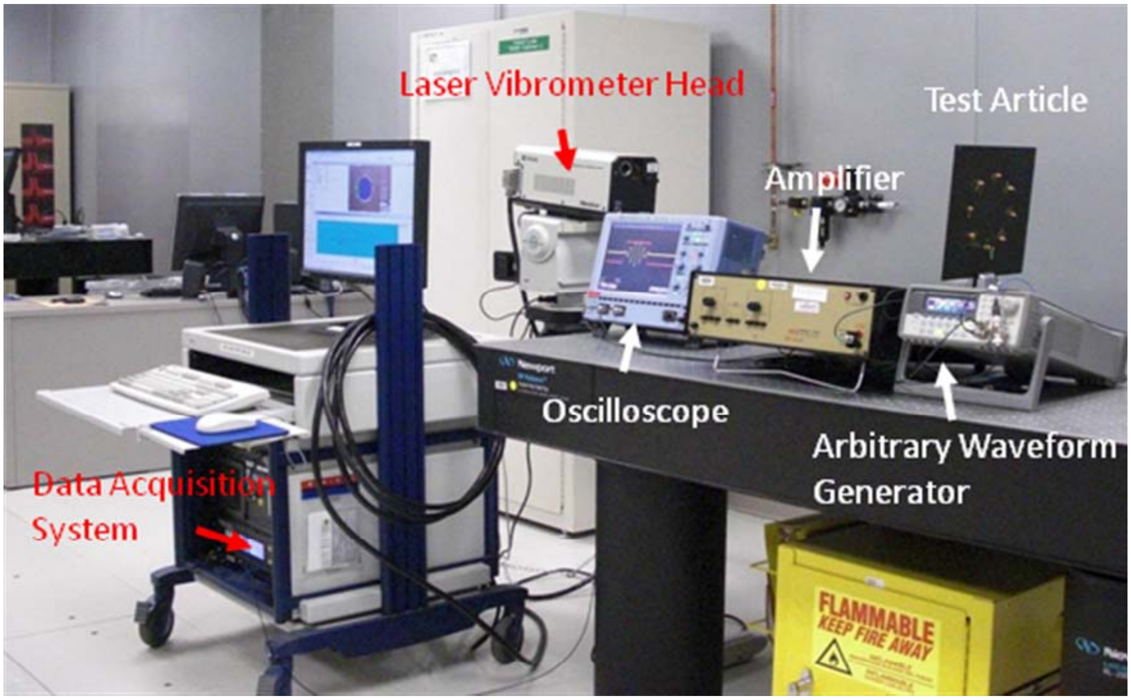

Figure 6.3 Overall configuration for laser based guided wave excitation and sensing experiment

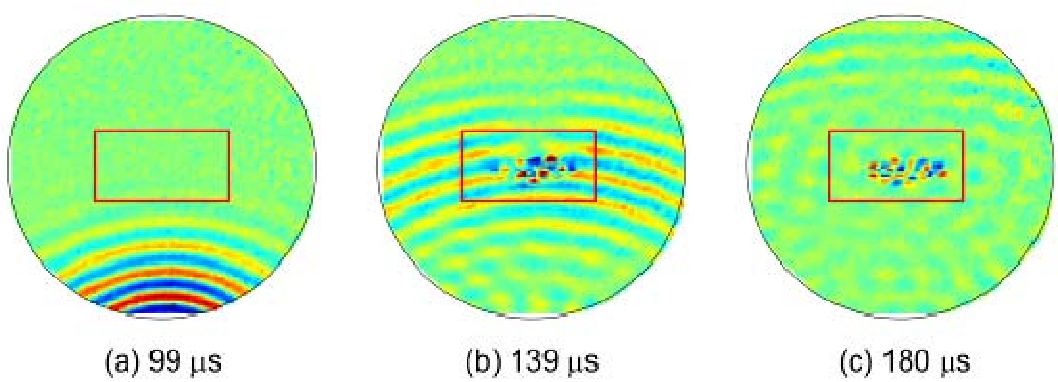

Figure 6.4 Laser vibrometer imaging of Lamb wave propagation in a 1.8 mm thick graphite plate containing delamination. Standing waves are observed at the delamination site.

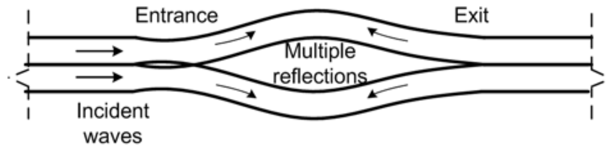

Figure 6.5 Schematic through-the-thickness side view of a delamination showing multiple reflections inside the delamination zone

Figure 6.5 shows a schematic through-the-thickness side view of a delamination. The incident waves enter the delamination site, and split and propagate independently through the laminates. A significant portion of these waves is reflected back from the exit. The reflected waves travel through the laminates and undergo reflection again at the original entrance. Numerical simulations using the strip element method have confirmed such multiple reflections taking place inside the delaminated zone [80],[81]. As a consequence of multiple reflections at the entrance and the exit, a considerable amount of ultrasonic energy is trapped inside the individual laminates. Now, the ultrasonic waves reflected from opposite ends of the delamination travel in opposite directions and interfere to produce standing waves according to the following equation:

$$\begin{aligned} &A\cos(\omega t - kx) + B\cos(\omega t + kx + \phi) \\ &= \underbrace{2B\cos(k\bar{x})\cos(\omega t + \frac{\phi}{2})}_{\text{Standing wave}} + (A - B)\cos(\omega t - k\bar{x} + \frac{\phi}{2}) \end{aligned} \tag{6.1}$$

In Equation (6.1), A and B are the amplitudes of the waves propagating in opposite directions (B < A without loss of generality); ω and k are the frequency and wavenumber of the propagating waves; ϕ is an arbitrary phase; t and x represent time and space coordinates respectively; $\bar{x}$ is the zero-shifted coordinate given by $\bar{x} = x + \frac{\phi}{2k}$. The first term in the right-hand side of the equation represents the standing waves at delamination while the second one represents the part of the wave that propagates. The standing waves remain trapped inside the delamination site long after the incident waves have passed. With time, however, the standing waves subside as the ultrasonic energy leaks out through the boundaries of the delamination and attenuates. Equation (6.1) describes the propagation and interference of pure longitudinal waves or pure shear waves. Although the equations describing Lamb waves would be more complex, Equation (6.1) captures the essence of standing wave formation.

Next, we propose a “standing wave filter” which is essentially a signal processing technique to isolate only the standing waves from a given wavefield. The first step is to convert the velocity field (v) from space-time domain (x,y,t) to wavenumber-frequency domain (k_x,k_y,ω) using a three-dimensional Fourier transform (3D FT)[18]:

$$V(k_x,k_y,\omega)=\int_{-\infty}^{\infty}\int_{-\infty}^{\infty}\int_{-\infty}^{\infty}v(x,y,t)e^{-i(k_x x+k_y y+\omega t)}dxdydt \tag{6.2}$$

Here, $V(k_x,k_y,\cdot)$ corresponds to the wavefront traveling in the vector direction $-k_x\hat{x}-k_y\hat{y}$, where $\hat{x}$ and $\hat{y}$ are the unit vectors along the x and y axes, respectively. A standing wave can be envisioned as a superposition of two waves of equal amplitude propagating in opposite directions over the same spatial region at the same time instant. Therefore, standing waves can be obtained from $V(k_x,k_y,\cdot)$ as following:

$$\begin{aligned}V_{sw}(k_x,k_y,\omega)&=V_{sw}(-k_x,-k_y,\omega)\\&=\min[|V(k_x,k_y,\omega)|,|V(-k_x,-k_y,\omega)|]\quad\forall\omega\end{aligned} \tag{6.3}$$

where the suffix sw stands for standing waves. The processing steps described in this section are all implemented in MATLAB in discrete-time paradigm. The range of ω in Equation (6.3) is below the Nyquist frequency. The portion of V_{sw} above the Nyquist frequency is modified to force the conjugate symmetry condition. Upon filtering, the residual signal can be transformed back to space-time domain using an inverse 3D FT:

$$v_{sw}(x,y,t) = \frac{1}{2\pi}\int_{-\infty}^{\infty}\int_{-\infty}^{\infty}\int_{-\infty}^{\infty} V_{sw}(k_x,k_y,\omega)e^{i(k_x x+k_y y+\omega t)}dk_x dk_y d\omega \tag{6.4}$$

This filtered wavefield $v_{sw}(x,y,t)$ simply contains any standing wave that is present in the originally scanned wavefield. For example, if the process described above is applied to the wavefield in Equation (6.1), the resulting field will only contain the standing wave component: $2B\cos(k\bar{x})\cos(\omega t+\frac{\phi}{2})$. **Figure 6.6** shows the resulting field when the originally measured wavefield images in **Figure 6.4** are passed through the standing wave filter. In **Figure 6.6**b, standing waves can be observed at the delamination location. Although mitigated, standing waves are found to be present long after the incident waves have passed (**Figure 6.6**c). Notice that the incident waves are filtered out in **Figure 6.6**. To image the total amount of standing wave energy experienced at a certain location, a mass-normalized value of the cumulative kinetic energy (E_{sw}) is computed as follows:

$$E_{sw}(x,y,t) = \int_{\tau=0}^{t} \frac{1}{2} v_{sw}^2(x,y,\tau)d\tau \tag{6.5}$$

The cumulative energy field when plotted at the end of the scanning duration (180 μs) helps locate and visualize the delamination (**Figure 6.7**).

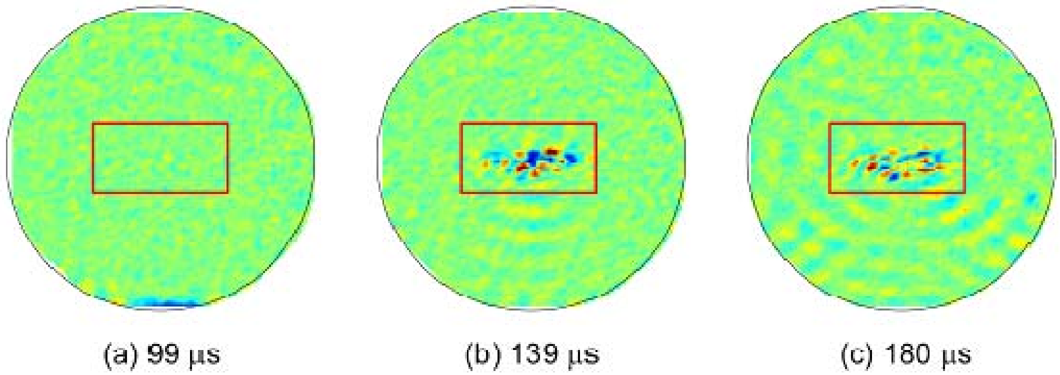

Figure 6.6 Isolating the standing wave components from the velocity fields in **Figure 6.4**

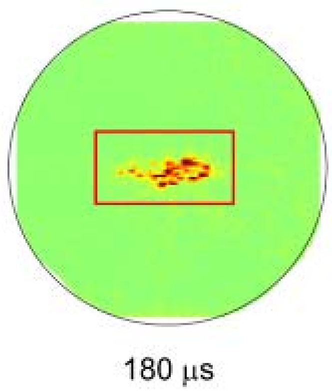

Figure 6.7 Accumulated mass-normalized kinetic energy corresponding to the standing wavefields in **Figure 6.6**

Another way to highlight the interaction of ultrasonic waves with delamination is by simply considering the total amount of ultrasonic energy that has passed through a certain point. As standing waves are formed, ultrasonic energy remains trapped inside the delamination region for a longer time as opposed to other locations where the incident or reflected waves are only ephemerally present. Therefore, by computing the accumulated mass-normalized kinetic energy (E_c):

$$E_c(x,y,t) = \int_{\tau=0}^{t} \frac{1}{2} v^2(x,y,\tau) d\tau \tag{6.6}$$

it is possible to accentuate the delamination location in the entire scanned area (**Figure 6.8**). The visual indication of the delamination can be enhanced even further by image processing. A well-known blob detection algorithm called Laplacian image filtering [82] is applied to the image in **Figure 6.8**c to produce **Figure 6.9**. The Laplacian mask (**L**) used in the filter is given by:

$$\mathbf{L} = \begin{bmatrix} -1 & -1 & -1 \\ -1 & 8 & -1 \\ -1 & -1 & -1 \end{bmatrix} \tag{6.7}$$

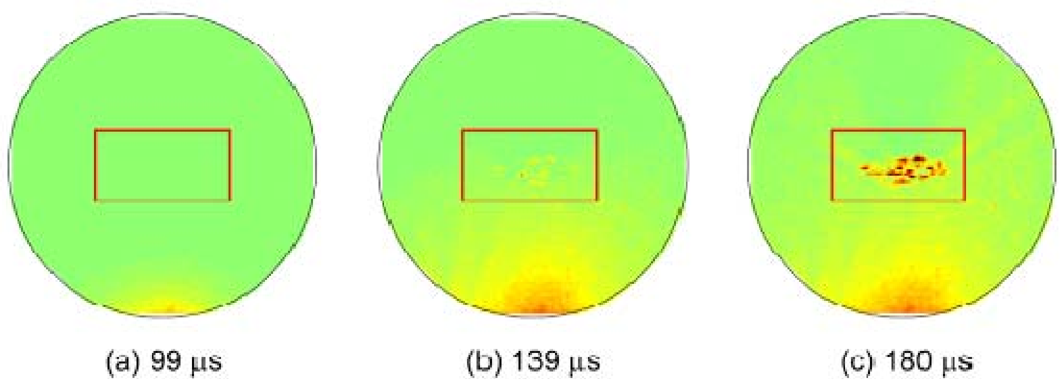

Figure 6.8 Accumulated mass-normalized kinetic energy corresponding to the velocity fields in **Figure 6.4**

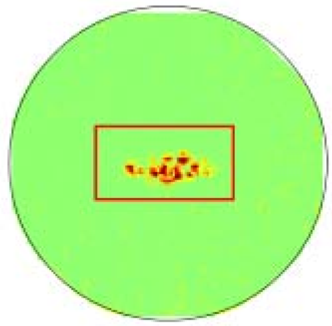

Figure 6.9 Effect of applying Laplacian image filter to the image in **Figure 6.8**c

The signal processing steps described above are all required to highlight the defect area with respect to the background. These steps might prove crucial while developing automated damage detection algorithms in the future.

The production of standing waves was also verified through numerical simulation using commercial finite element software.[83] A two dimensional plane strain model of a 3 mm thick graphite plate was excited using a piezoelectric wafer transducer. A 5-cycle tone-burst voltage signal centered at 100 kHz was used as input. This excited the fundamental antisymmetric Lamb wave mode in the laminate with a 0.8 cm wavelength along with other Lamb wave modes. The 3.5 cm wide delamination was modeled by elements with reduced density and stiffness, and enhanced damping coefficient.[84] The delaminated region is assumed to be one element thick. For the sake of consistency with experimental results, only the out-of-plane velocity field is reproduced in this article. **Figure 6.10** shows the snapshots of the out-of-plane velocity field at three different time instants. Standing wave at the delamination site (marked with a line) can be observed in addition to the transmitted and reflected waves.

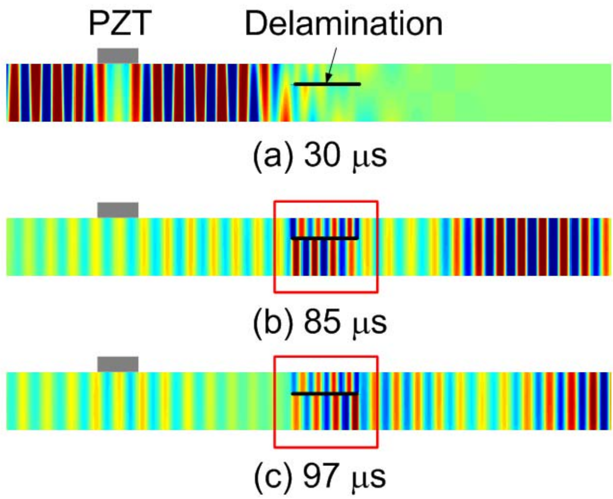

(b) 53 μs

Figure 6.10 Numerical simulation of Lamb wave propagation through a graphite plate containing delamination. Standing waves are observed at the delamination site.

6.5 Disbond detection in a composite wing with multiple spars

Here we present wavefield images from a composite wing specimen with a disbond between the wing surface and one of the spars. The Laplacian image filtering technique described in the previous section was found effective to highlight the damage.

The composite specimen tested for disbond is shown in **Figure 6.11**. This 11.8 cm × 15.7 cm plate of thickness of 2 mm is fitted with three spars and has a 40 mm × 60 mm area cut off from the top right corner. The details of the fabrication materials were not provided to the authors. A blade induced disbond was introduced between the wing surface and the base of one of the spars as shown in **Figure 6.11**.

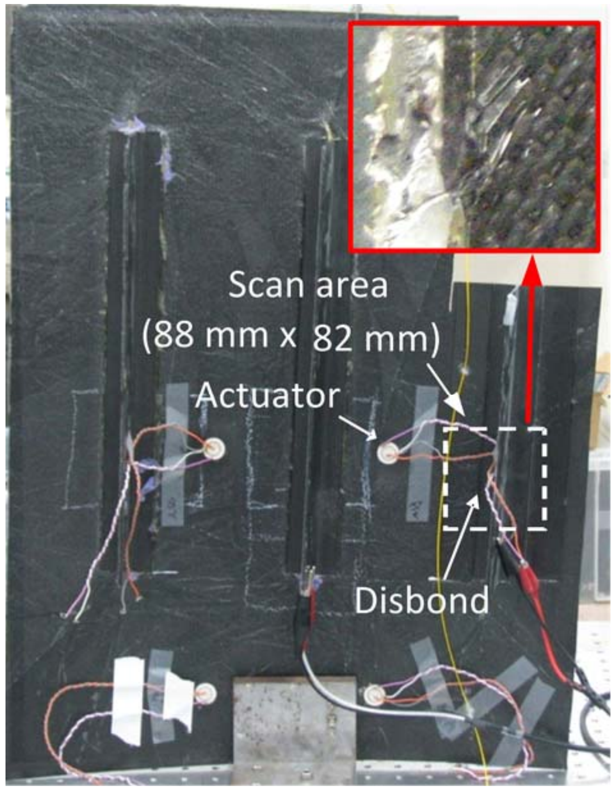

Figure 6.11 A composite wing fitted with spars. A blade induced disbond was introduced between the plate and one of the spars.

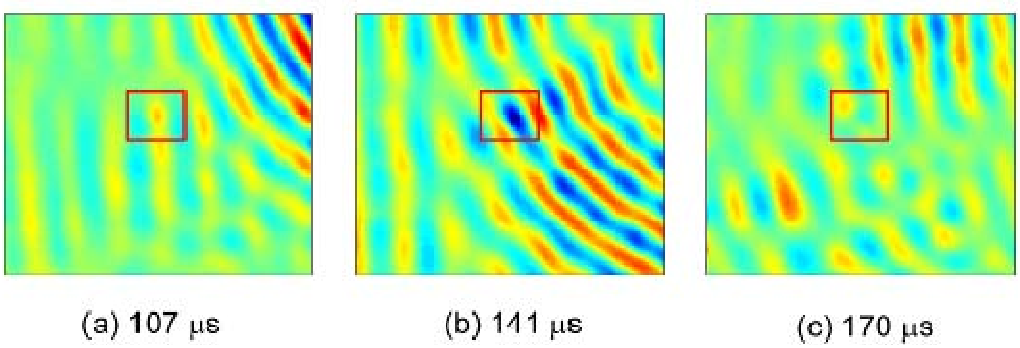

Figure 6.12 Snapshots of Lamb wave propagation on the wing surface

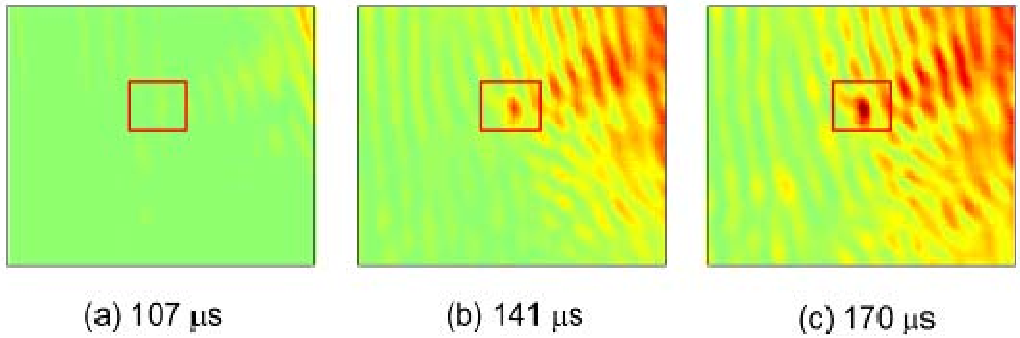

Figure 6.13 Accumulated mass-normalized kinetic energy corresponding to the wavefield in **Figure 6.12**

The input signal, data acquisition settings and vibrometer settings were identical as in the previous section. The scan was done on the external surface of the wing i.e. on the opposite side of what is shown in **Figure 6.11**. The scanned area is a 8.8 cm x 8.2 cm rectangle containing about 6000 scan points. The longest disbond dimension is 2 cm and the wavelength of the fundamental antisymmetric mode is about 1.5 cm. **Figure 6.12** shows snapshots of wave propagation in the structure at certain time instants. As can be observed from **Figure 6.12**b, the out-of-plane velocity of the ultrasonic wave is comparatively high at the disbond location. This is more evident from the accumulated kinetic energy images in **Figure 6.13**. Unlike delamination, a disbond is not bounded on all sides and a substantial part of the waves reflected from the edge of the disbond escapes through the open end of the disbond (**Figure 6.14**). Therefore, the standing waves which are formed in a delamination do not occur in the case of a disbond. Note that unlike **Figure 6.4**c, standing waves are not observed in the disbond area in **Figure 6.12**c. However, convergent waves reflected from a roughly semicircular disbond edge (as is the case here) stay inside the disbond region at least momentarily and interfere with the incident waves (**Figure 6.14**). This interference causes high amplitude oscillation inside the disbond region and provides explanation for the observations in **Figure 6.12** and **Figure 6.13**. Once again, the effectiveness of Laplacian image filter in highlighting the disbond location is demonstrated (**Figure 6.15**). As a note, the application of standing wave filter does not help in the case of disbond detection, which is expected.

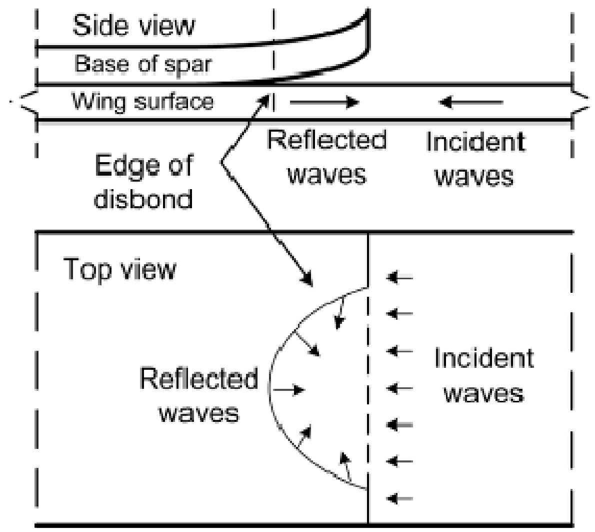

Figure 6.14 Schematic diagram showing the interaction of ultrasonic waves with disbond

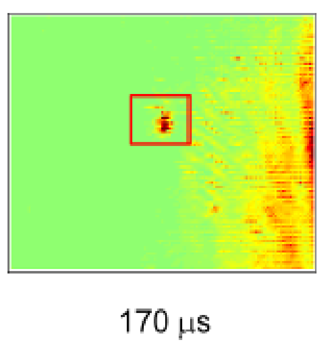

Figure 6.15 Application of Laplacian image filter to highlight the disbond location

In summary, it was observed that both delamination and disbond could be detected by the application of Laplacian image filter to the original wavefield images. However, only delamination could be detected using the standing wave filter proposed in this chapter. Therefore, by applying both the filtering techniques, one can differentiate between a delamination and a disbond.

6.6 Automated damage detection

The image processing techniques described in the previous sections make the defect region conspicuous in the background of the entire scan area. In this section, we describe a procedure to automatically detect the defect location from the processed scan images. This automatic detection algorithm not only needs to detect the damage but also has to correctly recognize undamaged objects.

The result from a representative undamaged composite plate specimen is shown in **Figure 6.18**. The original wave propagation image is processed using the Laplacian filtering technique described in section 6.4 and the filtered image is shown in **Figure 6.18**. It can be observed from **Figure 6.9**, **Figure 6.15** and **Figure 6.18** that high intensity values in the scan images of damaged specimens are clustered together in the defect region. On the other hand, the high intensity values in the undamaged specimen scan appear scattered across the scan area, especially near the outer boundary of the scan area. The latter can be explained by the working principle of a laser Doppler vibrometer. In case of one-dimensional laser vibrometers which measure the out-of-plane velocity component, the signal to noise ratio of the measured ultrasonic signals drops as the laser incidence angle increases [79]. In our experiments, the laser head was placed directly over the middle of the scan area, which resulted in slant incidence of the laser beam towards the edges.

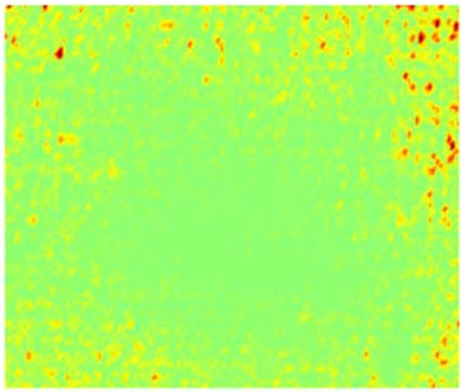

Figure 6.16 Scanned image from an undamaged composite plate after the application of Laplacian image filtering technique

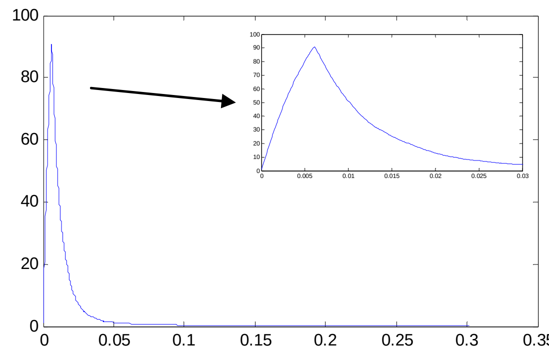

Figure 6.17 Distribution of the intensity values in the image shown in **Figure 6.16**

The automated damage detection algorithm is designed in two steps. In the first step, the high intensity values are identified using outlier detection. In the second step, a cluster analysis is performed to check if the outliers detected from the previous step are clustered or scattered. These two steps will be described in further detail in the following paragraphs. It is assumed that there is only one defect in the scanned area. Multiple clusters of outliers resulting from multiple damages will confuse the cluster detection algorithm.

The first step in the algorithm is to detect the high intensity outliers in the scan image. In this research, we use the three sigma outlier detection [85]. Consider a unimodal distribution with mean μ and standard deviation σ. The probability that a random variable will assume a value more discordant than $(\mu \pm 3\sigma)$ is less than 5% [85]:

$$\Pr(|X-\mu| \geq 3\sigma) \leq \frac{4}{9} \times \frac{\sigma^2}{(3\sigma)^2} = 0.049 \tag{6.8}$$

This probability is even lower when we just consider values over $(\mu + 3\sigma)$. Since the intensity distributions in the processed images are approximately unimodal (e.g. **Figure 6.17**) we used Equation (6.8) to detect the high intensity outliers.

The outliers detected in the processed scan images from the two damaged specimens (**Figure 6.9** and **Figure 6.15**) are shown in **Figure 6.18** andFigure **6.19**. **Figure 6.18** is the result obtained from the delaminated composite plate described in section 6.4 andFigure **6.19** is from the composite wing section with a blade induced disbond discussed in section 6.5. As expected, the outliers in the damaged specimens are clustered at the defect location.

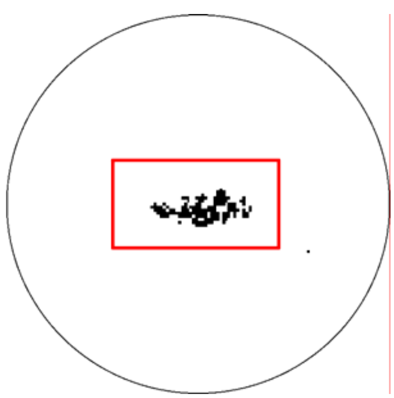

Figure 6.18 Outlier intensity values identified in the processed scan image (**Figure 6.9**) from the delaminated composite plate

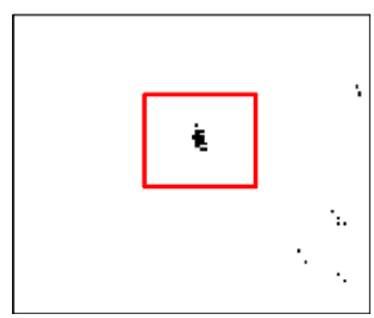

Figure 6.19 Outlier intensity values identified in the processed scan image (**Figure 6.15**) from the composite wing with blade induced disbond

Figure 6.20 (a) shows the outliers detected from the image in **Figure 6.18**. The experimental specimen being undamaged, we see the outliers scattered all over the outer perimeter of the scan area. However, after an impact induced delamination was introduced in the same specimen, the outliers in the processed scan image are found to be clustered at the delamination site (**Figure 6.20** (b)).

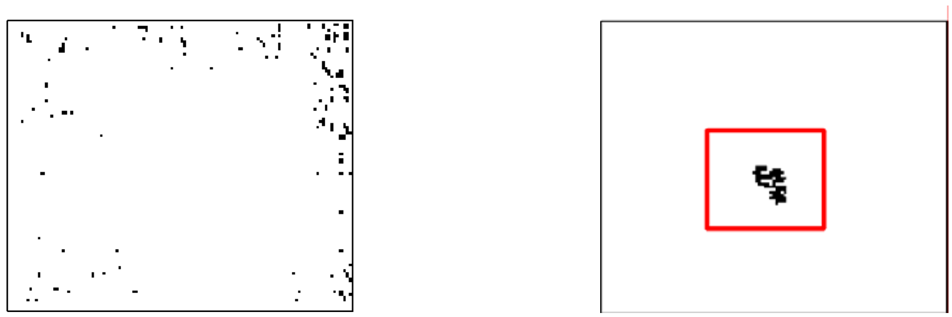

(a) Before introducing delamination (b) After introducing delamination

Figure 6.20 Outlier intensity values identified in the processed scan image from a composite plate

Once the outliers are identified, we use a cluster detection algorithm. The process is based on the complete spatial randomness (CSR) hypothesis which assumes that if there is no apparent cluster in a spatial distribution of points, then the points are randomly distributed in space with Poisson distribution [86]. The Poisson parameter, λ is given by:

$$\lambda = \frac{n}{A} \tag{6.9}$$

where n is the number of outliers and A is the scan area. Under this hypothesis, one can argue that the area enclosing r outliers $(A_r : 1 \leq r \leq n)$ is gamma distributed with parameters a and b given by $(a = r, b = \frac{1}{\lambda})$.

$$A_r \sim gamma(a = r, b = \frac{1}{\lambda}) \tag{6.10}$$

We thereby define the test statistic for cluster detection as following. At first, the coordinates of the centroid of the outlier points is evaluated. Then, the distance from the centroid to each outlier point is computed and arranged in ascending order. Let this distance be d_r for the r^{th} outlier point in the sorted distance array. Then, the probability (p_r) that the circle with radius d_r would contain r points is:

$$p_r = P[A_r = a_r \mid A_r \sim Gamma(a = r, b = \frac{1}{\lambda})]$$
$$\text{where } a_r = \pi d_r^2 \tag{6.11}$$

This probability p_r is evaluated repeatedly for each outlier point $1 \le r \le n$, and a P-value is computed as the average of these n probability values:

$$\text{P} - \text{value} = \frac{1}{n}\sum_{r=1}^{n} p_r \tag{6.12}$$

The P-value is the level of significance that the outlier points are scattered randomly and are not clustered in space. Therefore, in our application, a lower P-value would indicate damage.

Using the above procedure, the P-values for the three damaged specimens shown in **Figure 6.18**, Figure **6.19** and **Figure 6.20** (b) were found to be 0.04%, 10% and 0.01% respectively. The P-value for the undamaged specimen shown in **Figure 6.20** (a) is 65%. With a 15% or 20% threshold for level of significance, the damaged and the undamaged specimens are classified correctly. In the latter case, a few outliers are outside the defect area and are caused partly due to the low signal to noise ratio. These outliers away from the defect pull the centroid towards them and confuse the algorithm to some extent. Note that the cluster detection algorithm described above works under the wide-sense assumption that if there is a cluster we can find its centroid reasonably accurately.

The proposed automated damage detection technique was applied to two additional scenarios – i) an impact induced disbond on the composite wing, and ii) an undamaged area scan on the same composite wing. The processed scan images (using Laplacian image filtering technique) as well as the respective P-values are shown in **Figure 6.21** and **Figure 6.22**. The Laplacian image filtering technique did not work well on the undamaged area scan thereby producing clustered high intensity values in the processed image. The reason might be inferior quality and surface condition of the specimen, or the structural features in the vicinity of the scanned area. Further work must be done in order to address this issue of false alarm.

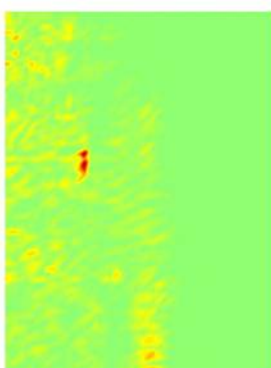

P-value = 5%

Figure 6.21 Processed scan image (using Laplacian filtering technique) from an impact induced disbond on the composite wing

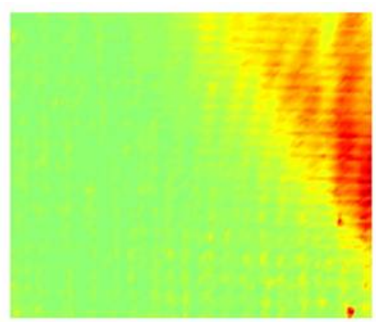

P-value = 0.3%

Figure 6.22 Processed scan image (using Laplacian filtering technique) from an undamaged area on the composite wing

6.7 Chapter summary

This chapter studied the applicability of non-contact wavefield imaging techniques to detect delamination and disbond in composite structures. A piezoelectric transducer was used to excite guided ultrasonic waves in the target structure and a laser vibrometer was used to image the resulting ultrasonic velocity field. The wavefield images thus obtained were further processed to highlight the defect location in the entire scan area. In particular, two novel processing techniques are proposed in this chapter: a standing wave filter and another Laplacian image filter. Both were found effective for detecting delamination while the latter was found useful to detect disbond. By applying both the processing techniques to a scanned image, one can differentiate between a delamination and a disbond. As a closing note of interest, the phenomenon described in this article is in some ways similar to the trapping of seismic waves in alluvial basins [87].

7. Conclusion

7.1 Summary of the work

This research explored various ultrasonic techniques to perform automated baseline free damage detection in structures. The major contributions of this research are i) providing mathematical models for the interaction of ultrasonic waves with various types of defects viz. notch, crack, delamination and disbond, and ii) developing signal processing techniques to extract the damage sensitive features from the raw ultrasonic signals.

Chapter 2 described a fully automated baseline-free technique for notch and crack detection in plates using piezoelectric wafer transducers. An over-determined system of Lamb wave measurements was used to obtain both the damage index and the damage threshold. The technique is limited in application to plate structures. However, the philosophy of making redundant measurements for the sake of error estimation may have broader applicability.

Chapters 3 and 4 concerned with nonlinear ultrasonic techniques for crack detection in metallic structures. Chapter 3 described a nonlinear guided wave based technique while a nonlinear system identification method was proposed in Chapter 4. In Chapter 3, a semi-analytical method was formulated to investigate the behavior of a bilinear crack model. Upon comparing the behavior with experimental observations, it was inferred that a bilinear model can only partially capture the signal characteristics arising from a fatigue crack. A correlation between the extents of nonlinear behavior of a breathing crack with the different stages of the fatigue crack growth was also made in Chapter 3. In Chapter 4, a popular electro-magnetic impedance circuit was used to detect acoustic nonlinearity produced by a crack. Although valuable insight on crack nonlinearity was obtained through these exercises, the goal of baseline-free damage detection by using nonlinear ultrasonics remained elusive due to the difficulty of segregating crack nonlinearity with the nonlinearity arising from the equipment and adhesive interfaces.

Chapters 5 and 6 comprised the final part of this research where wavefield images from a scanning laser vibrometer were digitally processed to detect hidden delamination in composite structures. Once processed, the defect in the scanned surface stands out as an outlier in the background of the undamaged area. An outlier analysis algorithm was then implemented to detect and localize the damage automatically. In Chapter 5, exploratory groundwork on wavefield imaging was done by obtaining wave propagation images from specimens made of different materials and with different geometries. In Chapter 6, delamination and disbond type defects in composite structures were automatically detected from the scan images through appropriate signal and image processing.

7.2 Limitations of the work

There are several issues which must be addressed before the work presented in this research can be adapted for field applications. First of all, the methods presented here must be validated on a wide range of structures of practical engineering interest. The specimens tested during this research represent only a small subset of those being used in the industry, and additional challenges are expected while implementing the techniques on more complex structures.

Another limitation of the work relates to the use of laser vibrometer. To image the ultrasonic wavefield, the laser vibrometer must be able to “see” the scan area. This poses a major problem for scanning interior and hard to access locations on a structure or a mechanical assembly. However, ultrasonic waves are often able to penetrate deep into a structure and carry information from its depth to the scannable surface. Also, one-dimensional laser vibrometers are not suitable for scanning surfaces with substantial curvature. In such cases, either three-dimensional laser vibrometers or scanning pulse laser sources must be used.

The ultrasonic energy trapping method described in this research needs to be tested in further complex structures, where the structural features itself might lead to a certain degree of trapping. A related study would be analyzing the sensitivity of the technique – i.e. how small a defect can be detected by ultrasonic waves of a given wavelength. It is expected that appropriate choice of ultrasonic wavelength will result in magnitudes of order higher energy trapping in the defect area compared to the trapping caused by structural features. The role of sensitivity analysis and application specific tuning in ultrasonic damage detection is well appreciated among non-destructive testing researchers [88] and it applies to the present research as well.

7.3 Future research direction in non-contact wavefield imaging

This research work is expected to contribute to the growing field of infrastructure monitoring, especially in detecting structural damages using non-contact optics-based methods. Development of a fully non-contact, laser based excitation and sensing system is underway. Preliminary results from such a system is described below.

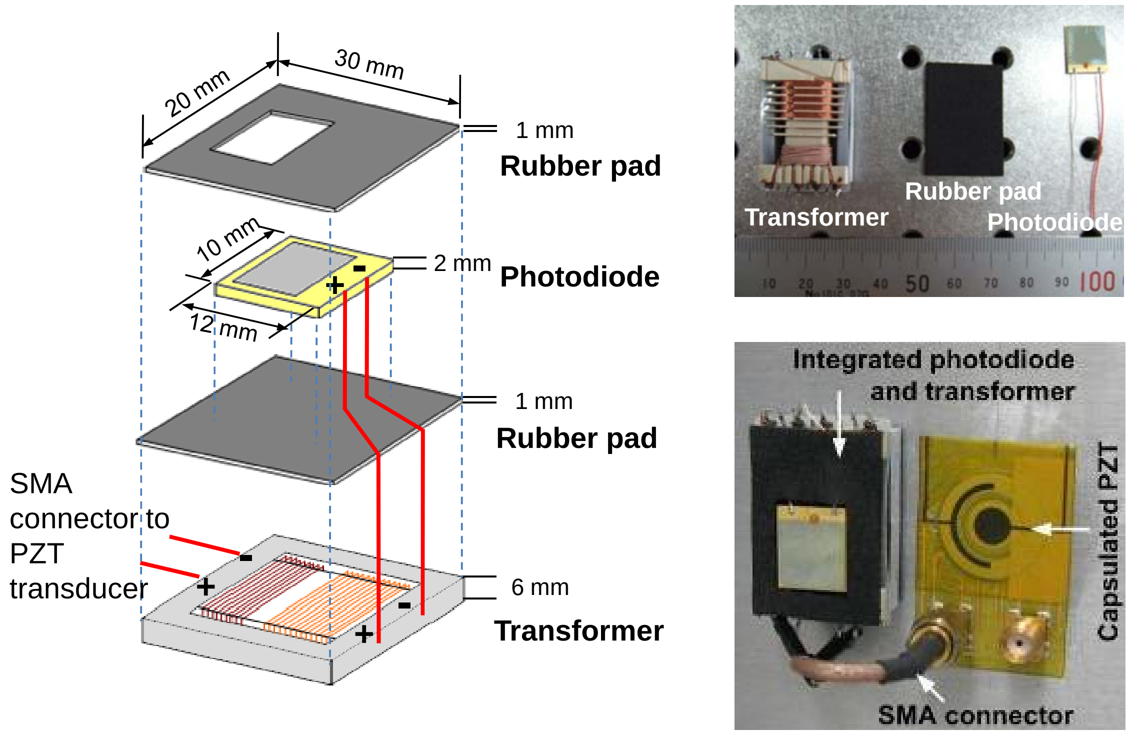

Figure 7.1 A PZT transducer node for wireless guided wave excitation

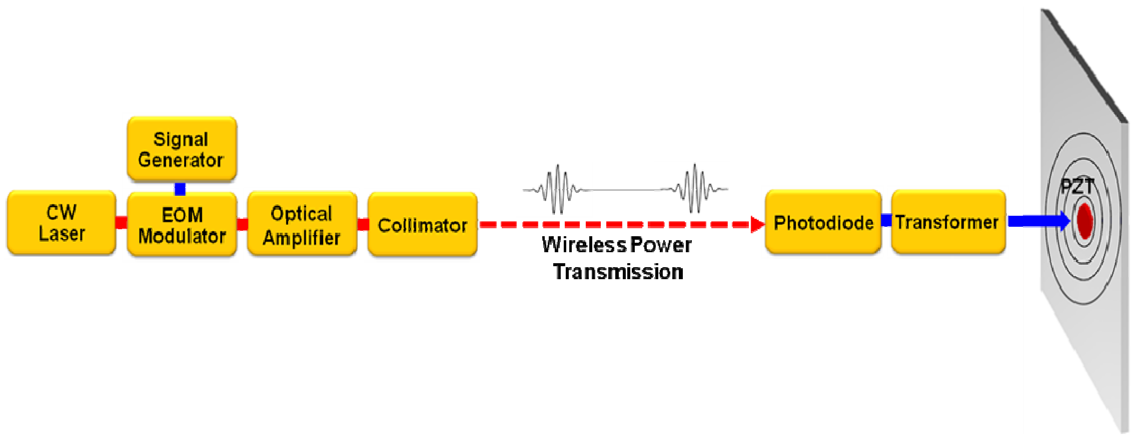

Figure 7.2 A schematic of wireless PZT transducer excitation using a laser source

Figure 7.1 shows the actuator node used in this study. It consists of a PZT wafer, a photodiode and a transformer padded with rubber sheets. The actuator is remotely excited using a laser light source (**Figure 7.2**). The source light is modulated by the electro-optic modulator (EOM) to produce user defined waveforms. In our experiments, a 5.5 cycle tone burst signal at 100 kHz driving frequency is used. The strength of the optical signal is then enhanced using an optical amplifier before it is focused on the photodiode. The photodiode converts the input optical power into electric voltage and this voltage is applied to the PZT transducer through a transformer. The PZT transducer when thus electrically excited generates ultrasonic waves in the structure. The excitation amplitude achieved in this study amounts to ±800 mV.

Figure 7.3 shows the experimental specimen. The 75 cm long composite channel has a 10 cm wide base and 6 cm high walls on either side. The specimen is 4 mm thick. Details of the material used to fabricate this structure were not provided to the authors. The sensing region was about 25 cm away from the actuator node. A reflective tape (3M Scotchlite™) was used to acquire clean signal from the laser vibrometer.

Before creating the ultrasonic wavefield image of the scanned area, a comparison between non-contact laser excitation and conventional wire excitation was made. A 5.5 cycle tone-burst signal centered at 100 kHz and ±800 mV peak amplitude was used in each case. The resulting out-of-plane velocities measured at PZT B in **Figure 7.3** using the laser vibrometer are shown in **Figure 7.4**. The two types of excitation have different processing times and produce slight difference in phase in the measured signals. The phase difference had been corrected in **Figure 7.4**.

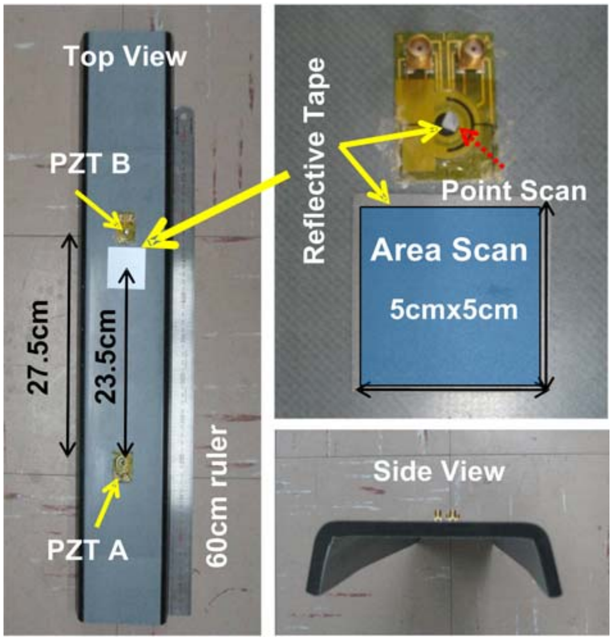

Figure 7.3 A composite channel used as experimental specimen

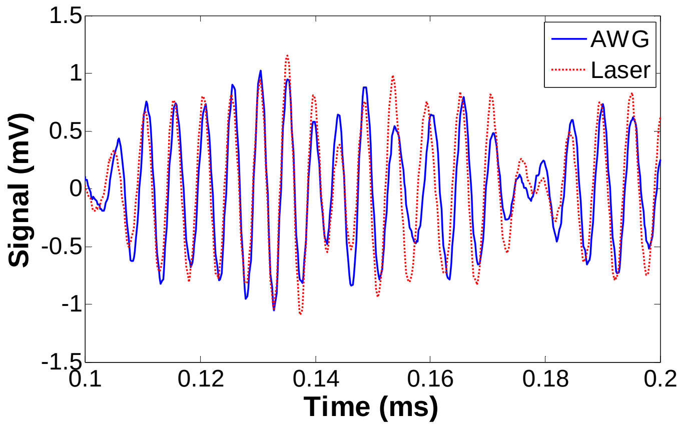

Figure 7.4 Comparison between AWG and laser excitation. The signal is measured using laser vibrometer.

The uniqueness of the laser based excitation used in this study is that, unlike conventional pulse laser sources, the proposed technique can excite arbitrary user defined waveforms at selective frequency ranges and can be used to remotely excite locations. Moreover, there is no risk of damaging the target structure if the power of the laser source goes into the ablative zone.

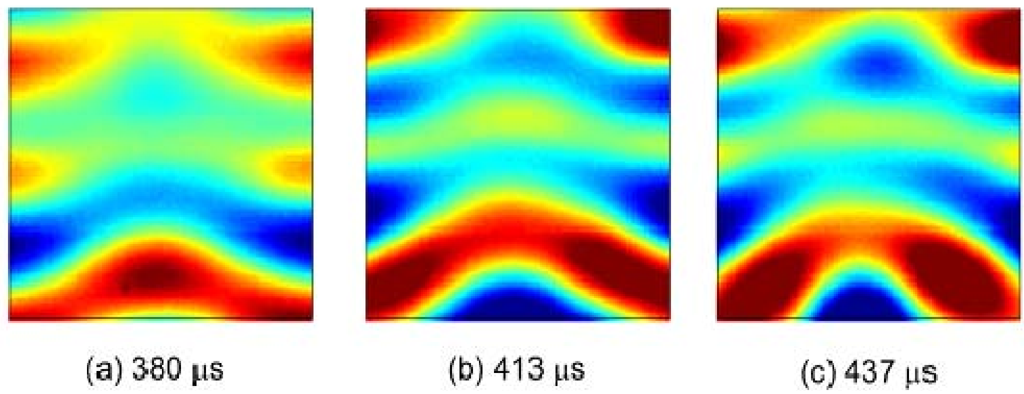

Figure 7.5 Snapshots of Lamb wave propagation with laser source excitation

Once the laser excitation setup is validated through point measurements (**Figure 7.4**), the ultrasonic velocity field images are obtained using the laser vibrometer. A tone-burst signal at 30 kHz was used for excitation. A sampling frequency of 1.28 MHz and a band pass filer with lower and higher cutoff frequencies of 15 kHz and 65 kHz were used for data acquisition using laser vibrometer. The other vibrometer settings remained identical to what is mentioned in the preceding sections. The scanned area is a square with 5 cm long sides containing 9000 scan points. **Figure 7.5** shows the wavefield images obtained using the wireless data interrogation system. Because of the multiple reflections from the junction between the base and the walls, the wave fronts in **Figure 7.5** are not as distinct as in the previous experiments.

In conclusion, a fully non-contact interrogation system consisting of a laser source and a laser vibrometer was used to construct ultrasonic field images in a composite specimen. The laser source used in this study can generate arbitrary user defined waveforms at selective frequencies without having to use a complicated and expensive array of optical lenses. However, the amplitude of the ultrasonic waves produced was low and reflective tapes had to be used to obtain any meaningful result from the laser vibrometer. The experimental results still count as a successful demonstration of a fully non-contact interrogation system, but a better optimized non-contact system is warranted for practical applications.

References

[1] ASCE, “Report Card for America's Infrastructure,” *http://www.infrastructurereportcard.org/*, 2009.

[2] V. Giurgiutiu, *Structural Health Monitoring: with Piezoelectric Wafer Active Sensors*, Academic Press, 2007.

[3] C. Boller, F. Chang, and Y. Fujino, *Encyclopedia of Structural Health Monitoring*, Wiley, 2009.

[4] J.A. Rice and B.F. Spencer Jr, “Structural health monitoring sensor development for the Imote2 platform,” *Proceedings of Sensors and Smart Structures Technologies for Civil, Mechanical, and Aerospace Systems (SPIE 6932),* vol. 693234, 2008.

[5] H. Sohn, C.R. Farrar, F.M. Hemez, D.D. Shunk, D.W. Stinemates, B.R. Nadler, and others, “A review of structural health monitoring literature: 1996-2001,” *Los Alamos National Laboratory, Technical Report LA-13976-MS, USA*, 2003.

[6] P.C. Chang, A. Flatau, and S.C. Liu, “Review paper: health monitoring of civil infrastructure,” *Structural Health Monitoring,* vol. 2, 2003, p. 257.

[7] A. Raghavan and C.E. Cesnik, “Review of guided-wave structural health monitoring,” *The Shock and vibration digest,* vol. 39, 2007, pp. 91–114.

[8] W. Staszewski, C. Boller, and G.R. Tomlinson, *Health Monitoring of Aerospace Structures: Smart Sensor Technologies and Signal Processing*, Wiley, 2004.

[9] V. Giurgiutiu and C.A. Rogers, “Electro-mechanical (E/M) impedance method for structural health monitoring and non-destructive evaluation,” *Structural Health Monitoring: Current Status and Perspectives*, 1997, p. 433.

[10] G. Park, H. Sohn, C.R. Farrar, and D.J. Inman, “Overview of piezoelectric impedance-based health monitoring and path forward,” *Shock and Vibration Digest*, vol. 35, 2003, pp. 451–464.

[11] A.J. Hillis, S.A. Neild, B.W. Drinkwater, and P.D. Wilcox, “Global crack detection using bispectral analysis,” *Proceedings of the Royal Society A: Mathematical, Physical and Engineering Science,* vol. 462, 2006, p. 1515.

[12] J.Y. Kim, L.J. Jacobs, J. Qu, and J.W. Littles, “Experimental characterization of fatigue damage in a nickel-base superalloy using nonlinear ultrasonic waves,” *The Journal of the Acoustical Society of America,* vol. 120, 2006, p. 1266.

[13] D.M. Donskoy and A.M. Sutin, “Vibro-acoustic modulation nondestructive evaluation technique,” *Journal of Intelligent Material Systems and Structures,* vol. 9, 1998, p. 765.

[14] H. Lamb, “On waves in an elastic plate,” *Proceedings of the Royal Society of London. Series A, Containing papers of a mathematical and physical character,* vol. 93, 1917, pp. 114–128.

[15] B.A. Auld, *Acoustic Fields and Waves in Solids, 2 Vol. Set*, Krieger Publishing Company, 1990.

[16] I. Viktorov, *Rayleigh and Lamb Waves: Physical Theory and Applications*, Plenum Press, 1967.

[17] W.J. Staszewski, B.C. Lee, L. Mallet, and F. Scarpa, “Structural health monitoring using scanning laser vibrometry: I,” *Smart Materials and Structures,* vol. 13, 2004, pp. 251–260.

[18] M. Ruzzene, “Frequency–wavenumber domain filtering for improved damage

visualization," *Smart Materials and Structures*, vol. 16, 2007, pp. 2116-2129.
[19] P.J. Shull, *Nondestructive Evaluation: Theory, Techniques, and Applications*, CRC Press, 2002.
[20] K. Worden, C.R. Farrar, G. Manson, and G. Park, "The fundamental axioms of structural health monitoring," *Proceedings of the Royal Society A: Mathematical, Physical and Engineering Science*, vol. 463, 2007, p. 1639.
[21] S.B. Kim and H. Sohn, "Instantaneous reference-free crack detection based on polarization characteristics of piezoelectric materials," *Smart Materials and Structures*, vol. 16, 2007, pp. 2375–2387.
[22] Younho Cho, "Estimation of ultrasonic guided wave mode conversion in a plate with thickness variation," *Ultrasonics, Ferroelectrics and Frequency Control, IEEE Transactions on*, vol. 47, 2000, pp. 591-603.
[23] S.B. Kim and H. Sohn, "Instantaneous crack detection using dual PZT transducers," *Proceedings of SPIE*, 2008, p. 693509.
[24] F.B. Cegla, A. Rohde, and M. Veidt, "Analytical prediction and experimental measurement for mode conversion and scattering of plate waves at non-symmetric circular blind holes in isotropic plates," *Wave Motion*, vol. 45, 2008, pp. 162–177.
[25] D.N. Alleyne and P. Cawley, "The interaction of Lamb waves with defects," *IEEE Transactions on Ultrasonics, Ferroelectrics and frequency control*, vol. 39, 1992, pp. 381–397.
[26] A. Demma, P. Cawley, M. Lowe, A.G. Roosenbrand, and B. Pavlakovic, "The reflection of guided waves from notches in pipes: a guide for interpreting corrosion measurements," *NDT and E International*, vol. 37, 2004, pp. 167–180.
[27] M.J.S. Lowe, D.N. Alleyne, and P. Cawley, "The mode conversion of a guided wave by a part-circumferential notch in a pipe," *Journal of Applied mechanics*, vol. 65, 1998, p. 649.
[28] Z. Su and L. Ye, "Selective generation of Lamb wave modes and their propagation characteristics in defective composite laminates," *Proceedings of the Institution of Mechanical Engineers, Part L: Journal of Materials: Design and Applications*, vol. 218, 2004, pp. 95–110.
[29] S. Park, C. Lee, and H. Sohn, "Reference-free crack detection using transfer impedances," *Journal of Sound and Vibration*, 2009.
[30] E.S. Sazonov, P. Klinkhachorn, U.B. Halabe, and H.V. GangaRao, "Non-baseline detection of small damages from changes in strain energy mode shapes," *Nondestructive Testing and Evaluation*, vol. 18, 2002, pp. 91–107.
[31] S.R. Anton, D.J. Inman, and G. Park, "Reference-Free Damage Detection Using Instantaneous Baseline Measurements," *AIAA JOURNAL*, vol. 47, 2009.
[32] J.L. Rose, *Ultrasonic Waves in Solid Media*, Cambridge University Press, 2004.
[33] K.F. Graff, *Wave Motion in Elastic Solids*, Dover Publications, 1991.
[34] Y. Cho and J.L. Rose, "A boundary element solution for a mode conversion study on the edge reflection of Lamb waves," *The Journal of the Acoustical Society of America*, vol. 99, 1996, p. 2097.
[35] J.D. Achenbach, *Reciprocity in Elastodynamics*, Cambridge University Press, 2004.
[36] R. Penrose, "A generalized inverse for matrices," *Proc. Cambridge Philos. Soc*, 1955, pp. 406–413.
[37] J.J. Dosch, D.J. Inman, and E. Garcia, "A self-sensing piezoelectric actuator for

collocated control," *Journal of Intelligent Material Systems and Structures*, vol. 3, 1992, p. 166.

[38] N.W. Hagood, W.H. Chung, and A. Von Flotow, "Modelling of piezoelectric actuator dynamics for active structural control," *Journal of Intelligent Material Systems and Structures*, vol. 1, 1990, p. 327.

[39] S.J. Lee and H. Sohn, "Active self-sensing scheme development for structural health monitoring," *Smart Materials and Structures*, vol. 15, 2006, pp. 1734-1746.

[40] H. Sohn, "Effects of environmental and operational variability on structural health monitoring," *Philosophical Transactions of the Royal Society A: Mathematical, Physical and Engineering Sciences*, vol. 365, 2007, p. 539.

[41] G. Park, K. Kabeya, H.H. Cudney, and D.J. Inman, "Impedance-based structural health monitoring for temperature varying applications," *JSME International Journal Series A*, vol. 42, 1999, pp. 249–258.

[42] C.P. Fritzen, G. Mengelkamp, and A. Guemes, "Elimination of temperature effects on damage detection within a smart structure concept," *Structural Health Monitoring 2003: From Diagnostics & Prognostics to Structural Health Management: Proceedings of the 4 th International Workshop on Structural Health Monitoring, Stanford University, Stanford, CA, September 15-17, 2003*, 2003, pp. 1530–1538.

[43] Y. Lu and J.E. Michaels, "A methodology for structural health monitoring with diffuse ultrasonic waves in the presence of temperature variations," *Ultrasonics*, vol. 43, 2005, pp. 717–731.

[44] A.J. Croxford, P.D. Wilcox, B.W. Drinkwater, and G. Konstantinidis, "Strategies for guided-wave structural health monitoring," *Proceedings of the Royal Society A: Mathematical, Physical and Engineering Science*, vol. 463, 2007, p. 2961.

[45] Z. Parsons and W.J. Staszewski, "Nonlinear acoustics with low-profile piezoceramic excitation for crack detection in metallic structures," *Smart Materials and Structures*, vol. 15, 2006, pp. 1110–1118.

[46] M. Huang, L. Jiang, P.K. Liaw, C.R. Brooks, R. Seeley, and D.L. Klarstrom, "Using acoustic emission in fatigue and fracture materials research," *JOM*, vol. 50, 1998, pp. 1–14.

[47] A. Sophian, G.Y. Tian, D. Taylor, and J. Rudlin, "Electromagnetic and eddy current NDT: a review," *Insight*, vol. 43, 2001, pp. 302–306.

[48] T.G. Chondros, A.D. Dimarogonas, and J. Yao, "A continuous cracked beam vibration theory," *Journal of Sound and Vibration*, vol. 215, 1998, pp. 17–34.

[49] S.S. Kessler, S.M. Spearing, and C. Soutis, "Damage detection in composite materials using Lamb wave methods," *Smart Materials and Structures*, vol. 11, 2002, pp. 269–278.

[50] P. Rizzo, M. Cammarata, D. Dutta, and H. Sohn, "An unsupervised learning algorithm for fatigue crack detection in waveguides," *Smart Materials and Structures*, vol. 18, 2009, p. 025016.

[51] T. Kundu, *Ultrasonic Nondestructive Evaluation: Engineering and Biological Material Characterization*, CRC Press, 2003.

[52] O. Buck and W.L. Morris, "Acoustic harmonic generation at unbonded interfaces and fatigue cracks," *The Journal of the Acoustical Society of America*, vol. 64, 1978, p. S33.

[53] W.L. Morris, O. Buck, and R.V. Inman, "Acoustic harmonic generation due to fatigue damage in high-strength aluminum," *Journal of Applied Physics*, vol. 50, 1979, p. 6737.

[54] J.M. Richardson, "Harmonic generation at an unbonded interface--I. Planar interface between semi-infinite elastic media," *International Journal of Engineering Science*, vol. 17, 1979, pp. 73-85.

[55] I. Bartoli, C. Nucera, A. Srivastava, S. Salamone, R. Phillips, F. Lanza di Scalea, S. Coccia, and C.S. Sikorsky, "Nonlinear ultrasonic guided waves for stress monitoring in prestressing tendons for post-tensioned concrete structures," *Proceedings of SPIE*, San Diego, CA, USA: 2009, pp. 729220-729220-11.

[56] A. Rivola, "Comparison between second and higher order spectral analysis in detecting structural damages," *Proceedings of Seventh International Conference on Recent Advances in Structural Dynamics*, 2000, pp. 937–950.

[57] M. K\ögl, S. Hurlebaus, and L. Gaul, "Finite element simulation of non-destructive damage detection with higher harmonics," *NDT and E International*, vol. 37, 2004, pp. 195–205.

[58] K. Kawashima, R. Omote, T. Ito, H. Fujita, and T. Shima, "Nonlinear acoustic response through minute surface cracks: FEM simulation and experimentation," *Ultrasonics*, vol. 40, 2002, pp. 611–615.

[59] C. Pecorari, "Nonlinear interaction of plane ultrasonic waves with an interface between rough surfaces in contact," *The Journal of the Acoustical Society of America*, vol. 113, 2003, p. 3065.

[60] M.I. Friswell and J.E.T. Penny, "Crack modeling for structural health monitoring," *Structural Health Monitoring*, vol. 1, 2002, p. 139.

[61] K. Worden and G. Tomlinson, *Nonlinearity in Structural Dynamics: Detection, Identification and Modelling*, Taylor & Francis, 2001.

[62] J.A. Greenwood and J.B.P. Williamson, "Contact of Nominally Flat Surfaces," *Proceedings of the Royal Society of London. Series A. Mathematical and Physical Sciences*, vol. 295, Dec. 1966, pp. 300-319.

[63] D.J. Ewins, *Modal Testing: Theory, Practice and Application*, Wiley, 2001.

[64] W. Zhu, J.L. Rose, J.N. Barshinger, and V.S. Agarwala, "Ultrasonic guided wave NDT for hidden corrosion detection," *Research in Nondestructive Evaluation*, vol. 10, 1998, pp. 205–225.

[65] P.D. Wilcox, M.J.S. Lowe, and P. Cawley, "Mode and Transducer Selection for Long Range Lamb Wave Inspection," *Journal of Intelligent Material Systems and Structures*,, 2001, pp. 553 -565 vol. 12:

[66] S.P. Pelts, D. Jiao, and J.L. Rose, "A comb transducer for guided wave generation and mode selection," *1996 IEEE Ultrasonics Symposium, 1996. Proceedings.*, 1996, pp. 857–860.

[67] G.A. Alers and L.R. Burns, "EMAT designs for special applications," 1987.

[68] M. Platte, "PVDF - ultrasonic transducers," *Ferroelectrics*, vol. 75, 1987, p. 327.

[69] D.C. Betz, G. Thursby, B. Culshaw, and W.J. Staszewski, "Acousto-ultrasonic sensing using fiber Bragg gratings," *Smart Materials and Structures*, vol. 12, 2003, pp. 122-128.

[70] B. Culshaw, G. Pierce, and P. Jun, "Non-contact measurement of the mechanical properties of materials using an all-optical technique," *IEEE Sensors Journal*, vol.

3, 2003, pp. 62–70.
[71] W.H. Leong, W.J. Staszewski, B.C. Lee, and F. Scarpa, “Structural health monitoring using scanning laser vibrometry: III. Lamb waves for fatigue crack detection,” *Smart Materials and Structures*, vol. 14, 2005, pp. 1387–1395.
[72] Fei Yan, R.L. Royer, and J.L. Rose, “Ultrasonic Guided Wave Imaging Techniques in Structural Health Monitoring,” *Journal of Intelligent Material Systems and Structures*, vol. 21, Feb. 2010, pp. 377 -384.
[73] V. Giurgiutiu and J. Bao, “Embedded-ultrasonics Structural Radar for In Situ Structural Health Monitoring of Thin-wall Structures,” *Structural Health Monitoring*, vol. 3, Jun. 2004, pp. 121-140.
[74] D.W. Greve, I.J. Oppenheim, and N.L. Tyson, “Interaction of defects with Lamb waves in complex geometries,” *IEEE Ultrasonics Conference Proceedings*, 2005, pp. 297–300.
[75] W.J. Staszewski, B.C. Lee, and R. Traynor, “Fatigue crack detection in metallic structures with Lamb waves and 3D laser vibrometry,” *Measurement Science and Technology*, vol. 18, 2007, pp. 727–739.
[76] S. Yashiro, J. Takatsubo, and N. Toyama, “An NDT technique for composite structures using visualized Lamb-wave propagation,” *Composites Science and Technology*, vol. 67, Dec. 2007, pp. 3202-3208.
[77] S. Yashiro, J. Takatsubo, H. Miyauchi, and N. Toyama, “A novel technique for visualizing ultrasonic waves in general solid media by pulsed laser scan,” *NDT & E International*, vol. 41, 2008, pp. 137–144.
[78] J.R. Lee, J. Takatsubo, and N. Toyama, “Disbond monitoring at wing stringer tip based on built-in ultrasonic transducers and a pulsed laser,” *Smart Materials and Structures*, vol. 16, 2007, pp. 1025–1035.
[79] Polytec GmbH, “Non-contact vibration measurement,” Feb. 2010.
[80] T. Hayashi and K. Kawashima, “Multiple reflections of Lamb waves at a delamination,” *Ultrasonics*, vol. 40, 2002, pp. 193–197.
[81] G.R. Liu and J.D. Achenbach, “Strip element method to analyze wave scattering by cracks in anisotropic laminated plates,” *Journal of Applied Mechanics*, vol. 62, 1995, p. 607.
[82] R.C. Gonzalez, R.E. Woods, and S.L. Eddins, *Digital Image Processing Using MATLA*, Prentice Hall, 2003.
[83] Weidlinger Assoc., “PZFlex, http://www.pzflex.com/,” *PZFlex, http://www.pzflex.com/*.
[84] A. Nag, D. Roy Mahapatra, S. Gopalakrishnan, and T.S. Sankar, “A spectral finite element with embedded delamination for modeling of wave scattering in composite beams,” *Composites Science and Technology*, vol. 63, Nov. 2003, pp. 2187-2200.
[85] F. Pukelsheim, “The Three Sigma Rule,” *The American Statistician*, vol. 48, May. 1994, pp. 88-91.
[86] T. Bailey and T. Gatrell, *Interactive Spatial Data Analysis*, Prentice Hall, 1996.
[87] K.B. Olsen, S.M. Day, J.B. Minster, Y. Cui, A. Chourasia, M. Faerman, R. Moore, P. Maechling, and T. Jordan, “Strong shaking in Los Angeles expected from southern San Andreas earthquake,” *Geophys. Res. Lett*, vol. 33, 2006, pp. 575–596.
[88] J.L. Rose, “Guided waves: Successes and challenges for ultrasonic testing in NDT and SHM,” *Materials Evaluation*, vol. 68, 2010, pp. 494-500.